

SEA SURFACE MOTION INDUCED EFFECTS ON HIGH FREQUENCY
UNDERWATER ACOUSTIC SIGNALS

A THESIS SUBMITTED TO
THE GRADUATE SCHOOL OF NATURAL AND APPLIED SCIENCES
OF
MIDDLE EAST TECHNICAL UNIVERSITY

BY
HASAN GÜNEŞ

IN PARTIAL FULFILLMENT OF THE REQUIREMENTS
FOR
THE DEGREE OF MASTER OF SCIENCE
IN
ELECTRICAL AND ELECTRONICS ENGINEERING

SEPTEMBER 2014

Approval of the thesis:

**SEA SURFACE MOTION INDUCED EFFECTS ON HIGH FREQUENCY
UNDERWATER ACOUSTIC SIGNALS**

submitted by **HASAN GÜNEŞ** in partial fulfillment of the requirements for the degree of **Master of Science in Electrical and Electronics Engineering Department, Middle East Technical University** by,

Prof. Dr. Canan Özgen
Dean, Graduate School of **Natural and Applied Science**

Prof. Dr. Gönül Turhan Sayan
Head of Department, **Electrical and Electronics Engineering**

Prof. Dr. Tolga Çiloğlu
Supervisor, **Electrical and Electronics Eng. Dept., METU**

Examining Committee Members:

Prof. Dr. Mustafa Kuzuoğlu
Electrical and Electronics Engineering Dept., METU

Prof. Dr. Tolga Çiloğlu
Electrical and Electronics Engineering Dept., METU

Prof. Dr. Sencer Koç
Electrical and Electronics Engineering Dept., METU

Assoc. Prof. Dr. Ali Özgür Yılmaz
Electrical and Electronics Engineering Dept., METU

M.S. Zekeriyya Şahin
ASELSAN

Date:

I hereby declare that all information in this document has been obtained and presented in accordance with academic rules and ethical conduct. I also declare that, as required by these rules and conduct, I have fully cited and referenced all material and results that are not original to this work.

Name, Last Name: HASAN GÜNEŞ

Signature :

ABSTRACT

SEA SURFACE MOTION INDUCED EFFECTS ON HIGH FREQUENCY UNDERWATER ACOUSTIC SIGNALS

Güneş, Hasan

M.S., Department of Electrical and Electronics Engineering

Supervisor: Prof. Dr. Tolga Çiloğlu

September 2014, 108 pages

Acoustic signal scattering from the moving sea surface constitutes one of the most significant problems in underwater communication and sonar applications when dealing with signal processing especially at high frequencies. In this thesis, a realistic 3D linear sea surface wave model which solves governing equations is combined with a ray based computationally efficient acoustic model, BELLHOP, in order to simulate the effects of the time-evolving sea surface on acoustic waves. Rough sea surface realizations according to main environmental parameters (wind speed and fetch) are generated and imported into acoustic model to simulate temporal fluctuations in the acoustic signals. Doppler shifts in frequency of source signal are calculated by using the surface-normal velocities provided by sea surface wave model and acoustic rays provided by BELLHOP tool. Received timeseries are generated by convolution of source timeseries and time-varying impulse response of the underwater channel which is obtained from application of an existing interpolation scheme to arrival amplitude-delay pairs in order to simulate amplitude fluctuations as well. In addition, Monte Carlo based simulations are made to relate wind speed and acoustic signal fluctuations statistically.

Keywords: Time-Evolving Sea Surface Waves, Underwater Acoustic Signal Scattering, Ray Tracing

ÖZ

YÜKSEK FREKANSLI SUALTI AKUSTİK SİNYALLERİ ÜZERİNDE DENİZ YÜZEYİ HAREKETİ KAYNAKLI ETKİLER

Güneş, Hasan

Yüksek Lisans Elektrik Elektronik Mühendisliği Bölümü

Tez Yöneticisi: Prof. Dr. Tolga Çiloğlu

Eylül 2014, 108 sayfa

Akustik sinyallerin hareket eden deniz yüzeyinden yansması özellikle yüksek frekansta sinyal işleme yapılan sualtı iletişimi ve sonar uygulamalarındaki en önemli problemlerden birini oluşturmaktadır. Bu tezde, hükmeden denklemleri çözen gerçekçi bir üç boyutlu doğrusal deniz yüzeyi dalga modeli ile hesaplama verimli ışın temelli bir akustik dalga modeli, BELLHOP, zamanda ilerleyen deniz yüzeyi dalgalarının akustik sinyaller üzerinde etkisini benzetmek için birleştirilmiştir. Temel çevresel parametrelere (rüzgâr hızı ve rüzgâr mesafesi) göre üretilen pürüzlü deniz yüzeyleri gerçeklemeleri akustik sinyallerdeki zamansal dalgalanmaları benzetmek için akustik modele dâhil edilmiştir. Kaynak sinyalinin frekansındaki Doppler kaymaları deniz yüzeyi dalga modeli tarafından sağlanan yüzey normali hızları ve BELLHOP aracı tarafından sağlanan akustik ışınlar kullanılarak hesaplanmıştır. Alınan zaman dizisi de kaynak zaman serisi ile sualtı kanalının var olan bir aradeğerleme şemasının varış genliği-gecikmesi çiftlerine uygulanması ile elde edilen zamanla değişen dürtü tepkisinin evrimi ile üretilebilir. Ek olarak, rüzgâr hızı ile akustik sinyal dalgalanmalarını istatistiksel olarak ilişkilendirmek için Monte Carlo temelli benzetimler yapılmıştır.

Anahtar Kelimeler: Zamanla İlerleyen Deniz Yüzeyi Dalgaları, Sualtı Akustik Sinyal Saçılması, Işın İzleme

To my Wife and my Family

ACKNOWLEDGMENTS

I would like to express my deepest gratitude to my supervisor Prof. Dr. Tolga ÇİLOĞLU for his guidance, advice, criticism, encouragements and insight throughout the research.

Thanks to the examining committee members Prof. Dr. Mustafa KUZUOĞLU, Prof. Dr. Sencer KOÇ, Assoc. Prof. Dr. Ali Özgür YILMAZ, and M.Sc. Zekeriyya ŞAHİN for evaluating my work and for their valuable comments.

Deepest thanks to my wife and my family for their love, trust, understanding, and every kind of support not only throughout my thesis but also throughout my life.

TABLE OF CONTENTS

ABSTRACT.....	v
ÖZ.....	vi
ACKNOWLEDGEMENTS.....	viii
TABLE OF CONTENTS.....	ix
LIST OF TABLES.....	xi
LIST OF FIGURES.....	xii
CHAPTERS	
1 INTRODUCTION	1
1.1 Introduction.....	1
1.2 Outline.....	4
2 LINEAR SEA SURFACE WAVE FIELD MODEL.....	7
2.1 Introduction.....	7
2.2 Sea Surface Waves.....	7
2.3 Concept of Sea Surface Wave Spectrum	11
2.3.1 Pierson-Moskowitz Sea Surface Spectrum	12
2.3.2 JONSWAP Sea Surface Spectrum.....	14
2.3.3 Angular/Directional Spreading	16
2.4 Construction Steps for 2D and 3D Sea Surface Wave Fields.....	19
2.4.1 Frequency to Wavenumber Conversion in 2D.....	19
2.4.2 Directional Wave Spectra	19
2.4.3 Construction of Initial Surface Wave Field in 2D	20
2.4.4 Construction of Initial Surface Wave Field in 3D	22
2.5 Governing Equations for the Surface Wave Model.....	25
2.5.1 Fourth Order Runge-Kutta Method.....	26

2.6	Calculation of Surface-Normal Velocity	27
2.7	Swell.....	28
2.8	2D Linear Sea Surface Wave Model.....	29
2.9	3D Linear Sea Surface Wave Model.....	32
3	ACOUSTIC SCATTERING FROM THE SEA SURFACE	39
3.1	Introduction.....	39
3.2	Physical Basis for the Numerical Model.....	39
3.2.1	Theoretical Background	39
3.2.2	Gaussian Beam Tracing and BELLHOP Model	44
3.3	BELLHOP Ray Tracing Model	54
3.3.1	BELLHOP Input Files.....	55
3.3.2	BELLHOP Output Files	57
3.4	Doppler Shift Calculations.....	62
4	VirTEX ALGORITHM.....	65
4.1	Introduction.....	65
4.2	Modeling Source and Receiver Motion with Rays	67
4.3	Modeling Time Varying Sea Surfaces	72
5	COUPLED MODEL & DISCUSSION OF SIMULATIONS	77
5.1	BELLHOP and Time-evolving Sea Surface Wave Model Integration	77
5.2	Simulations and Discussions.....	84
6	CONCLUSION	103
6.1	Concluding Remarks.....	103
6.2	Future Work	103
	REFERENCES.....	105

LIST OF TABLES

TABLES

Table 2.1: Beaufort Wind Force Scale [38]	8
Table 5.1: Table of constant simulation parameters	84

LIST OF FIGURES

FIGURES

Figure 2.1: Evolution of Wind Waves Growth [25].....	10
Figure 2.2: Wave Spectra of a Fully Developed Sea for Different Wind Speeds According to Moskowitz (1964) [26].....	13
Figure 2.3: Wave Spectra of Developing Sea for Different Fetches According to Hasselmann et al. (1973) [26]	14
Figure 2.4: 2D Linear Sea Surface Wave Snapshot (N=1024)	30
Figure 2.5: Input and Output Wavenumber Spectra Comparison	31
Figure 2.6: 3D Linear Sea Surface Waves Snapshot (Main Wind Direction: 0°).....	33
Figure 2.7: 3D Linear Sea Surface Waves Snapshot (Main Wind Direction: 0°).....	34
Figure 2.8: 3D Linear Sea Surface Waves Snapshot (Main Wind Direction: 45°)....	34
Figure 2.9: 3D Linear Sea Surface Waves Snapshot (Main Wind Direction: 45°)....	35
Figure 2.10: 3D Linear Sea Surface Waves Snapshot (Main Wind Direction: 45°)..	35
Figure 2.11: 3D Linear Sea Surface Waves Snapshot (Main Wind Direction: 90°)..	36
Figure 2.12: A Comparison of Input and Output Wavenumber Spectra (Main Wind Direction: 45°).....	37
Figure 3.1: Rays and Wavefronts [29]	41
Figure 3.2: Snell's Law and Calculation of the Grazing Ray [29].....	42
Figure 3.3: A Ray Refracting through a Stack of Layers [29]	43
Figure 3.4: Schematic of the 2D Ray Geometry [29]	48
Figure 3.5: The Ray-Tube Cross Section [29]	52
Figure 3.6: Transmission Loss (a) Standard Ray Tracing versus Exact Solution, (b) Gaussian Beam Tracing Solution vs. Exact Solution, Solid Curve: Exact Solution [29]	55
Figure 3.7: Ray Reflected from a Piecewise Linear Boundary [29]	56
Figure 3.8: Eigenrays for the Munk Sound Speed Profile with the Source at 1000 m and the Receiver at 800 m [40]	58
Figure 3.9: Coherent Transmission Loss Calculated by BELLHOP [44]	60

Figure 3.10: An Example Channel Impulse Response, reproduced from [40]	61
Figure 3.11: Doppler Effect of Moving Object. Source and Receiver in x-z Plane [8]	62
Figure 3.12: Multiple Interactions of Acoustic Eigenrays from the Sea Surface [1].	64
Figure 4.1: A Notional Example of Piecewise Continuous Approximation to the Arrival Function for a Single Eigenray Computed by the VirTEX Algorithm [14]..	66
Figure 4.2: A Notional Example of the Wall Clock Time Arrival Function $w(t)$ (a) Steady Motion Case (b) Unsteady Motion Case [14]	69
Figure 4.3: Four Points of the Computational Grid for a Ray Trace. The Actual Arrivals are Computed at the Four Corners and any Point in the Interior Computed through Interpolation of the Amplitudes and Extrapolation of the Delays. A Sample Arrival is Shown Travel [4]	71
Figure 4.4: Same as Figure 4.3 Except with the Added Dimension to Allow for Time Changing Surface [4]	73
Figure 5.1: Time-varying Sea Surface Model. (top) Snapshot of 3D Time-varying Sea Surface Wave Field with Wind Speed 10m/s and at Wind Direction 45° . (bottom) Corresponding 2D Cross-section of 3D Sea Surface Snapshot	79
Figure 5.2: Plot of Eigenrays. Eliminated eigenrays are also showed. Red Lines are far from the Receiver and Dashed Line has a Low Amplitude.....	80
Figure 5.3: Geometry of Small Beam Fan to Increase Resolution with the Same Computational Speed, redesigned by [13]	81
Figure 5.4: Block Diagram of the Coupled Model	84
Figure 5.5: Arrival Time Fluctuation of the Strongest Eigenray: $U=1\text{m/s}$, $X=25\text{km}$	85
Figure 5.6: Arrival Time Fluctuation of the Strongest Eigenray: $U=5\text{m/s}$, $X=25\text{km}$	86
Figure 5.7: Arrival Time Fluctuation of the Strongest Eigenray: $U=14\text{m/s}$, $X=25\text{km}$	86
Figure 5.8: A Comparison of Arrival Time Fluctuations. Blue Line: $U=1\text{m/s}$, Green Line: $U=5\text{m/s}$, and Red Line: $U=14\text{m/s}$	87
Figure 5.9: Arrival Angle Fluctuation of the Strongest Eigenray: $U=1\text{m/s}$, $X=25\text{km}$	88
Figure 5.10: Arrival Angle Fluctuation of the Strongest Eigenray: $U=1\text{m/s}$, $X=25\text{km}$	88

Figure 5.11: Arrival Angle Fluctuation of the Strongest Eigenray: $U=14\text{m/s}$, $X=25\text{km}$	89
Figure 5.12: A Comparison of Arrival Angle Fluctuations. Blue Line: $U=1\text{m/s}$, Green Line: $U=5\text{m/s}$, and Red Line: $U=14\text{m/s}$	90
Figure 5.13: Doppler Shift Fluctuation of the Strongest Eigenray: $U=1\text{m/s}$, $X=25\text{km}$	90
Figure 5.14: Doppler Shift Fluctuation of the Strongest Eigenray: $U=5\text{m/s}$, $X=25\text{km}$	91
Figure 5.15: Doppler Shift Fluctuation of the Strongest Eigenray: $U=14\text{m/s}$, $X=25\text{km}$	91
Figure 5.16: A Comparison of Absolute Doppler Shift Fluctuations. Blue Line: $U=1\text{m/s}$, Green Line: $U=5\text{m/s}$, and Red Line: $U=14\text{m/s}$	92
Figure 5.17: Time Series of Acoustic Signal. (a) Source Time Series (b), (c), and (d) Received Time Series for $U=1\text{m/s}$, $U=5\text{m/s}$, and $U=14\text{m/s}$ respectively.	93
Figure 5.18: Spectrogram for Received Time Series for $U = 14\text{m/s}$, $X = 25\text{km}$	94
Figure 5.19: Arrival Time Fluctuation of the Strongest Eigenray: $U=5\text{m/s}$, $X=100\text{km}$	95
Figure 5.20: Arrival Angle Fluctuation of the Strongest Eigenray: $U=5\text{m/s}$, $X=100\text{km}$	95
Figure 5.21: Doppler Shift Fluctuation of the Strongest Eigenray: $U=5\text{m/s}$, $X=100\text{km}$	96
Figure 5.22: Received Signal for, $U=5\text{m/s}$, $X=100\text{km}$. (top) Received Time Series (bottom) Spectrogram of Received Time Series	97
Figure 5.23: Standard Deviation of Arrival Time wrt. Wind Speed (U)	98
Figure 5.24: Standard Deviation of Arrival Angle wrt. Wind Speed (U)	99
Figure 5.25: Standard Deviation of Doppler Shift wrt. Wind Speed (U).....	100
Figure 5.26: Standard Deviation of Arrival Time wrt. Wind Speed (U)	100
Figure 5.27: Standard Deviation of Arrival Angle wrt. Wind Speed (U)	101
Figure 5.28: Standard Deviation of Doppler Shift wrt. Wind Speed (U).....	101

CHAPTER 1

INTRODUCTION

1.1 Introduction

Propagation of sound in underwater acoustic channel can be affected from several environmental parameters. Due to sea water depth, temperature, and salinity sound speed profile changes, transmission paths bend or refract to region sound speed is low [29]. Conditions of sea bottom and sea surface are other crucial parameters which influence acoustic propagation. All environmental parameters have different effects on underwater acoustic systems. These effects are crucial for transmission of information and determining performance of communication system in underwater.

Sea surface waves are one of the most essential environmental parameters. The effects of surface waves on propagation acoustic signal at high frequency are important especially in shallow water. Acoustic scattering from the rough sea surface can be a significant source of reverberation in coastal areas. Since air-sea interface is in motion, sea surface interacted acoustic waves are subjected to Doppler Effect. Interaction of acoustic sound waves with time-varying sea surface causes scattering of energy of acoustic signal into coherent and incoherent components. Rayleigh roughness parameter (R) is utilized in order to characterize sea surface roughness from acoustic point of view. R is defined as $2kh_{rms} \sin \theta_g$ where k , h_{rms} , and θ_g represents acoustic wavenumber, root-mean-square (rms) surface waveheight (crest to trough), and acoustic grazing angle respectively. Sea surface is primarily a reflector when $R \ll 1$. Since roughness is small, energy of acoustic wave reflected coherently at the specular angle. When $R \gg 1$ the sea surface roughness is high. Therefore, acoustic wave energy is scattered in all directions incoherently [16].

Since sea surface waves have significant impact on propagation of sound waves in a watercolumn, the problem of modeling acoustic energy reflected/scattered from sea

surface has been studied by many researchers in the literature. Theories for the prediction of acoustic intensity scattered from randomly rough surfaces developed mainly through two widely accepted methods. These methods are suitable for different scale of surface roughness. One of these methods is based on standard physical optics which is called as Kirchhoff approach [9]. Kirchhoff approach is applied when roughness is large but smooth. Other method is Rayleigh-Rice [10] approach which based on small perturbation of roughness. Combinations of these two methods also have been proposed because sea surface contains many spatial scales [34], [36]. In one of these combinations [34], rms sea surface height and slopes of the sea surface which is formed by empirical data are utilized. A comparison is made by Thorsos [5] between exact Helmholtz integration method and Kirchhoff and Rayleigh-Rice methods. Rough surface realizations according to Pierson-Moskowitz [27] sea surface wave spectrum have been used as inputs to check accuracy of Kirchhoff and Rayleigh-Rice methods in [5].

There are several stochastic studies in literature in order to relate spectral density of acoustic pressure which is reradiated from rough sea surface and statistical parameters of the rough surface. In Parkins [17] two extreme cases are discussed which are slightly rough and very rough sea surfaces namely. For slightly rough sea surfaces, spectrum of sea surface is mapped as lower and upper sidebands of the reradiated acoustic wave field. If sea surface is very rough, spectrum of reradiated energy broadens and becomes Gaussian-shaped regardless of sea surface wave spectrum. However there is no solution in [17] when sea surface roughness is moderate. In Scharf and Swarts [18] similar results are obtained again by using method of physical optics (Kirchhoff method) following the [17]. Roderick and Cron [19] and Roderick and Deavenport [31] have also studied theoretical analysis of frequency spectra of forward-scattered sound from the ocean surface. They do a model tank experiments and an ocean experiments to determine the frequency spread of sound reradiated form sea surface. Their studies present that acoustic waves reflected/scattered from the sea surface are modulated in amplitude and phase. Amount of frequency spreading is related to frequency of acoustic signal, sea surface wave spectrum, and geometry. The Doppler shift in the backscatter contains information on the direction of surface wave propagation as well according to [31].

Time-angle spreading characteristics of received acoustic signals are observed at experiments of Dahl [31]. In these experiments geometry of forward scattering from rough watercolumn boundary and environmental conditions related with ocean surface are taken into account to observe their relationships with the time-angle spreading of acoustic waves at the receiver for high-frequency transmission. Physical optics method based on assumption that incident wave is locally reflected is used to conclude about results of the experiments.

Acoustic field is modeled by aid of computers by using four types of numerical methods: 1) ray tracing, 2) normal modes [12], 3) fast-field program [11], and 4) the parabolic equation. Methods 2, 3, and 4 are in class of full wave models. However, class of ray-based models is computationally efficient and accurate especially in high frequency simulations [33]. A deterministic method with ray theory approximations (the wave front model) [37] is used to observe travel time and arrival amplitude fluctuations of acoustic signals due to curvature of ocean waves [34]. Ray-based tool, BELLHOP [3] which uses the Gaussian beam tracing model [2] gives impulse response of the underwater acoustic channel for a given geometry of source(s) and receiver(s) and frequency of source. However, BELLHOP runs for static environments and does not take in to account time-varying changes in the environment (air-sea interface). Environmental data obtained from an acoustic experiment is utilized to construct random time-evolving rough ocean surface realizations in Heitsenrether and Badiey [23]. Rough sea surface boundary is given as an input to be used by BELLHOP Gaussian beam tracer to compute corresponding acoustic field. Experiment results agree with simulation especially in case of sea surface roughness is small. BELLHOP model with a realistic, and time-evolving sea surface model are combined in [1], [13] to provide fluctuations of the time of arrival and angle of time along the transmission time of acoustic signal in the shallow water. Out-of-plane scattering of acoustic wave energy is ignored in those studies. VirTEX code [4] is also a tool to simulate a time-varying channel. VirTEX is based on repeated BELLHOP applications to show cumulative effect of environmental variation on the receiver side.

In this thesis, similar to [13] 2D realizations of the sea waves obtained from downwind direction cross-sections of 3D realizations of ocean [1] are combined with BELLHOP Gaussian beam tracing model. Doppler shifts on eigenrays of acoustic signals calculated according to [1] are utilized to show fluctuation of change of frequency of eigenrays across the transmission time. In order to simulate amplitude fluctuations of received signal at the hypothetical receiver location, VirTEX code is also used in this thesis with its interpolation scheme. The received timeseries are obtained from source timeseries with interpolated channel impulse responses by using VirTEX method.

Combination of time-evolving sea surface wave model with ray-based acoustic propagation model, BELLHOP, in order to obtain temporal fluctuations of acoustic wave energy due to sea surface motion correlated with environmental parameters such as wind speed and fetch is the main purpose of this thesis. Computing received timeseries from source time series by convolving is another focus of attention to observe amplitude fluctuations of received signals. Statistical relationship between environmental conditions and variations in acoustic signal by using Monte Carlo simulations to generate ensemble averages of random realizations. Wind speed is principal environmental parameter to take account in these simulations.

1.2 Outline

In Chapter 2 of this thesis construction of initial wave field by JONSWAP spectrum and Inverse Fourier Transform method, governing equations of the linear wave model and their numerical solution technique is explained. Sea surface wave field simulations are presented in both two and three dimensions.

In Chapter 3, acoustic scattering of sound waves from the ocean surface are discussed. The Gaussian beam approach, which is an extension to standard ray tracing theory, is explained. Also, the acoustic Gaussian beam tracing program BELLHOP which is used for modeling sound waves inside the watercolumn is described. Doppler shift calculations by using surface-normal velocities calculated by sea surface wave model are also mentioned in this chapter.

In Chapter 4, there is a brief explanation of VirTEX code which is used to interpolation of channel impulse responses in order to obtain received timeseries at a hypothetical receiver location in this thesis.

In Chapter 5, coupled/combined model scheme of linear sea surface wave model and BELLHOP Gaussian beam tracing method is introduced. Simulations through time-evolving sea surface for different environmental conditions are presented in this chapter as well. In addition, statistics for temporal fluctuations of the source signal are provided based on Monte Carlo technique. Discussions for both simulation types are made to comment the sea surface motion induced effects on the acoustic signals.

In Chapter 6, some brief concluding remarks are made with suggestions for future work.

CHAPTER 2

LINEAR SEA SURFACE WAVE FIELD MODEL

2.1 Introduction

This thesis followed an approach given by in [1] and [13] constructing linear sea surface wave field. Linear sea surface wave evolution equations are solved numerically starting with initial surface fluctuation and surface velocity potential. Initial wave field is constructed based on the given sea surface wave spectrum. JONSWAP sea surface wave spectrum is used with Hasselmann spreading function in order to obtain 3D linear waves. JONSWAP spectrum presents a relationship between environmental variables, such as wind speed, fetch length, and frequency distribution of sea surface waves. Wind speed has a specific significance for simulations which are mentioned in Section 5.2. Fetch length is kept constant for all simulations in this work. Hasselmann spreading function is also used to simulate angular/directional spreading of sea surface waves. 2D snapshots are obtained from 3D realizations of sea surface for simulations at Section 5.2, evolving/resulting in linear sea surface wave field in downwind direction. When compared to nonlinear evolution equations that are not used in this thesis linear evolution equations avoids the sea surface wavenumber spectrum from being affected by any round-off and aliasing errors explained in [1].

2.2 Sea Surface Waves

As stated in [25], sea surface waves are generated when a body of water is disturbed by various forces such as the gravitational pull of the sun and the moon, underwater earthquakes, landslides and the movements of boats and swimmers. However, the most common sea waves are wind-generated and occur when the air particles in the blowing wind push against the surface of smooth water, creating small ridges and

ripples due to friction. As long as the wind exists, these ripples enlarge and finally turn into waves of several meters high.

There are three factors that determine the size of the wind-generated waves. These are the wind speed, the wind duration and the distance over which the wind blows without changing direction, called fetch [25]. The waveheights increases with larger wind speeds and durations. The size of the waves increases proportionally to the fetch distance as well. This could be observed in the Beaufort scale [38] shown in Table 2.1 that presents the relation between the height of the ocean waves and the speed of the wind. However, this increase in wave size is limited since the energy of wind passed on to the water is dissipated by wave breaking after a certain point. The state that sea surface waves reach their maximum height is called as the “fully developed state of the sea” [25].

Table 2.1: Beaufort Wind Force Scale [38]

Beaufort Number	Description	Wind Speed	Wave Height	Sea Conditions	Land Conditions
0	Calm	<0.3m/s	0m	Flat.	Calm. Smoke rises vertically.
1	Light Air	0.3-1.5m/s	0-0.2m	Ripples without crests.	Smoke drift indicates wind direction. Leaves and wind vanes are stationary.
2	Light Breeze	1.6-3.3m/s	0.2-0.5m	Small wavelets. Crests of glassy appearance, not breaking	Wind felt on exposed skin. Leaves rustle. Wind vanes begin to move.
3	Gentle Breeze	3.4-5.4m/s	0.5-1m	Large wavelets. Crests begin to break; scattered whitecaps	Leaves and small twigs constantly moving, light flags extended.
4	Moderate Breeze	5.5-7.9m/s	1-2m	Small waves with breaking crests. Fairly frequent whitecaps.	Dust and loose paper raised. Small branches begin to move.
5	Fresh Breeze	8.0-10.7m/s	2-3m	Moderate waves of some length. Many whitecaps. Small amounts of spray.	Branches of a moderate size move. Small trees in leaf begin to sway.
6	Strong Breeze	10.8-13.8m/s	3-4m	Long waves begin to form. White foam crests are very frequent. Some airborne spray is present.	Large branches in motion. Whistling heard in overhead wires. Umbrella use becomes difficult. Empty plastic bins tip over.
7	Near Gale	13.9-17.1m/s	4-5.5m	Sea heaps up. Some foam from breaking waves is blown into streaks along wind direction. Moderate amounts of airborne spray.	Whole trees in motion. Effort needed to walk against the wind.
8	Gale	17.2-20.7m/s	5.5-7.5m	Moderately high waves with breaking crests forming spindrift. Well-marked streaks of foam are blown along wind direction. Considerable airborne spray.	Some twigs broken from trees. Cars veer on road. Progress on foot is seriously impeded.

9	Strong Gale	20.8-24.4m/s	7-10m	High waves whose crests sometimes roll over. Dense foam is blown along wind direction. Large amounts of airborne spray may begin to reduce visibility.	Some branches break off trees, and some small trees blow over. Construction/temporary signs and barricades blow over.
10	Storm	24.5-28.4m/s	9-12.5m	Very high waves with overhanging crests. Large patches of foam from wave crests give the sea a white appearance. Considerable tumbling of waves with heavy impact. Large amounts of airborne spray reduce visibility.	Trees are broken off or uprooted, structural damage likely.
11	Violent Storm	28.5-32.6m/s	11.5-16m	Exceptionally high waves. Very large patches of foam, driven before the wind, cover much of the sea surface. Very large amounts of airborne spray severely reduce visibility.	Widespread vegetation and structural damage likely.
12	Hurricane	>32.7m/s	>14m	Huge waves. Sea is completely white with foam and spray. Air is filled with driving spray, greatly reducing visibility.	Severe widespread damage to vegetation and structures. Debris and unsecured objects are hurled about.

According to [26] there different physical processes develop when the wind suddenly begins to blow steadily at a constant speed on the sea surface:

- Because of the turbulence caused by wind, pressure on the ocean surface starts to fluctuate randomly. These perturbations lead to form sea surface waves with in order of a few centimeters wavelengths (called as Phillips Mechanism).
- After sea surface waves with small wavelengths are formed, wind continues to blow causing sea surface waves with large wavelengths. Pressure differences along the surface waves increase when sea surface waves get larger. This leads to an unstable growth of the ocean waves. Growth speed of surface waves become an exponential function (called as Miles Mechanism).
- Finally, sea surface waves with longer wavelengths start to form due to interaction of ocean waves between themselves [7] by transferring the energy from waves with short wavelengths generated by Miles' mechanism to waves with long wavelengths. Thus peak of the sea surface wave spectrum shifts to lower frequencies (non-linear growth). The result of shift on the peak frequency of sea wave spectrum is that speed of an ocean wave component is higher than wind speed [27].

Five main stages of development of sea surface wave components are stated as the linear growth, the exponential growth, the non-linear growth, wave breaking (white capping) and quasi-equilibrium stages as stated in [24]. As shown in Figure 2.1 two more phases of physical processes involved in ocean waves' generation. Non-linear growth of sea surface waves continues by forming sharper and more unstable waves. After a certain point sea waves break and white caps form on the ocean surface. In the final stage, the sea surface wave components reach in balance which is a quasi-equilibrium state. After all physical processes ends at equilibrium phase, sea surface wave spectrum becomes “fully arisen” [25].

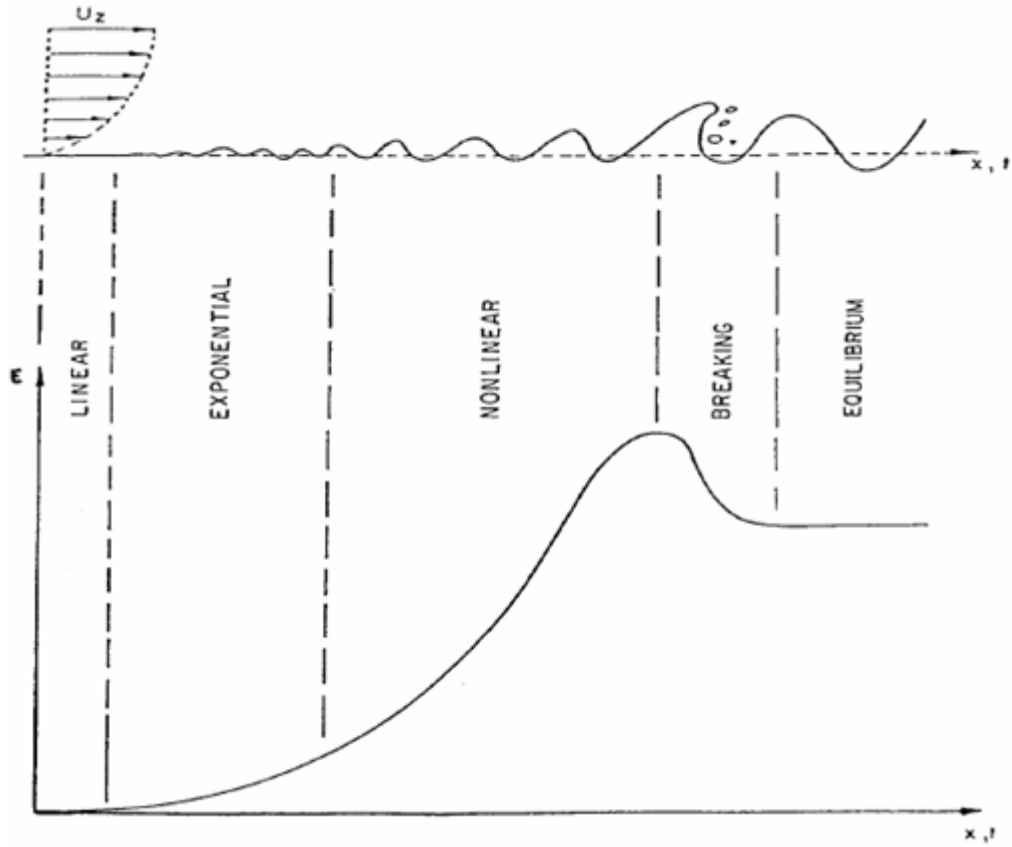


Figure 2.1: Evolution of Wind Waves Growth [25]

2.3 Concept of Sea Surface Wave Spectrum

Sea waves surface waves cannot be described as simple sinusoidal functions, since ocean waves includes random wave components such that each of them have different wavelengths, wave periods, and phases. Because of random character of sea surface wave field, it can be observed by statistical and/or spectral modeling methods. In the spectral modeling probabilistic character of the sea surface elevation is described basically. Sea surface elevation is assumed as an ergodic Gaussian stochastic process in order to construct a spectral model [25]. Concept of the spectrum of the sea surface waves relies on approach that ocean waves can be obtained by superposition of infinite number of sinusoidal waves with different amplitudes (waveheights), frequencies, phases, and direction of propagations after some simplifications. The superposition of arbitrary sinusoidal waves' leads to form of shape of rough sea surface during wind is blowing [25]. The spectrum of ocean waves shows how the wave energy is distributed on the sea surface among various wave frequencies of wavelengths.

The harmonic analysis (Fourier analysis) is a strong tool used to describe random sea surface with sinusoidal components. Rough ocean surface can be represented by a mathematical expression as follows [25]

$$\eta(t) = \sum_{n=1}^N a_n \sin(2\pi f_n t + \theta_n) \quad (2.1)$$

where,

- $\eta(t)$: Surface elevation at time t , at a fixed point
- a_n : The amplitude of n^{th} sinusoidal component
- f_n : The frequency of n^{th} sinusoidal component
- θ_n : The phase angle of n^{th} sinusoidal component
- N : Number of all possible wave components

This representation describes the harmonic analysis of wind-driven sea surface waves with some simplifications since it considers all surface wave components with a_n , f_n , and θ_n coming from various directions as an individual wave component.

There are several ideal forms of the sea surface wave spectrum which are produced by steady and homogeneous winds. The Pierson-Moskowitz [27] and JONSWAP [7] spectra are two of the most widely accepted spectrum models explained in sections below.

2.3.1 Pierson-Moskowitz Sea Surface Spectrum

The ocean wave spectrum suggested by the Pierson-Moskowitz can be considered as the simplest wave spectrum. The principal assumption is that the sea surface waves reach an equilibrium state when a large area of ocean surface is exposed to steady wind blowing for a long time. This state is called as “fully developed” sea as stated earlier and Pierson-Moskowitz sea surface wave spectrum is valid for this state of seas [26].

Several measurements are made in North Atlantic by Pierson and Moskowitz and these measurements are used in order to acquire a “fully developed” sea surface spectrum [27]. Sea surface wave’s data are collected when steady wind blows for a long time over large areas of North Atlantic by Pierson and Moskowitz. Then spectrum of the ocean waves is computed by using the collected data for various wind speeds as illustrated in Figure 2.2.

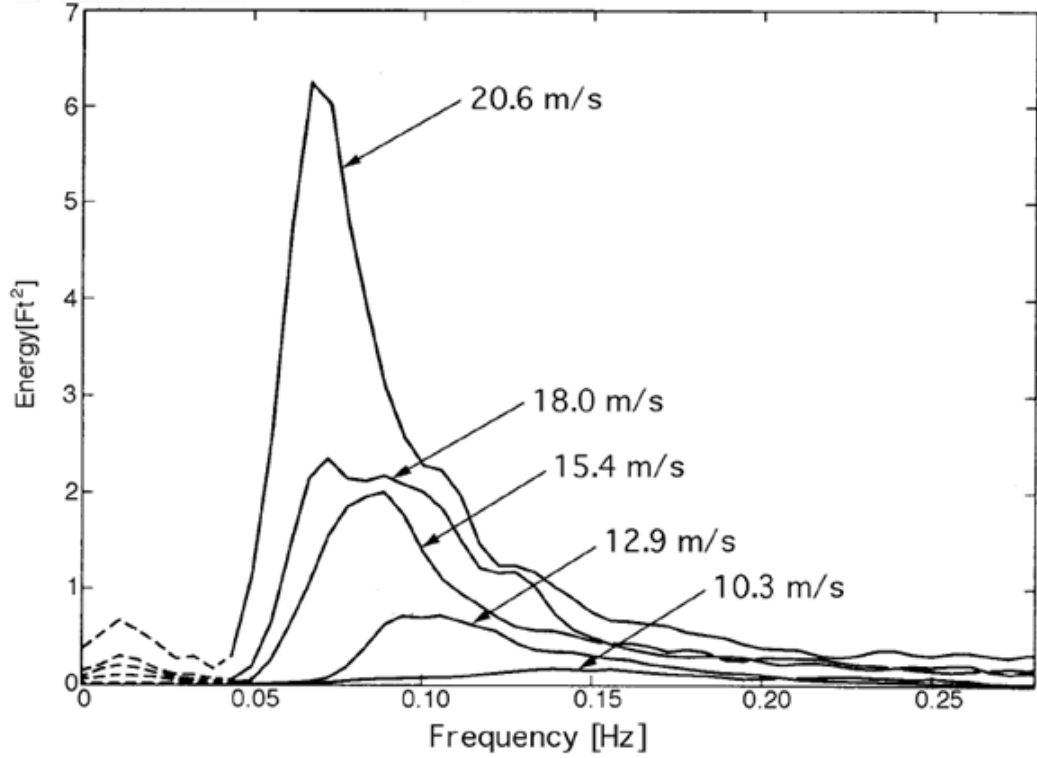


Figure 2.2: Wave Spectra of a Fully Developed Sea for Different Wind Speeds According to Moskowitz (1964) [26]

A characterization of wind-driven sea surface waves is provided by the Pierson-Moskowitz spectrum [26]

$$S(\omega) = \frac{2\pi\alpha g^2}{\omega^5} \exp\left(\frac{-5}{4} \left(\frac{\omega_p}{\omega}\right)^4\right) \quad (2.2)$$

where $\omega_p = \frac{0.26\pi g}{U}$ is angular frequency of peak of the spectrum, U represents wind velocity, $g = 9.81 \text{ m/s}^2$ (acceleration of gravity), and $\alpha = 8.1 \times 10^{-3}$ is Philip's constant.

The quantity $T_p = \frac{2\pi}{\omega_p} = \frac{U}{0.13g}$ stands for the period of the peak sea surface spectrum.

The main aim of the Pierson-Moskowitz spectrum is to represent a “fully developed” wind generated sea surface and it lies in the valid interval of $10 \frac{m}{s} < U < 20 \frac{m}{s}$. In the scope of this study, sea surface waves formed by wind speeds smaller than 10 m/s are also considered. It is one of the reasons for why Pierson-Moskowitz sea

surface wave spectrum is not used in this thesis to construct ocean surface realizations.

2.3.2 JONSWAP Sea Surface Spectrum

Another spectral model to describe sea surface waves is JONSWAP (Joint North Sea Wave Observation Project) spectrum which is suggested by Hasselmann et al. [7]. Data gathered during JONSWAP analyzed and it is figured out that sea is never “fully developed” because the sea surface wave spectrum keeps developing through non-linear interactions of ocean waves between themselves even when wind blows over very long times and distances. Therefore based on observations of JONSWAP, a sea surface wave spectrum proposed as illustrated in Figure 2.3 [26].

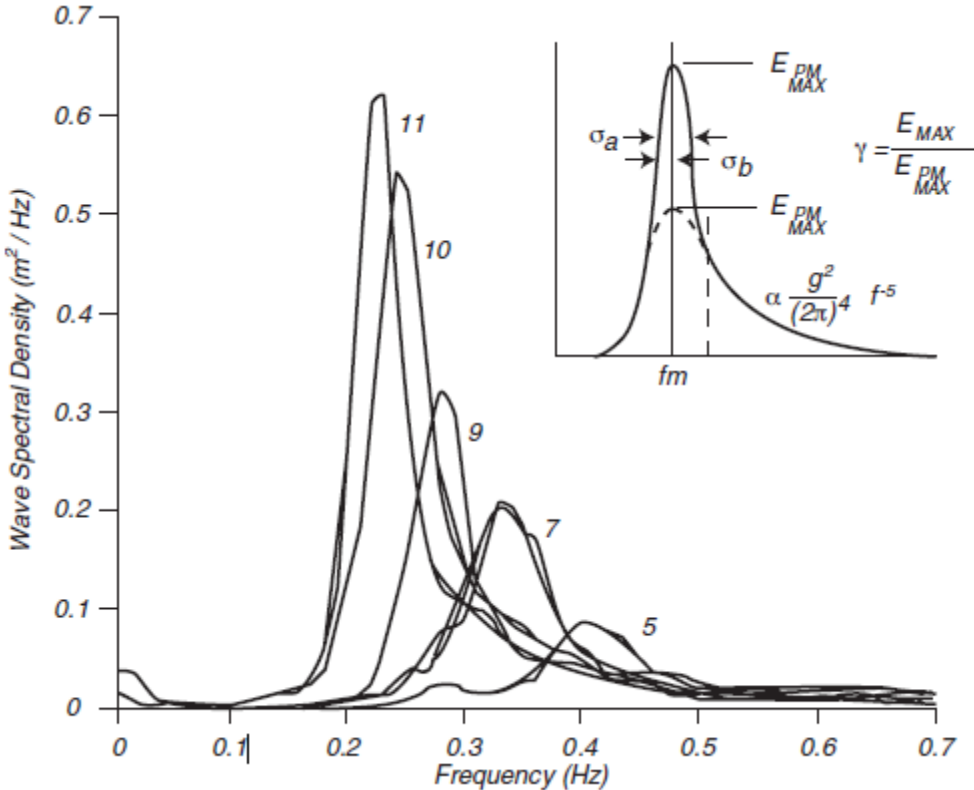


Figure 2.3: Wave Spectra of Developing Sea for Different Fetches According to Hasselmann et al. (1973) [26]

JONSWAP is a very appropriate surface wave spectrum model to model rough ocean surface for this thesis, because it can create realistic sea surface waves especially for shallow without any restriction for the wind speed interval. JONSWAP spectrum provides a relationship between frequency distribution of sea surface waves and wind velocity assuming that fetch is limited [7]. The JONSWAP spectrum is stated in the following form [26]

$$S(\omega) = \alpha g^2 \omega^{-5} \exp \left[\frac{-5}{4} \left(\frac{\omega}{\omega_p} \right)^{-4} \right] \gamma^\delta \quad (2.3)$$

where ω is the angular frequency, g is the gravitational acceleration, and δ is a peak enhancement factor given by

$$\delta = \exp \left[-\frac{(\omega - \omega_p)^2}{2\sigma_0^2 \omega_p^2} \right] \quad (2.4)$$

The parameters γ and σ_0 are given as $\gamma = 3.3$, $\sigma_0 = 0.07$ for $\omega < \omega_p$ and $\sigma_0 = 0.09$ for $\omega > \omega_p$, while α is function of fetch X (the distance over which the wind blows with constant velocity) and wind speed U :

$$\alpha = 0.076 \left(\frac{gX}{U} \right)^{-0.22} \quad (2.5)$$

Similar to the Pierson-Moskowitz spectrum, the JONSWAP spectrum provides a special function to compute the peak frequency of the wave spectrum such that

$$\omega_p = 7\pi \left(\frac{g}{U} \right) \left(\frac{gX}{U^2} \right)^{-0.33} \quad (2.6)$$

JONSWAP spectrum is similar to Pierson-Moskowitz spectrum in terms of wave energy distribution, but it has a little higher peak frequency with respect to Pierson-Moskowitz sea surface wave spectrum. In addition, for JONSWAP spectrum sea surface waves always continue to grow with time specified by the α term [26].

JONSWAP rough ocean surface spectrum is considered to be an improved version of the Pierson-Moskowitz spectrum to model sea waves in a realistic manner.

2.3.3 Angular/Directional Spreading

The wave energy at any point on the sea surface has an angular distribution termed as “angular/directional spreading” and frequency distribution. Spectral representations which include both of these distributions are called as "directional spectrum" [22]. It is essential to know the directional spectrum of evolving sea surface waves especially in shallow water to obtain more precise predictions. Spectral models without combining with “directional spreading” lead to estimate higher sea surface waveheights (approximately 20 percent).

“Directional spreading” is used to describe wind generated sea surface wave flow velocities accurately by representing distribution of energy of ocean waves correctly. If angular spreading is not considered, flow velocities are estimated to be higher as well [22]. Some of the most widely used spreading functions are presented in the following sections.

2.3.3.1 Cosine-Squared Spreading Function

The cosine-squared sea surface spreading (which is independent of frequency) is given by the expression [16]

$$G(\theta) = \begin{cases} \frac{2}{\pi} \cos^2(\theta - \bar{\theta}) & \left(\frac{-\pi}{2} + \bar{\theta}\right) < \theta < \left(\frac{\pi}{2} + \bar{\theta}\right) \\ 0 & \text{otherwise} \end{cases} \quad (2.7)$$

where $\bar{\theta}$ is mean wave direction (in radians).

This is a strongly non-isotropic directional spreading function since it calculated as zero except in the interval $|\theta - \bar{\theta}| < \pi/2$.

2.3.3.2 Donelan Spreading Function

Another frequency independent spreading function is suggested by Donelan et al. Compact form of Donelan spreading function [28] is described by

$$G(\theta) = \frac{\beta}{2} \operatorname{sech}^2(\beta(\theta - \bar{\theta})) \quad (2.8)$$

where $\bar{\theta}$ is the mean wave direction and

$$G = \begin{cases} 2.61 \left(\frac{\omega}{\omega_p}\right)^{1.3} & 0.56 < \frac{\omega}{\omega_p} < 0.95 \\ 2.28 \left(\frac{\omega}{\omega_p}\right)^{-1.3} & 0.95 < \frac{\omega}{\omega_p} < 1.6 \\ 1.24 & \text{otherwise} \end{cases} \quad (2.9)$$

2.3.3.3 Mitsayusu Spreading Function

The Mitsayusu sea surface directional spreading function [20] is a frequency dependent approach expressed as

$$G(\omega, \theta) = \frac{\Gamma(s+1)}{2\sqrt{\pi}\Gamma(s+0.5)} \cdot \left(\cos^2 \frac{\theta}{2}\right)^s \quad (2.10)$$

where $\Gamma(s)$ stands for the Gamma function; the parameter s controls the angular distribution of energy along frequency as follows:

$$s = \begin{cases} 9.77 \cdot \left(\frac{\omega}{\omega_p}\right)^{-2.5} & \omega \leq \omega_p \\ 6.97 \cdot \left(\frac{\omega}{\omega_p}\right)^5 & \omega \geq \omega_p \end{cases} \quad (2.11)$$

The definition of s reflects that it increases in vicinity of the peak spectral frequency and decreases at frequencies lower than peaks frequency of the wave spectrum [16]. Expression of Mitsayusu spreading function gives the energy of a wave with angular frequency ω that is travelling under an angle θ relative to the direction of the wind.

2.3.3.4 Hasselmann Spreading Function

This is another spreading function that relies on frequency proposed by Hasselmann et al. [21] and is stated as

$$G(\omega, \theta) = \frac{1}{N_p} \left[\cos^2 \left(\frac{\theta - \bar{\theta}}{2} \right) \right]^p \quad (2.12)$$

Data collected from surface wave measurements are fitted an analytical expression in order to obtain the following dependence of the parameters on frequency through a maximum likelihood technique given as in [16]

$$p = 9.77 \left(\frac{\omega}{\omega_p} \right)^\mu \quad (2.13)$$

and

$$\mu = \begin{cases} 4.06 & \omega < \omega_p \\ -2.34 & \omega > \omega_p \end{cases} \quad (2.14)$$

the corresponding normalization factor is

$$N_p = 2^{1-2p} \pi \frac{\Gamma(2p+1)}{\Gamma^2(2p+1)} \quad (2.15)$$

where $\Gamma(p)$ denotes Gamma function as well.

There are two factors that differentiate the Hasselmann spreading function from the usual cosine-squared distribution [39]. First, the profile generated around the peak frequency in the downwind (in the direction of wind which steadily blows) of the spectrum is narrower. This modification fits with additional experimental evidence. Secondly, Hasselmann spreading function reduces the peak frequency of the wave spectrum. Then a bimodal spectrum shape is formed for angles that are near 90° from downwind. Thus all frequency (peak and non-peak) components of the sea surface wave spectrum are maintained.

2.4 Construction Steps for 2D and 3D Sea Surface Wave Fields

2.4.1 Frequency to Wavenumber Conversion in 2D

The spectra of ocean waves are described in the frequency domain. In order to use in acoustic propagation models it is better to define the rough sea surface based on space instead of time. Due to that reason the wavenumber domain needs to be used for defining the ocean spectra [16]. Wavenumber spectrum of the sea surface wave field can be obtained by using frequency spectrum, because wave energy under both curves is equal to each other. This energy equality is given as

$$S_{\omega} \frac{d\omega}{dk} = S_k(k) \quad (2.16)$$

where S_k is wavenumber spectrum. In order to describe the relationship between ω and k “dispersion relation” [1] is utilized

$$\omega^2 = gk \tanh(kh) \quad (2.17)$$

by using dispersion relation the expression for group velocity found as

$$\frac{d\omega}{dk} = C_g = \frac{1}{2} \left(1 + \frac{2kh}{\sinh(2kh)} \right) \frac{\omega}{k} \quad (2.18)$$

Wavenumber spectrum can be obtained from Equations (2.16) and (2.18).

In general, an increase in wind speed leads to lower the peak of the wavenumber spectrum and longer the sea surface wavelengths. In other words, as wind speed gets higher, waves propagate with lower frequencies and higher amplitudes beside of more energy transmission to the ocean [25].

2.4.2 Directional Wave Spectra

In order to model sea surface wave field directivity of the wind is integrated with frequency spectrum of the ocean surface by using a spreading function. It is provided

in terms directional wave spectra in this thesis. Directional wave spectra $S(k, \theta)$ can be described by

$$S(k, \theta) = S_k(k)G(\omega, \theta) \quad (2.19)$$

where S_k is the wavenumber spectrum described by Equation (2.16) and $G(\omega, \theta)$ (ω is included if G is frequency dependent) is the directional spreading function.

Given that the total energy in the directional as well as the one-dimensional spectrum must be equal, function $G(\omega, \theta)$ depends on the condition stated as

$$\int_{-\infty}^{\infty} \int_{-\pi}^{\pi} S_k(k)G(\omega, \theta) d\theta dk = \int_{-\infty}^{\infty} S_k(k) dk \quad (2.20)$$

2.4.3 Construction of Initial Surface Wave Field in 2D

In order to acquire nodal amplitudes for each dk , energy equality is used after computing the wavenumber spectrum [1]

$$\frac{1}{2} a_r^2 = S_k(k_r) dk \quad (2.21)$$

where $r = 0, 1, \dots, \frac{N}{2}$, $k_r = rdk$, $dk = \frac{2\pi}{L}$ and L is length of the computational sea surface domain. N stands for total number of wave components and it is chosen as power of 2 to be able to use Fast Fourier Transforms (FFT). Later on, based on the symmetry relation, two sided amplitude spectrum is generated by using the one sided amplitude spectrum

$$a_s = a_{N-s} \quad (2.22)$$

where $s = \frac{N}{2} + 1, \frac{N}{2} + 2, \dots, N - 1$.

for $r = 0, 1, \dots, \frac{N}{2}$ uniformly distributed random phases θ_r with the values in the interval of $[0, 2\pi]$ are generated. By using the symmetry relation given by Equation (2.22) for phases in this case, symmetric random phases θ_j are obtained for $j = -\frac{N}{2} + 1, -\frac{N}{2} + 2, \dots, \frac{N}{2}$.

Complex amplitudes, A , are computed using real amplitudes and random phases which are stated in Equation (2.21) and Equation (2.22) respectively

$$A_j = \frac{a_j \exp(i\theta_j)}{2} \quad (2.23)$$

where $j = -\frac{N}{2} + 1, -\frac{N}{2} + 2, \dots, \frac{N}{2}$, $i = \sqrt{-1}$ and θ_j denotes the symmetric uniformly distributed random phase shifts in interval of $[0, 2\pi]$.

Initial surface elevation can be calculated depending on complex amplitudes in Equation (2.23) such as

$$\eta_p = \sum_{j=-N/2+1}^{N/2} A_j \exp(ik_j x_p) \quad (2.24)$$

where $p = 0, 1, \dots, N - 1$, $x_p = p dx$, $dx = \frac{L}{N}$ and L is length of the 2D sea surface.

The complex amplitudes in order to construct the surface velocity potential, ϕ^s are also obtained in a similar manner given by

$$B_j = -\frac{ig a_j}{\omega_j} \exp(i\theta_j) \quad (2.25)$$

where ω_j are discrete angular frequencies obtained from Equation (2.17) for discrete wavenumbers, k_j , and g denotes the gravitational acceleration.

By using complex amplitudes given in Equation (2.25) the initial sea surface velocity potential can be attained and expressed as

$$\phi_p^s = \sum_{j=-N/2+1}^{N/2} B_j \exp(ik_j x_p) \quad (2.26)$$

for $p = 0, 1, \dots, N - 1$.

It is necessary for the complex amplitudes $A(k)$ and $B(k)$ to be complex conjugates of $A(-k)$ and $B(-k)$ to obtain real values for η and ϕ^s . If that condition is provided, real values of η and ϕ^s is computed by using Inverse Fast Fourier Transform to solve Equation (2.24) and Equation (2.26).

2.4.4 Construction of Initial Surface Wave Field in 3D

The directional wave spectrum $S(k, \theta)$ can be generated using Equation (2.19) and one of the spreading function equations (2.7, 2.8, 2.10, and 2.12) in order to construct sea surface wave field with two horizontal directions. Derivation of the sea surface wavenumber spectrum component amplitudes is discussed shortly in this section. These complex amplitudes are used to construct initial sea surface by using Inverse Fourier Transform technique. In order to take advantage of that technique directional wave spectrum, $S(k, \theta)$, is transformed to wavenumber spectrum, $S_{k_x k_y}(k_x, k_y)$, which is a function of wavenumber components along x and y axes (k_x and k_y). Then again using feature that energy is equal under surfaces of $S(k, \theta)$ and $S_{k_x k_y}(k_x, k_y)$. Transformation is done based on this consideration such as

$$S_{k_x k_y}(k_x, k_y) = \frac{S(k, \theta)}{|J|} \quad (2.27)$$

where $|J|$ stands for the Jacobean of the transformation which is defined by

$$|J| = \begin{vmatrix} \cos\theta & \sin\theta \\ -k\sin\theta & k\cos\theta \end{vmatrix} = k \quad (2.28)$$

Having $S_{k_x k_y}(k_x, k_y)$, component amplitudes for each $dk_x dk_y$ interval can be computed by equality of energy given as

$$\frac{1}{2} a_{p,r}^2 = S_{k_x k_y}(k_{xp}, k_{yr}) dk_x dk_y \quad (2.29)$$

where $p = 0, 1, \dots, \frac{N_x}{2}$, $r = 0, 1, \dots, \frac{N_y}{2}$, $k_{xp} = p dk_x$, $k_{yr} = r dk_y$, $dk_x = \frac{2\pi}{L_x}$, and $dk_y = \frac{2\pi}{L_y}$. N_x and N_y denote the total number of wave components along x and y directions respectively. Similarly, L_x and L_y are lengths of computational sea surface domain in x and y directions respectively. Both N_x and N_y are taken as power of 2 in order to use 2D Fast Fourier Transforms.

Next, the one-sided component amplitudes are mirrored about $\frac{N_x}{2}$ and $\frac{N_y}{2}$ to construct the two-sided amplitude spectrum given by symmetry relation below

$$a_{s,u} = a_{N_x-s, N_y-u} \quad (2.30)$$

where $s = \frac{N_x}{2} + 1, \frac{N_x}{2} + 2, \dots, N_x - 1$ and $u = \frac{N_y}{2} + 1, \frac{N_y}{2} + 2, \dots, N_y - 1$.

For $p = 0, 1, \dots, \frac{N_x}{2}$ and $r = 0, 1, \dots, \frac{N_y}{2}$ uniformly distributed random phases $\theta_{p,r}$ are produced in the interval of $[0, 2\pi]$. By using the symmetry relation again in Equation (2.30) for random phases in this case, mirrored random phases $\theta_{j,n}$ are obtained for $j = -\frac{N_x}{2} + 1, -\frac{N_x}{2} + 2, \dots, \frac{N_x}{2}$ and $n = -\frac{N_y}{2} + 1, -\frac{N_y}{2} + 2, \dots, \frac{N_y}{2}$.

For computing complex amplitudes, A , real amplitudes that are obtained by Equations (2.29) and (2.30) are used. In addition to real amplitudes, uniformly distributed random phases with values between 0 and 2π are also utilized to construct the rough sea surface leading the equation given by

$$A_{j,n} = \frac{a_{j,n} \exp(i\theta_{j,n})}{2} \quad (2.31)$$

where $j = -\frac{N_x}{2} + 1, -\frac{N_x}{2} + 2, \dots, \frac{N_x}{2}$, $n = -\frac{N_y}{2} + 1, -\frac{N_y}{2} + 2, \dots, \frac{N_y}{2}$. At next step, initial sea surface elevation is obtained based on computed complex amplitudes, $A_{j,n}$, given as

$$\eta_{v,q} = \sum_{j=-N_x/2+1}^{N_x/2} \sum_{n=-N_y/2+1}^{N_y/2} A_{j,n} \exp(ik_j x_v + ik_n y_q) \quad (2.32)$$

where $v = 0, 1, \dots, N_x - 1$, $q = 0, 1, \dots, N_y - 1$, $x_v = v dx$, $y_q = q dy$, $dx = \frac{L_x}{N_x}$, and $dy = \frac{L_y}{N_y}$.

Complex amplitudes, $B_{j,n}$, to generate initial surface velocity potential, ϕ^s , are obtained in a similar manner stated as

$$B_{j,n} = -\frac{ig}{\omega_{j,n}} \frac{a_{j,n}}{2} \exp(i\theta_{j,n}) \quad (2.33)$$

Finally, the initial surface velocity potential is obtained by equation given as

$$\phi^s_{v,q} = \sum_{j=-N_x/2+1}^{N_x/2} \sum_{n=-N_y/2+1}^{N_y/2} B_{j,n} \exp(ik_j x_v + ik_n y_q) \quad (2.34)$$

where $v = 0, 1, \dots, N_x - 1$ and $q = 0, 1, \dots, N_y - 1$.

It is necessary for the complex amplitudes $A(k_x, k_y)$ and $B(k_x, k_y)$ to be complex conjugates of $A(-k_x, -k_y)$ and $B(-k_x, -k_y)$ to obtain real values for η and ϕ^s . If that condition is provided, real values of η and ϕ^s is computed by using 2D Inverse Fast Fourier Transform to solve Equation (2.32) and Equation (2.34).

In this thesis, 3D sea surfaces are constructed but only 2D downwind cross-sections of ocean waves are used in simulations in Chapter 5. Thus a more realistic representation of ocean wave field is provided without constructing sea surface waves with exaggerated waveheights.

2.5 Governing Equations for the Surface Wave Model

In this thesis, the evolution equations given by [1] and [13] are followed which are solution of the classical boundary value problem for sea surface waves in a constant depth of h . Main assumptions in this solution are that water flow is inviscid, incompressible, and irrotational. Due these assumptions if ϕ satisfies the governing equation for water flow (Laplace's equation), there exists a velocity potential $\phi(\vec{x}, z, t)$. $\vec{x} = (x, y)$ stands for the horizontal position vector. Following [1], the surface velocity potential is used in this study stated as

$$\phi^S(\vec{x}, t) = \phi(\vec{x}, \eta(\vec{x}, t), t) \quad (2.35)$$

at $z = \eta(\vec{x}, t)$. η is the sea surface elevation from the flat sea surface when state of the sea is calm. The classical kinematic and dynamic boundary conditions at the free sea surface are found by chain rule differentiation and they are expressed in terms of surface velocity potential, ϕ^S , given as

$$\eta_t + \nabla_h \phi^S \cdot \nabla_h \eta - (1 + \nabla_h \eta \cdot \nabla_h \eta) \phi_z(\vec{x}, \eta, t) = 0 \quad (2.36)$$

$$\phi_t^S + g\eta + \frac{1}{2} \nabla_h \phi^S \cdot \nabla_h \phi^S - \frac{1}{2} (1 + \nabla_h \eta \cdot \nabla_h \eta) \phi_z^2(\vec{x}, \eta, t) = -\frac{P_a}{\rho} \quad (2.37)$$

where $\nabla_h = (\partial/\partial x, \partial/\partial y)$ is the horizontal gradient and t is time. P_a denotes the atmospheric pressure and ρ stands for the fluid density.

Equation (2.36) and Equation (2.37) are the nonlinear evolution equations of sea surface waves. Since numerical solution of nonlinear evolution equations suffers from errors like aliasing errors, amplification of round-off errors etc. stated in [1], it is used linear evolution equations in this thesis.

Gage pressure, P_a , in Equation (2.37) is taken to be zero. Then, by making linear the evolution equations in Equation (2.36) and Equation (2.37), linear evolution equations at $z = 0$ are obtained in the form given as

$$\eta_t - \phi^S_z = 0 \quad (2.38)$$

$$\phi^S_t + g\eta = 0 \quad (2.39)$$

Starting with initial sea surface wave field, η (sea surface fluctuation) and ϕ^S (sea surface velocity potential), linear evolution equations given in Equation (2.38) and Equation (2.39) are solved by the fourth-order Runge-Kutta time integrator. A general description of the fourth-order Runge-Kutta method is expressed in Section 2.5.1.

2.5.1 Fourth Order Runge-Kutta Method

General description of fourth-order Runge-Kutta method (*RK4*) is stated with following algorithm steps [42]. If a first order differential equation problem is considered such as

$$\begin{cases} y' = f(t, y) \\ y(t_0) = \alpha \end{cases} \quad (2.40)$$

Δt is defined as constant time step size and $t_i = t_0 + i\Delta t$, where i is a nonnegative integer. Then the steps of *RK4* method in Equation (2.41) are followed in order to compute an approximate solution, that is $w_i \approx y(t_i)$.

$$w_0 = \alpha$$

$$c_1 = \Delta t f(t_i, w_i)$$

$$c_2 = \Delta t f\left(t_i + \frac{\Delta t}{2}, w_i + \frac{c_1}{2}\right) \quad (2.41)$$

$$c_3 = \Delta t f\left(t_i + \frac{\Delta t}{2}, w_i + \frac{c_2}{2}\right)$$

$$c_4 = \Delta t f(t_i + \Delta t, w_i + c_3)$$

$$w_{i+1} = w_i + \frac{1}{6}(c_1 + 2c_2 + 2c_3 + c_4)$$

2.6 Calculation of Surface-Normal Velocity

The velocity component in the direction normal to the surface is essential in computing the Doppler shift [1]. The surface-normal velocity can be obtained by using the sea surface wave model discussed in this chapter.

Having surface velocity potential ϕ^S as a function of spatial variables x and y at a given instant of time, field of the surface velocity potential at the 3D sea surface is obtained by

$$\vec{u} = (\phi^S_x, \phi^S_y, \phi_z|_{z=\eta}) \quad (2.42)$$

Path of a particle at the sea surface occurred by surface wave motion can be described by function

$$F = z - \eta \quad (2.43)$$

Hence outward normal to the sea surface is described as

$$\vec{n} = \left(\frac{F_x, F_y, F_z}{\sqrt{F_x^2 + F_y^2 + F_z^2}} \right) = \left(\frac{-\eta_x, -\eta_y, 1}{\sqrt{\eta_x^2 + \eta_y^2 + 1}} \right) \quad (2.44)$$

Therefore the surface-normal velocity, v , can be described as dot product of surface velocity potential field at the sea surface and outward sea surface normal given by

$$\begin{aligned}
v = \vec{u} \cdot \vec{n} &= \left(\phi_x^S, \phi_y^S, \phi_z|_{z=\eta} \right) \cdot \left(\frac{-\eta_x, -\eta_y, 1}{\sqrt{\eta_x^2 + \eta_y^2 + 1}} \right) \\
&= \left(\frac{-\eta_x \phi_x^S, -\eta_y \phi_y^S, \phi_z|_{z=\eta}}{\sqrt{\eta_x^2 + \eta_y^2 + 1}} \right)
\end{aligned} \tag{2.45}$$

where ϕ_x^S , ϕ_y^S , and ϕ_z^S are calculated by pseudo-spectral approach by making use of Fast-Fourier and Inverse Fast-Fourier transforms between physical space and wavenumber space when the linear evolution equations of sea surface are used. For 2D ocean surface Equation (2.45) reduces to

$$v = \vec{u} \cdot \vec{n} = \left(\frac{-\eta_x \phi_x^S, \phi_z|_{z=\eta}}{\sqrt{\eta_x^2 + 1}} \right) \tag{2.46}$$

Doppler shift calculations of the acoustic eigenrays are made by utilizing Equation (2.46) in order to compute the surface-normal velocity in Chapter 3.

2.7 Swell

According to the physical oceanographers, surface waves take two separate forms as sea waves and swells [25]. Sea waves are said to be the waves with shorter periods that are still being produced by winds or are quite near to the point of origin. Whereas swells refer to waves that are far from the area where they were generated and are also away from the winds that caused them. Swells have longer wavelengths and are more stable in direction and frequency when compared to sea waves. They are usually generated by storms thousands of nautical miles away from the areas where they are observed. Swells that travel large distances to coast become more stable and clean, with smooth, well-defined crests and relatively longer periods.

Swells can be idealized as single-tone periodic perturbations of the sea surface, whose phase changes progressively over time; therefore surface fluctuation η can be modeled simply as [16]

$$\eta(r, t) = A \sin(kr + \phi(t)) \quad (2.47)$$

where A , k and $\phi(t)$ stand for amplitude, wavelength and phase of swell, respectively. And r represents range for two-dimensional cylindrical coordinates.

In this thesis, it is only interested in sea waves which have shorter wavelengths and more random structure. Swells can also be taken into account in future works for double-peaked sea surface wave spectrum which involves both swells and sea waves at the same time.

2.8 2D Linear Sea Surface Wave Model

When linear wave equations in Equation (2.38) and Equation (2.39) are solved using fourth order Runge-Kutta method with a constant time step similar to [1] and [13], time-evolving linear sea surface waves with various times can be obtained. Linear equations are solved starting with construction of initial sea surface fluctuation ($\eta(\vec{x}, t_0)$) and sea surface velocity potential ($\phi^s(\vec{x}, t_0)$). Figure 2.4 illustrates a snapshot of propagating linear waves where sea surface fluctuation, η , is plotted as a function of propagation axis, x .

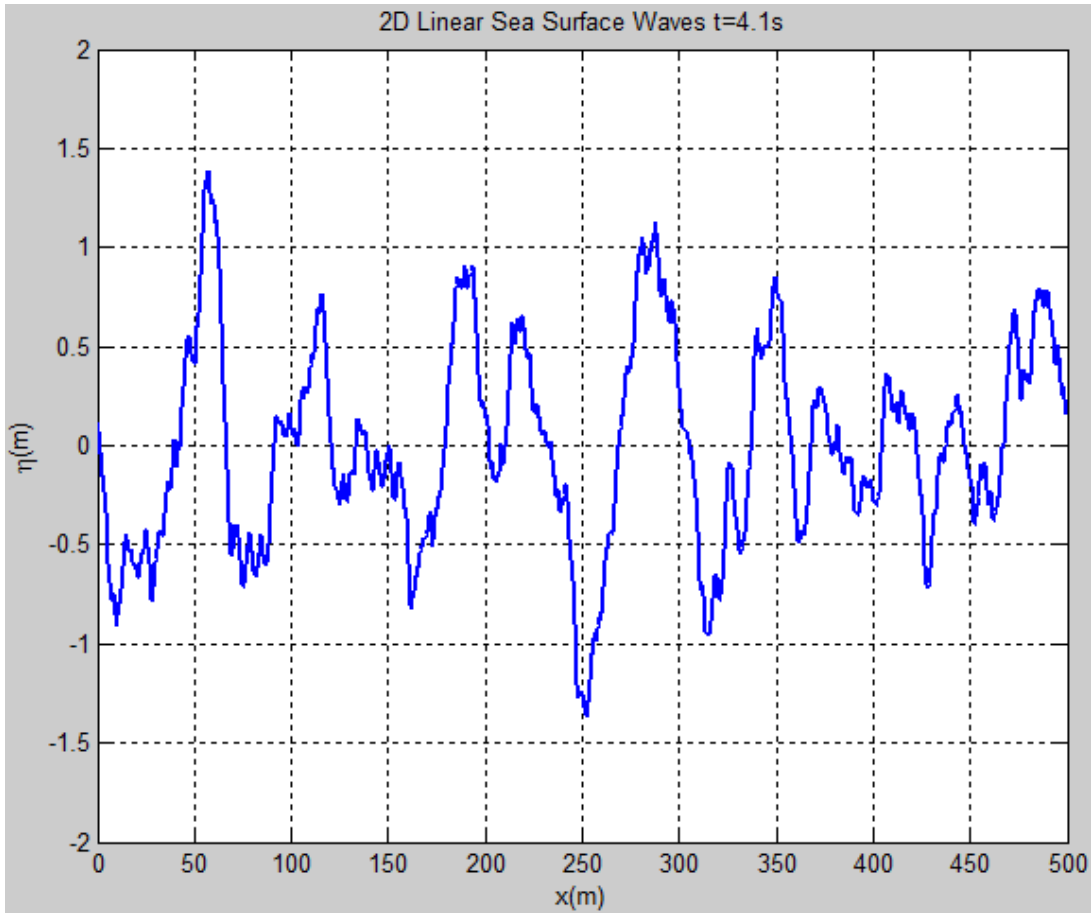


Figure 2.4: 2D Linear Sea Surface Wave Snapshot (N=1024)

The snapshot shown in Figure 2.4 is constructed by using JONSWAP spectrum given in Equations (2.3)-(2.6). Wind speed, U , is taken as 14 m/s which is 10 m above the calm sea surface and fetch, X , is taken as 100 km . Water depth, h , is chosen as 40 m in order to validate shallow water approximation.

The accuracy of the linear sea surface wave model is confirmed by two methods. First method is based on comparing the input wavenumber spectrum of the sea surface wave model and wavenumber spectrum of the sea surface waves marched in time. Output wavenumber spectrum can be obtained by using Fourier analysis. Second check depends on comparing the input and output variances of sea surface wave fluctuations.

Result of the first accuracy check can be seen in Figure 2.5. Since input energy is preserved in linear sea surface wave model without suffering errors seen in nonlinear wave models in [1], an ideal match of input and output wavenumber spectra occurs.

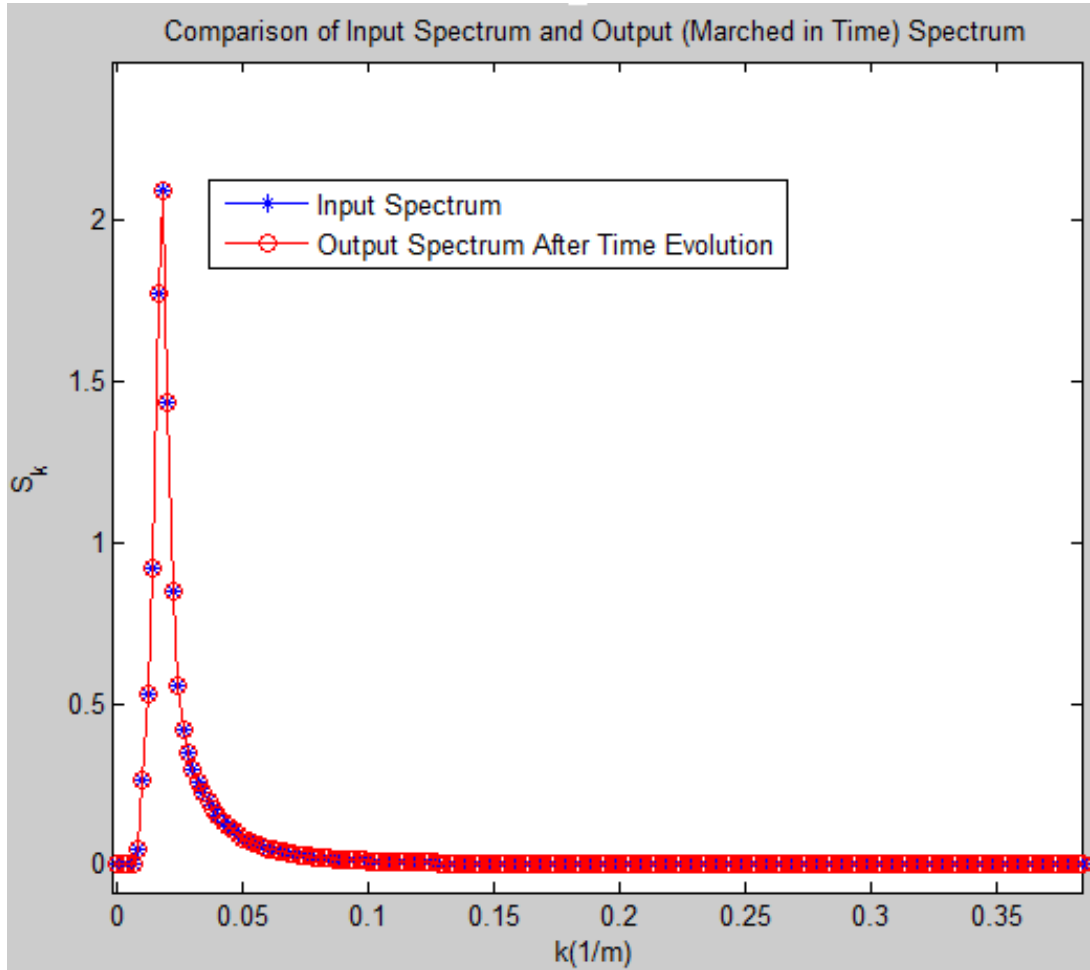


Figure 2.5: Input and Output Wavenumber Spectra Comparison

Input variance is given by

$$\sigma^2_{input} = \int_0^{\infty} S(\omega) d\omega \quad (2.48)$$

Output variance of sea surface wave fluctuation which is obtained after that sea surface waves are marched in time. Output variance is computed by

$$\sigma^2_{output} = \frac{1}{N} \sum_{j=1}^N (\eta_j - \bar{\eta})^2 \quad (2.49)$$

where

$$\bar{\eta} = \frac{1}{N} \sum_{j=1}^N \eta_j \approx 0 \quad (2.50)$$

For wavenumber spectrum given in Figure 2.5 input and output variances lead to the same result, $0.2598m^2$. Error between two variances is in order of $10^{-3}m^2$. Second accuracy check also depicts energy conservation of linear sea surface wave model. Different input spectra that are imported into linear sea surface wave model have same order of magnitude of error. Increase in the number of sea surface wave components (N) results in less error between input and outputs variances because sea surface wave field is represented more accurately as N is a higher value.

2.9 3D Linear Sea Surface Wave Model

In order to generate evolution of 3D sea surface waves, linear wave equations given in Equation (2.38) and Equation (2.39) are used again. Hasselmann spreading function in Section 2.2.3.4 is used to obtain directional wave spectrum. The process starts by computing initial sea surface fluctuation ($\eta(\vec{x}, t_0)$) and velocity potential ($\phi^s(\vec{x}, t_0)$). Then, numerical integrations for linear sea surface wave equations are provided by fourth-order Runge-Kutta time integrator.

In 3D linear sea surface wave model principal direction of sea surface waves can lie in $0^\circ - 360^\circ$ interval. This direction of sea surface wave field depends on the main direction of wind which is defined counter-clockwise sense with respect to x axis.

The plots in Figure 2.6-Figure 2.11 show three snapshots of time-evolving 3D linear sea surface wave realizations. In Figure 2.6 and Figure 2.7 sea surface wave propagation direction is considered to be as 0° . Figure 2.8 and Figure 2.9 are snapshots for principal wind direction of 45° . Whereas sea surface waves in Figure 2.10 and Figure 2.11 propagate in 90° direction with respect to x axis.

The sea surface waves in Figure 2.6- Figure 2.11 are constructed by using the wave model with JONSWAP spectrum given in Equation (2.3)-Equation (2.6). Wind speed, U , is given as 10 m/s and fetch, X , is given as 100 km . Water depth, h , is used as 40 m in simulations plotted in these figures.

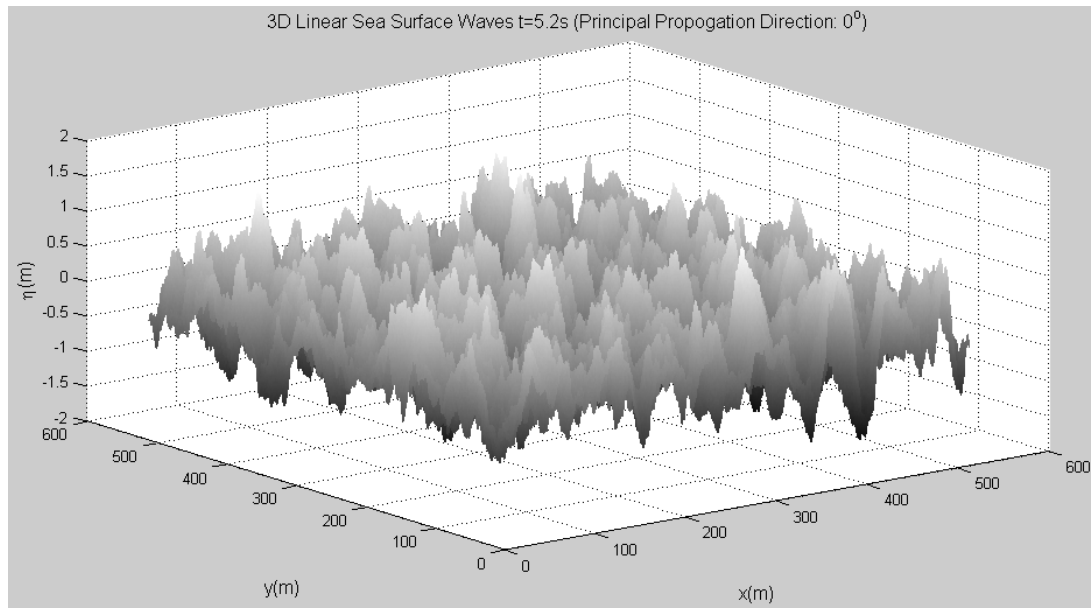


Figure 2.6: 3D Linear Sea Surface Waves Snapshot (Main Wind Direction: 0°)

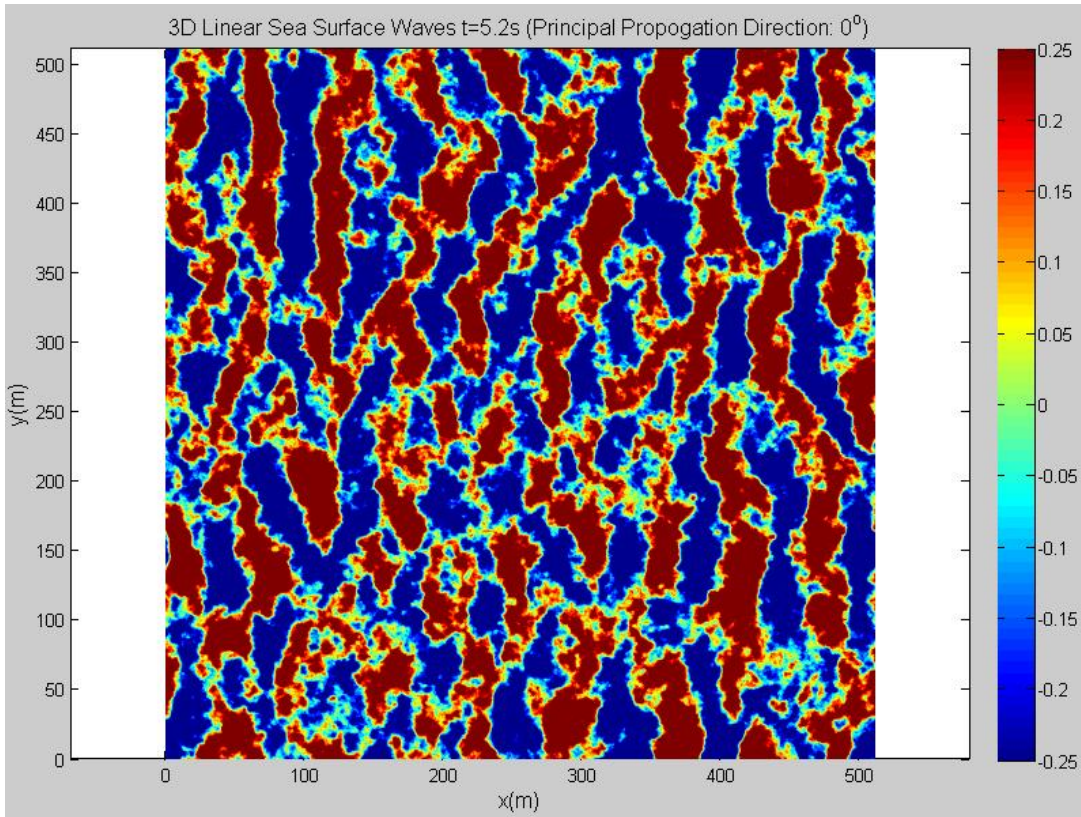


Figure 2.7: 3D Linear Sea Surface Waves Snapshot (Main Wind Direction: 0°)

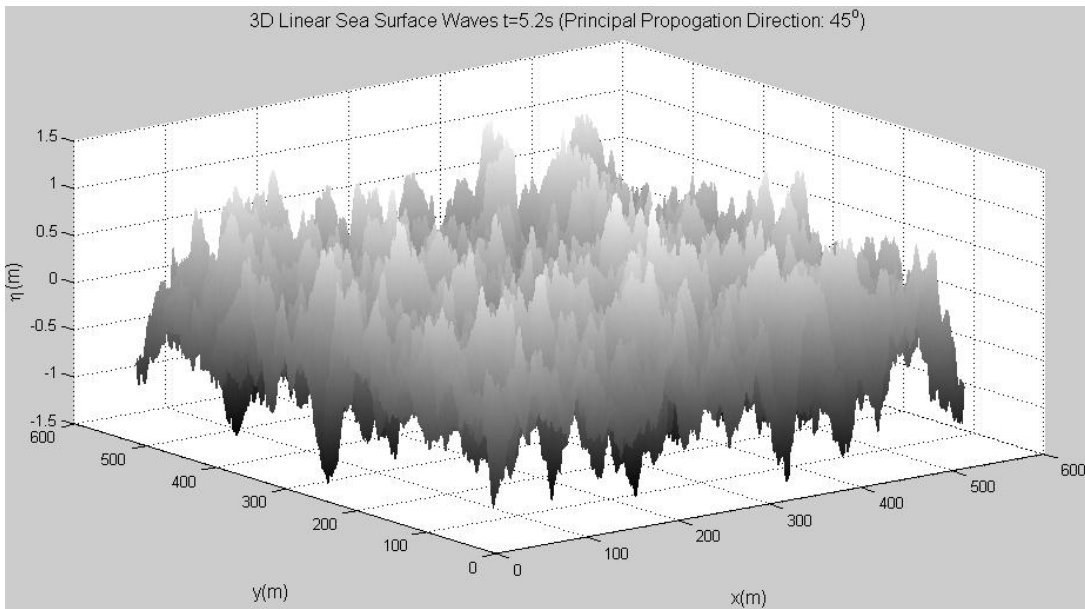


Figure 2.8: 3D Linear Sea Surface Waves Snapshot (Main Wind Direction: 45°)

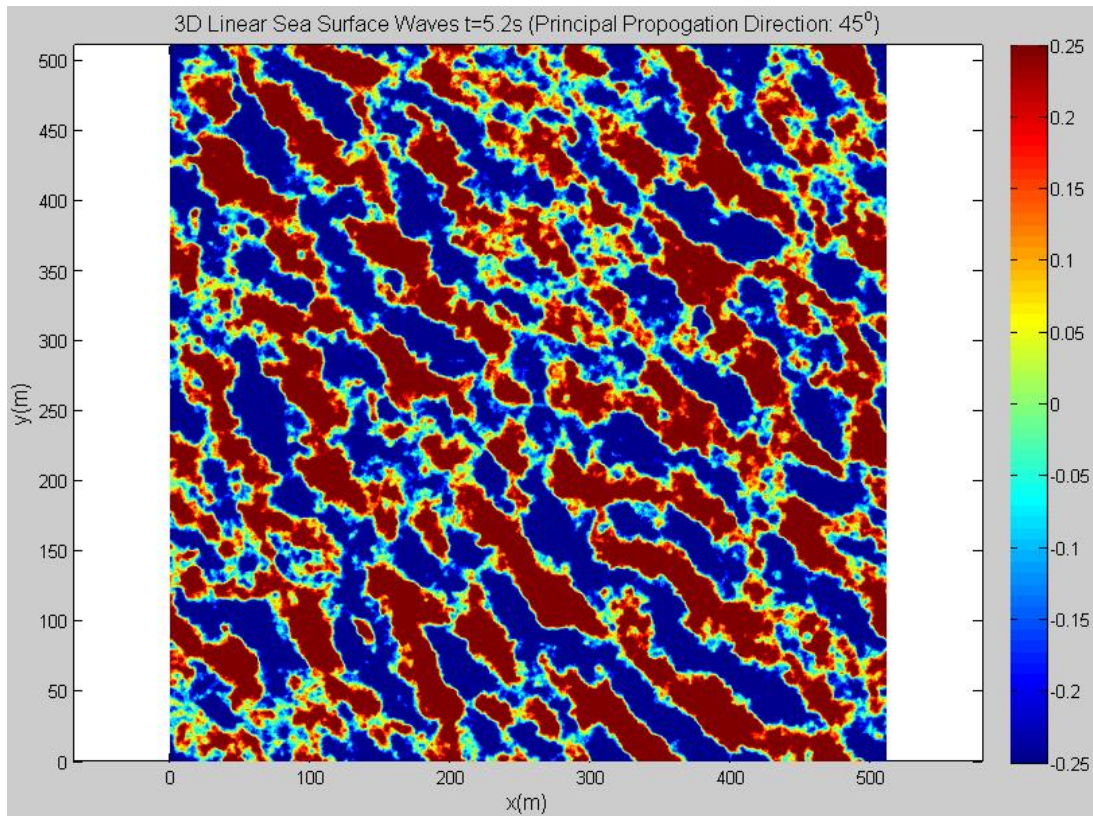


Figure 2.9: 3D Linear Sea Surface Waves Snapshot (Main Wind Direction: 45°)

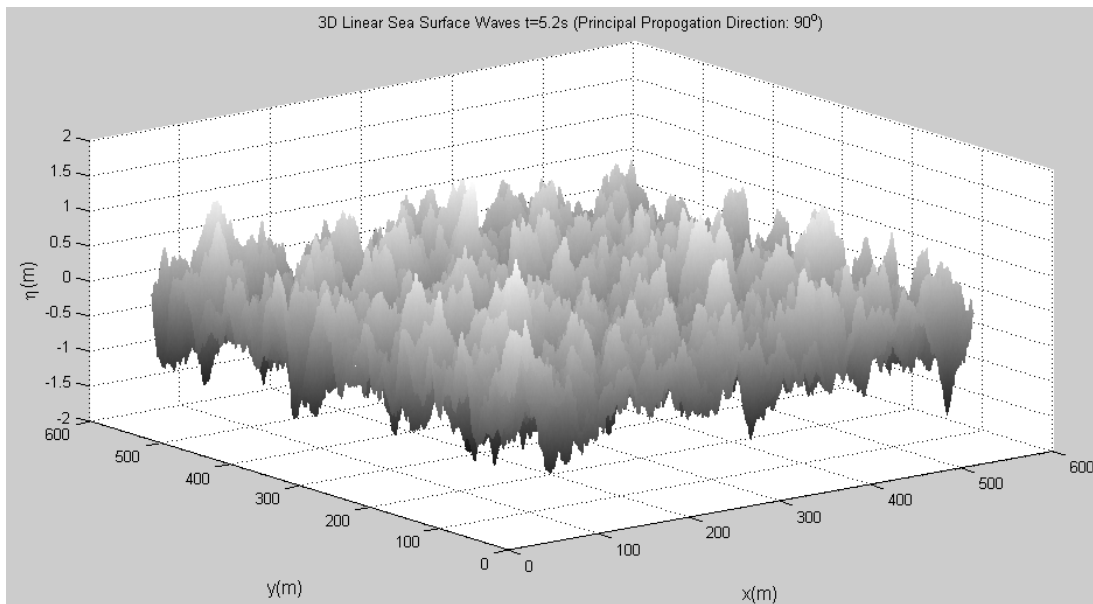


Figure 2.10: 3D Linear Sea Surface Waves Snapshot (Main Wind Direction: 45°)

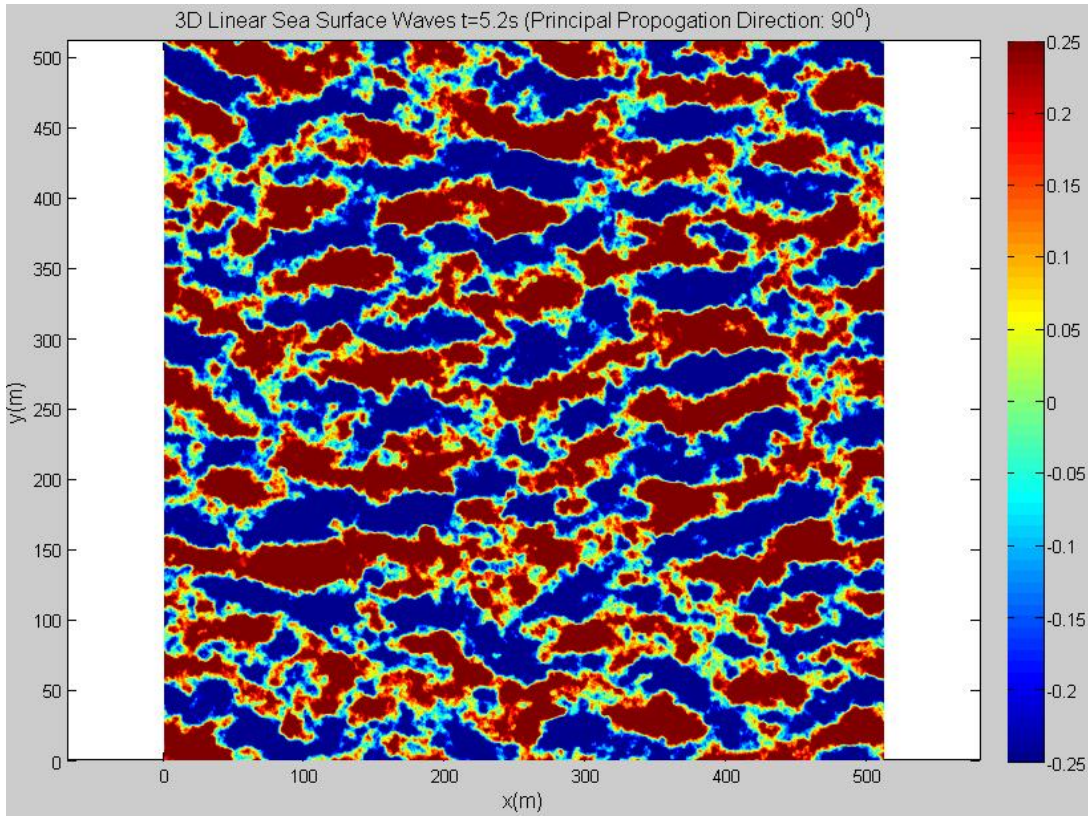


Figure 2.11: 3D Linear Sea Surface Waves Snapshot (Main Wind Direction: 90°)

Similar to 2D case, 3D linear sea surface wave model can also be checked by two methods. First method is again based on comparison between input and output directional wavenumber spectra as in 2D case. Input wavenumber spectrum ($S_{k_x k_y}(k_x, k_y)$) to use in comparison is specified in Equation (2.27). In order to obtain output wavenumber spectrum 2D Fast Fourier Transforms are made for sea surface wave field which is marched in time after construction of initial wave field. Second accuracy check is conducted by comparing input and output variances of sea surface fluctuation.

Figure 2.12 provides a comparison of input and output wavenumber spectrums. Again there is a perfect match between spectrums since linear evolution equations do not suffer from any numerical errors.

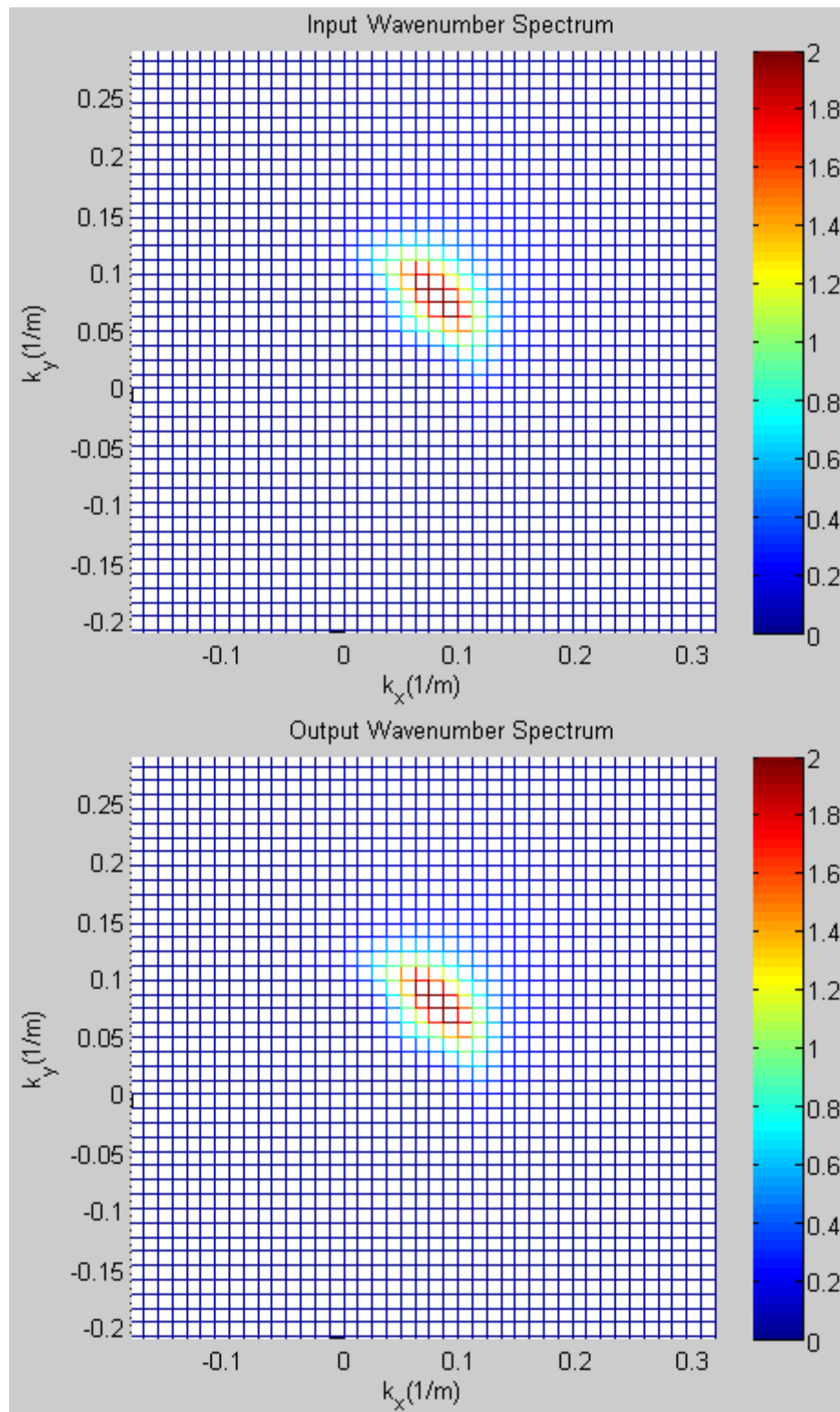


Figure 2.12: A Comparison of Input and Output Wavenumber Spectra (Main Wind Direction: 45°)

Since total energy of directional spectrum is same as energy of one dimensional spectrum, input variance is given by

$$\sigma^2_{input} = \int_{-\pi}^{\pi} \int_0^{\infty} S(\omega, \theta) d\omega d\theta = \int_0^{\infty} S(\omega) d\omega \quad (2.51)$$

Variances of time series of surface fluctuation (η) can be calculated at different points on the rectangular grid as output variances using the expression

$$\sigma^2_{output} = \frac{1}{T} \sum_{j=1}^T (\eta_j - \bar{\eta})^2 \quad (2.52)$$

where T denotes the length of time series of η and

$$\bar{\eta} = \frac{1}{T} \sum_{j=1}^T \eta_j \approx 0 \quad (2.53)$$

Input variance of wavenumber spectrum given in Figure 2.12 can be computed by using Equation (2.51). This computation results as $0.1526 m^2$. Output variances can also be calculated at four different rectangular grid points with different time lengths (T) by using Equation (2.52) and Equation (2.53). Time lengths of simulations (T) are $50T_p$, $100T_p$, $150T_p$, and $200T_p$ with respect to grid points. T_p denotes period of peak sea surface wave. Values of output variances at these grid points are $0.1504 m^2$, $0.1518 m^2$, $0.1521 m^2$, and $0.1523 m^2$ respectively. It can be obviously seen that the value of output variance converges to input variance by increasing time length of linear sea surface wave field simulation.

CHAPTER 3

ACOUSTIC SCATTERING FROM THE SEA SURFACE

3.1 Introduction

There are two different groups that acoustic propagation models are divided into, which are full wave models and ray-based models. Ray-based model is usually preferred when the processing speed is considered to be the most important factor. This model has some weaknesses such as shadow zones and caustics. This thesis uses BELLHOP, a Gaussian beam tracing model, as a substitute for the typical ray tracing models. Although BELLHOP ray tracer can be used describe the entire underwater acoustic channel, this thesis focuses on only the surface reflected ray paths. Acoustic Gaussian beam tracing and BELLHOP tool are described in detail in the following sections of this chapter.

3.2 Physical Basis for the Numerical Model

3.2.1 Theoretical Background

The wave equation is a partial differential equation that defines the motion of a wave in a medium. The acoustic wave equation is a linear approximation maintains only first-order terms of the wave equation. By computing the acoustic wave equation based on the proper boundary and medium conditions, the propagation of sound in an elastic medium such as sea water is described mathematically. The acoustic wave equation presents a relation between acoustic pressure, p , and spatial coordinates x , y , z as well as time t [30]. It can be expressed in the standard form of the wave equation stated as

$$\nabla^2 p - \frac{1}{c^2} \frac{\partial^2 p}{\partial t^2} = 0 \quad (3.1)$$

where ∇ is the spatial gradient operator, $\nabla = \frac{\partial}{\partial x} + \frac{\partial}{\partial y} + \frac{\partial}{\partial z}$, and c is the sound speed in the watercolumn that can vary with the spatial coordinates.

Modeling acoustic propagation conditions is significant when underwater acoustics is considered and various ways could be followed to generate different mathematical/numerical models. Ray theory, modal expansion and wave number integration techniques constitute the base for some of the most familiar approaches. Ray acoustics and ray tracing techniques are the most intuitive and often simplest ways for modeling sound propagation in the sea. Hence, an approach based on ray theory is used in this work due to its important advantages.

3.2.1.1 Wave Theory

Wave theory explains sound propagation with respect to characteristic functions called normal modes that are attained by solving Equation (3.1) [30]. These normal modes are added together to meet the required boundary and medium conditions. Even though complete solution for all frequencies is properly provided by this approach, it also has some drawbacks e.g., lack of provided intuitive picture of the distribution of radiated energy, difficulty in handling real boundary conditions, and need for significant computation power and time because wave theory approaches try to model the entire wave.

3.2.1.2 Ray Theory

Another method to follow in computing the wave equation is the ray theory. Ray theory of acoustics depends on the assumption that acoustic signal propagates along rays that are normal to the wavefronts, i.e., the surfaces of constant phase of the acoustic waves [43]. Propagation of ray paths is greatly influenced by the sound speed.

When generated from a point source in a medium with a constant sound speed, the wavefronts from surfaces that are concentric circles, and sound follows line paths that radiate out from the sound source. Rays and wavefronts in an isovelocity medium are illustrated in Figure 3.1. Rays appear to be straight lines due to the constant velocity of sound.

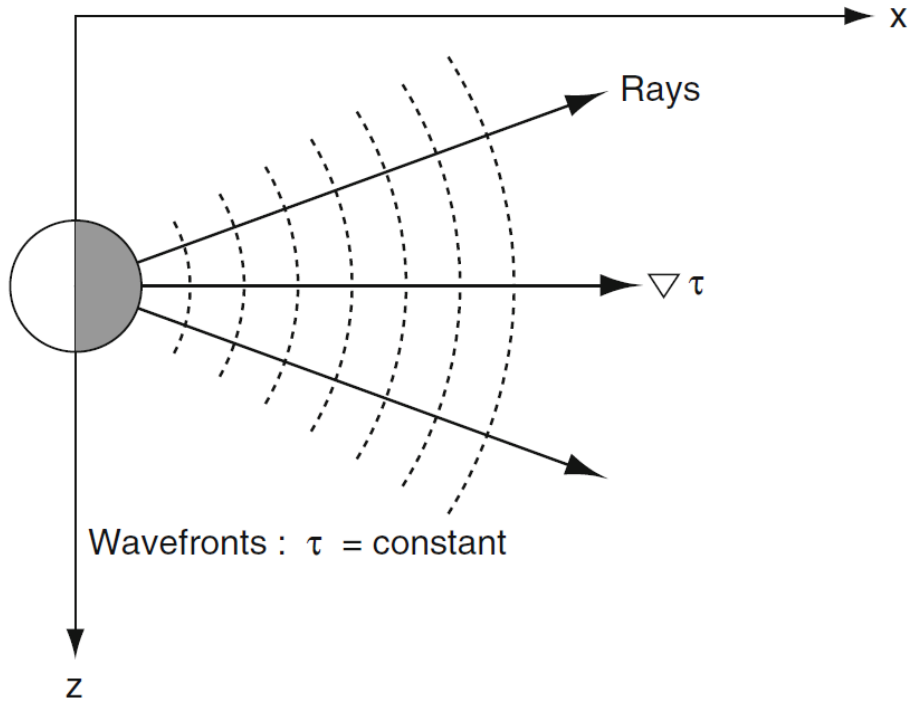


Figure 3.1: Rays and Wavefronts [29]

Since the speed of sound in underwater environment depends on temperature, depth and salinity of the water, spatial and temporal variability occur in the sound speed. It is fact that the water temperature and salinity changes with spatial coordinates of the sea. In addition, the hydrostatic pressure also changes with depth. The speed of sound in the watercolumn is approximated as an empirical formula given as [41]

$$c(T, S, z) = 1449.2 + 4.6T - 0.055T^2 + 0.00029T^3 + (1.34 - 0.017T)(S - 35) + 0.016z \quad (3.2)$$

where c stands for sound speed as a function of three independent variables which are temperature (T) in degree of centigrade, salinity (S) in parts per thousand, and depth (z) in meters.

The rays propagate in shape of curved paths instead of straight paths when the sound speed is not constant among watercolumn.

As stated in Snell's law, spatial variability of sound speed causes bending of rays towards the area where the speed is lower which is called as refraction [29]. The

Snell's law presents a simple formula in order to find the declination angle of ray at any depth z using only the declination angle (θ) at any other depth and knowledge of the sound speed profile of watercolumn. The result is

$$c(z_0) \cos \theta(z) = c(z) \cos \theta(z_0) \quad (3.3)$$

Figure 3.2 depicts Snell's law for an acoustic ray originating from the source with declination angle $\theta(z_0)$. Grazing angle of ray can be obtained by using Snell's law.

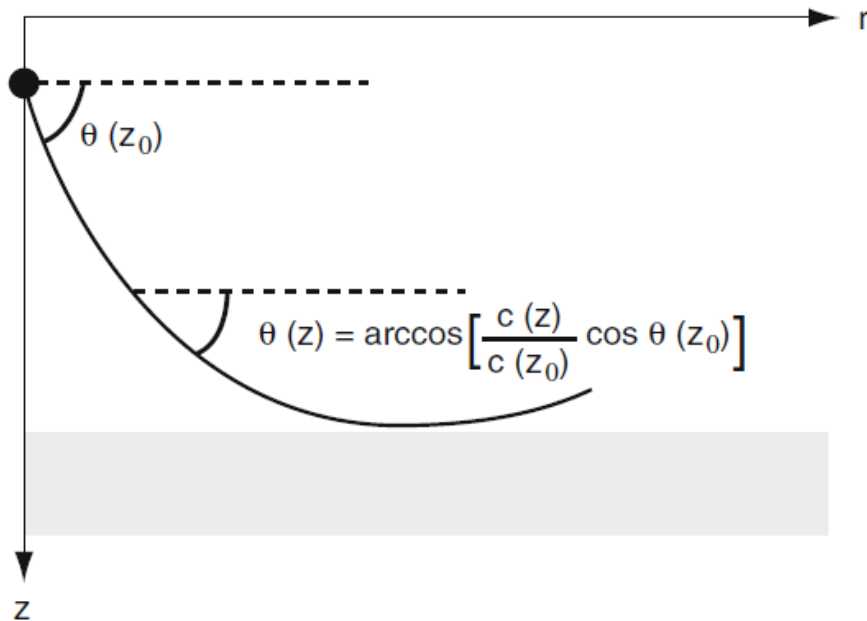


Figure 3.2: Snell's Law and Calculation of the Grazing Ray [29]

In order to depict the phenomenon that an acoustic wave bends or refracts along the ray path, the case of a medium with stack of fluid layer can be shown as an example. Snell's law is applied at each layer of fluid stack. Figure 3.3 depicts the refraction of incident ray trough a stack of fluid layers. Discrete stack of layers is given as an approximation of continuously changing sound speed $c(z)$.

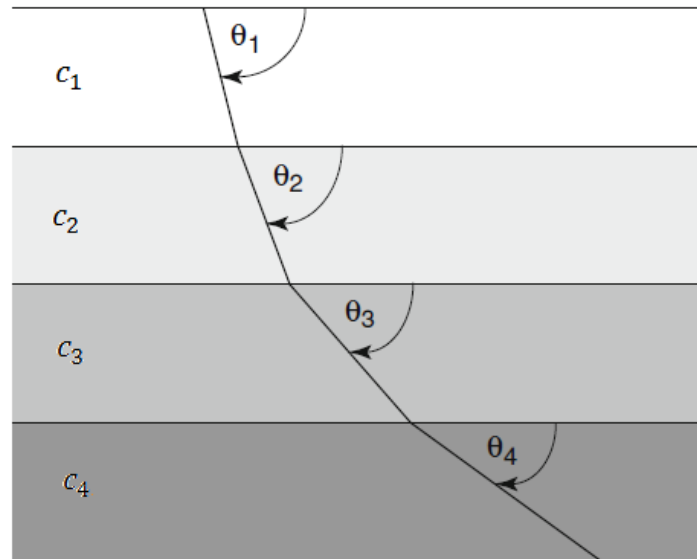


Figure 3.3: A Ray Refracting through a Stack of Layers [29]

Ray tracing is a computational technique used to calculate the trajectories of ray paths of acoustic signals which describe the spatial location of acoustical sound energy from the source basically [43].

Ray theory for tracing ray trajectories is derived from the wave equation based on some simplifying assumptions. Ray tracing method is essentially a high-frequency approximation. Ray models become more accurate at higher frequencies at which full wave models have often intolerably long computational time [15]. Therefore, ray tracing techniques are usually used in underwater acoustics for modeling the propagation of high-frequency sound signals as a function of time. In this study, source frequency of 1000 Hz is admitted high enough to have valid ray theory approximations.

Another important feature of ray models is that they are able to handle broadband problems efficiently [15]. In full wave models, a new model run is required for each new frequency. As an advantage, most of the computations for ray methods such as ray paths and travel times are frequency-independent. In addition to these advantages, ray theory is directly applicable to range-dependent (in a media that sound speed changes with range) problems.

3.2.2 Gaussian Beam Tracing and BELLHOP Model

Gaussian beam tracing is considered as a natural substitute for ray tracing. In this approach beams are associated with the individual acoustic rays in a ray fan. The field at any given point is constructed by adding up the contributions of each of the beams.

The Gaussian beam method is a lot more accurate than conventional ray tracing methods given that the beamwidth and curvature of beams are chosen properly. When compared to standard ray tracing, this method does not suffer from certain ray tracing artifacts such as perfect shadows and infinitely high energy caustics as an advantage.

Each ray is linked with a beam in the Gaussian beam method with a Gaussian intensity profile normal to the ray. The beamwidth and curvature are controlled by further pair of differential equations. These equations are combined with the usual ray equations to compute beam field in the neighborhood of the central ray of the beam [2].

In Porter and Bucker [2] many improvements are studied for the ray theory aiming to get more accurate results for acoustic propagation while keeping the model computationally efficient. Following the approach of [1] and [13], this thesis combines the output of sea surface wave model and the ray tracing method. The Gaussian beam approach that is used in coupled wave-acoustic model in this thesis is discussed mathematically in detail in the Section 3.2.2.1.

Basically, the initial process of Gaussian beam construction is integration of the typical ray equations to obtain central ray of the beam according to [2]. After that, a pair of auxiliary equations is integrated to form beams about the rays. These auxiliary equations govern the evolution of the beams in terms of the beamwidth and curvature as a function of arc length. Finally, a beam is obtained in which pressure field decreases in a Gaussian intensity of normal disturbance from central ray of the beam.

3.2.2.1 Mathematical Derivation of Gaussian Beams

Ray theory is based on acoustic wave equation mathematically. The mathematical derivation of ray theory provides the time delay of the acoustic ray from source to receiver, the ratio of the pressure amplitude at the desired location to that at a reference point, and the transmission loss [30]. Impulse response of the underwater channel and ray diagrams are obtained from these outputs of ray theory.

The ray theory is derived the acoustic wave equation given in Equation (3.1). By utilizing separation of variables it is shown that radiated sound pressure depends on the three-dimensional position vector $\mathbf{x} = (x, y, z)$ and time t

$$p = P(\mathbf{x})T(t) \quad (3.4)$$

so that only the spatial and time dependencies are separated. By substituting Equation (3.4) into Equation (3.1) and taking the separation constant as k^2 it is obtained

$$\nabla^2 P + k^2 P = 0 \quad (3.5)$$

$$\frac{d^2 T}{dt^2} + k^2 c^2 T = 0 \quad (3.6)$$

Equation (3.5) is the time independent version of acoustic wave equation which is called as the Helmholtz equation. If $k = \omega/c$, then

$$\nabla^2 p + \frac{\omega^2}{c^2(\mathbf{x})} p = 0 \quad (3.7)$$

where $c(\mathbf{x})$ is the three-dimensional sound speed and ω is the angular frequency of the source. A solution of the Helmholtz equation of the form given as

$$p(\mathbf{x}) = e^{i\omega\tau(\mathbf{x})} \sum_{j=0}^{\infty} \frac{A_j(\mathbf{x})}{(i\omega)^j} \quad (3.8)$$

where $\tau(\mathbf{x})$ is the travel time described by the acoustic signal to reach location \mathbf{x} from the source and $A(\mathbf{x})$ denotes the amplitude of the signal at \mathbf{x} . Equation (3.8) is called as the ray series. The first and second derivatives of the ray series, keeping only the first-order terms (due to high-frequency approximation) provides the infinite sequence of equations for the functions $\tau(\mathbf{x})$ and $A(\mathbf{x})$ given as

$$O(\omega^2): |\nabla\tau|^2 = \frac{1}{c^2(\mathbf{x})} \quad (3.9)$$

$$O(\omega): 2\nabla\tau \cdot \nabla A_0 + (\nabla^2\tau)A_0 = 0 \quad (3.10)$$

so that the solution to the Helmholtz equation is a product of a phase function, called the as eikonal equation ($O(\omega^2)$), and an amplitude function, called as the transport equation ($O(\omega)$).

In order to compute the eikonal equation, families of rays which are perpendicular to the wavefronts of $\tau(\mathbf{x})$ are introduced. These rays define a new coordinate system in ray coordinates in terms of the arc length, s . The ray trajectory ($\mathbf{x}(s)$) is later defined using the differential equation

$$\frac{d\mathbf{x}}{ds} = c\nabla\tau \quad (3.11)$$

which can be squared to attain the equation given by

$$\left| \frac{d\mathbf{x}}{ds} \right|^2 = c^2 |\nabla\tau|^2 \quad (3.12)$$

By substituting Equation (3.9) into Equation (3.12) implies that the tangent vector $d\mathbf{x}/ds$ has unit length. Then taking the Cartesian coordinates of Equation (3.11) and

differentiating with respect to the arc length s gives the resultant vector equation for the ray trajectories

$$\frac{d}{ds} \left(\frac{1}{c} \frac{d\mathbf{x}}{ds} \right) = -\frac{1}{c^2} \nabla c \quad (3.13)$$

The central ray of the beam in Porter and Bucker, [2], obeys the standard ray equations derived from Equation (3.13). When a cylindrical coordinate system is considered with r indicating horizontal range and z the depth coordinate the ray equations is obtained by Equation (3.13) stated as

$$\frac{d}{ds} \left(\frac{1}{c(r, z)} \frac{d\mathbf{r}}{ds} \right) = -\frac{1}{c^2(r, z)} \nabla c(r, z) \quad (3.14)$$

where $\mathbf{r} = \mathbf{r}(s)$ denotes the $[r(s), z(s)]$ coordinate of the ray as a function of arc length s , and $c(r, z)$ is the sound speed.

It is possible to reduce these equations given in Equation (3.14) to first-order form directly with the help of auxiliary variables $(\rho(s), \zeta(s))$. This is more convenient for numerical solution since numerical integrators for initial value problems are usually stated for first order systems [2]. In addition, since $[\rho(s), \zeta(s)]$ is proportional to local tangent vector, it becomes a useful quantity. Then, the ray equations are specified in first-order form stated as

$$\frac{dr}{ds} = c\rho(s) \quad (3.15)$$

$$\frac{d\rho}{ds} = -\frac{1}{c^2} \frac{\partial c}{\partial r} \quad (3.16)$$

$$\frac{dz}{ds} = c\zeta(s) \quad (3.17)$$

$$\frac{d\zeta}{ds} = -\frac{1}{c^2} \frac{\partial c}{\partial z} \quad (3.18)$$

Ray tracing is generally comprised of a set of differential equations describing the trajectory of ray called the ray equations (Equation (3.15)-Equation (3.18)). These equations are governed by given initial conditions to be able to trace the path of a ray which propagates away from the source. Figure 3.4 indicates the source position (r_0, z_0) where the ray starts with a specified take-off angle θ_0 as the initial conditions of ray. And t_{ray} represents tangent vector $(c[\rho(s), \zeta(s)])$ to the traveling ray [29]. The amplitude of a ray is directly related with change in the cross-sectional area of the ray tube bounded by neighboring rays.

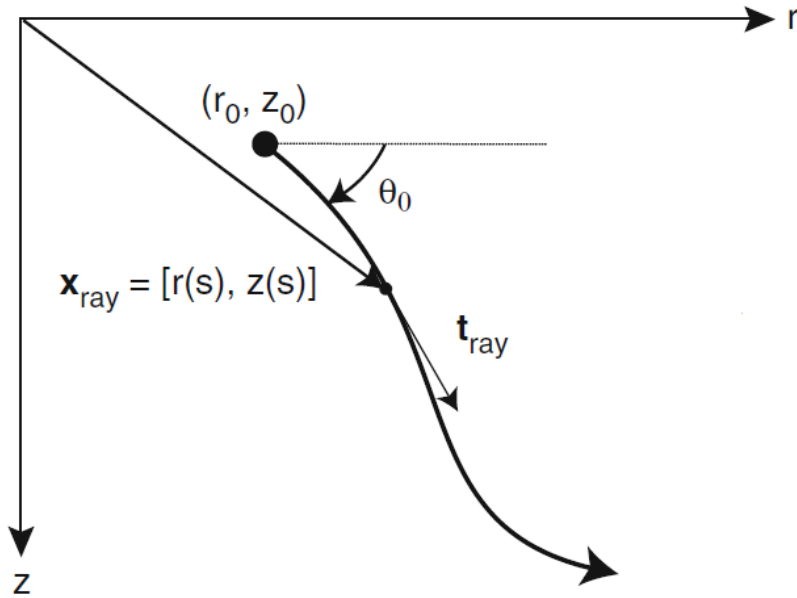


Figure 3.4: Schematic of the 2D Ray Geometry [29]

In order to derive the curvature of beam and beamwidth, the quantities $p(s)$ and $q(s)$ which are obtained by integrating an additional pair of ordinary differential equations along the central ray are used. Derivation of these additional equations is done by computing parabolic equation in the neighborhood of each central ray. In [2] the final result of the derivation is stated as follows

$$\frac{dq}{ds} = c(s)\rho(s) \quad (3.19)$$

$$\frac{dp}{ds} = -\frac{c_{nn}}{c^2(s)}q(s) \quad (3.20)$$

where, c_{nn} denotes the second normal derivative of sound speed $c(r, z)$ and it is computed as

$$\begin{aligned} c_{nn} &= c_{rr} \left(\frac{dr}{dn} \right)^2 + 2c_{rz} \left(\frac{dr}{dn} \right) \left(\frac{dz}{dn} \right) + c_{zz} \left(\frac{dz}{dn} \right)^2 \\ &= c_{rr} (N_{(r)})^2 + 2c_{rz} (N_{(r)})(N_{(z)}) + c_{zz} (N_{(z)})^2 \end{aligned} \quad (3.21)$$

where $(N_{(r)}, N_{(z)})$ stands for a unit normal stated as

$$(N_{(r)}, N_{(z)}) = \left(\frac{dz}{ds}, -\frac{dr}{ds} \right) = c(s)[\zeta(s), -\rho(s)] \quad (3.22)$$

Next, the beam is defined by

$$u(s, n) = A\sqrt{c(s)/[rq(s)]} \times \exp(-i\omega\{\tau(s) + 0.5[p(s)/q(s)]n^2\}) \quad (3.23)$$

where A is an arbitrary constant, n denotes the normal distance from the central ray, and ω stands for the angular frequency of the source signal.

The term $\tau(s)$ in Equation (3.23) denotes the phase delay (travel time) of ray which satisfies the equation given by

$$\frac{d\tau}{ds} = \frac{1}{c(s)} \quad (3.24)$$

For Equation (3.23) to describe the beam field completely, the intended branch of the square root is needed to be specified [2]. The branch is chosen so that the resulting phase varies continuously with the arc length s . Thus the square root defined by

$$\sqrt{x} = (-1)^{m(s)} \text{sqrt}(x) \quad (3.25)$$

where $\text{sqrt}(x)$ now denotes the principal value, i.e., the branch of the square root that yields a resulting phase in $(-\pi/2, \pi/2)$. The function $m(s)$ is the integer number which gives the number of times $c(s)/[rq(s)]$ (or equivalently $q(s)$) has crossed the negative imaginary axis. The function $m(s)$ is computed during the integration of the $p - q$ equations.

The initial conditions for the ray equations which include four ordinary differential equations governs the central ray of the beam are

$$[r(0), z(0)] = (r_s, z_s) \quad (3.26)$$

$$[\rho(0), \zeta(0)] = (\cos \alpha, \sin \alpha)/c(0) \quad (3.27)$$

where (r_s, z_s) denotes the source location and α stands for prescribed takeoff angle. Angles are measured with respect to the horizontal r axis and positive angles are used for downgoing rays so that α is a declination angle.

It is convenient to relate $p - q$ functions to beam radius (half-width), $L(s)$, and beam curvature $K(s)$ in order to discuss initial conditions of $p - q$ functions. Beam radius and curvature functions are defined by

$$L(s) = \sqrt{-2/\{\omega \text{Im}[p(s)/q(s)]\}} \quad (3.28)$$

$$K(s) = -c(s) \text{Re}[p(s)/q(s)] \quad (3.29)$$

As a plain definition the beam radius $L(s)$ is the normal distance from the central ray at which the beam amplitude $1/e$ of its maximum value. In addition, the rate of change of phase which is based on traveling normal to the central ray relates directly to local curvature. Therefore, it provides the basis to interpret $K(s)$ as curvature.

Although there is no consensus on the proper choice of $p(0)$ and $q(0)$ (0) and $K(0)$ equivalently) in the literature, Porter and Bucker, [2], obtained useful results by assuming that beam is initially flat (no curvature) and choosing the initial beamwidth so that the beams are “space filling” in the far field. $q(0)$ is set to an imaginary constant of magnitude ϵ given by Equation (3.30) in order to obtain a flat beam

$$p(0) = 1, \quad q(0) = i\epsilon \quad (3.30)$$

Note that $p(0)$ can be chosen as 1 without loss of generality, since p occurs in Equation (3.23) only as the quotient p/q . Then, it can be seen that purely real ϵ is equivalent to zero curvature beams referring to Equation (3.29).

Next ϵ is selected to obtain “space filling” beam in the farfield. In a 51irby51nous medium with constant sound speed c_0 , the $p - q$ equations are yielded solutions given by

$$p(s) = 1, \quad q(s) = c_0s + i\epsilon \quad (3.31)$$

or

$$p(s)/q(s) = (c_0s - i\epsilon)/(c_0^2s^2 + \epsilon^2) \quad (3.32)$$

Therefore, the Gaussian beam defined by Equation (3.23) diminishes in intensity with n (the normal distance from the central ray) according to

$$\exp[-0.5\omega\epsilon n^2/(c_0^2s^2 + \epsilon^2)] \quad (3.33)$$

Then, if a beam fan including N beams which are traced over angular spread (α_1, α_2) , each beam “occupies” an angle of $\delta\alpha = (\alpha_2 - \alpha_1)/(N - 1)$ and the normal distance to the central ray of the adjacent beam is specified as $n = s\delta\alpha$. In order to cover a reasonable are even at long ranges ($c_0s > \epsilon$), ϵ can be chosen such that the intensity of the beam is reduced by $1/e$ at the location of two adjacent beams. Therefore,

$$\epsilon = 2c_0^2 / [\omega(\delta\alpha)^2] \quad (3.34)$$

Equation (3.34) together with Equation (3.30) completes the specification of $p - q$ initial conditions.

When a point source in a cylindrical symmetric ocean is specialized, a “ray tube” formed by the boundary of two rays launched with adjacent take-off angles, separated by $\delta\alpha$, is depicted as in Figure 3.5 [29].

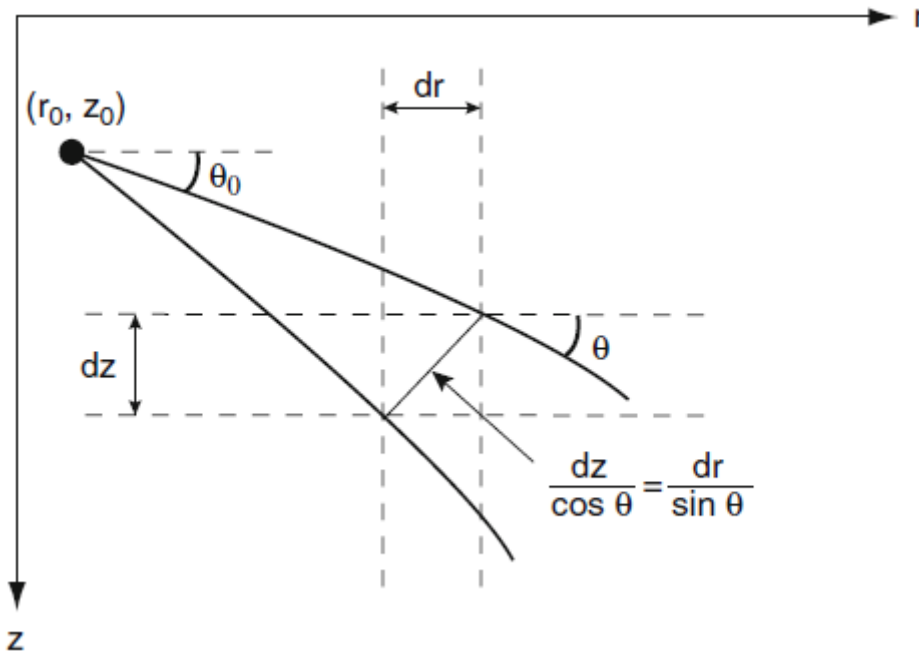


Figure 3.5: The Ray-Tube Cross Section [29]

In many cases, the sources are not “beamlike” and an approximation to the source as superposition of beams is needed. An approach of this approximation is matching the high-frequency asymptotic field of Gaussian beam representation to exact solution in a homogenous medium. An expansion of the Gaussian beam field as an integral over beam take-off angle stated as

$$u(\alpha_0) = \int A(\alpha) \sqrt{\frac{c(s)}{rq(s)}} \times \exp\left\{-i\omega \left[\tau + 0.5 \left(\frac{p}{q}\right) n^2\right]\right\} d\alpha \quad (3.35)$$

where α_0 denotes the angle to the receiver. In homogenous medium, Equations for $p(s)$, $q(s)$, and $\tau(s)$ can be obtained easily in a homogenous watercolumn. The saddle point method in [2] provides the high-frequency asymptotic approximation given by

$$u(\alpha_0) \sim A(\alpha_0) c_0 \sqrt{2\pi/[q(0)\omega r R]} \times \exp(-i\omega R/c_0 - i\pi/4) \quad (3.36)$$

where R denotes the slant range to receiver and r stands for the (r, z) cylindrical coordinate of the receiver. The initial condition of q quantity ($q(0)$) denotes is given by Equation (3.31).

After converting entire expression to (R, z) coordinates by using $r = R \cos \alpha_0$ relationship, the exact solution for a point source in three dimensions given in Equation (3.37) can be matched.

$$u(R) = \exp(-i\omega R/c_0)/R \quad (3.37)$$

The exact solution and high-frequency asymptotic approximation forms match if

$$A(\alpha) = (1/c_0) \exp(i\pi/4) \sqrt{q(0)\omega \cos \alpha / (2\pi)} \quad (3.38)$$

and finally the Gaussian beam field is constructed as

$$\begin{aligned} u(\alpha_0) &= u(s, n) \\ &= \sum \delta\alpha \left(\frac{1}{c_0}\right) \exp\left(\frac{i\pi}{4}\right) \sqrt{\frac{q(0)\omega \cos \alpha}{2\pi}} \\ &\quad \times \frac{c(s)}{r q(s)} \exp\left\{-i\omega \left[\tau(s) + 0.5 \left(\frac{p(s)}{q(s)}\right) n^2\right]\right\} \end{aligned} \quad (3.39)$$

where the integral is approximated by a discrete summation.

For a detailed discussion of Gaussian beam method, it can be referred to Porter and Bucker, [2].

3.3 BELLHOP Ray Tracing Model

BELLHOP is a ray-based model for predicting acoustic pressure fields in ocean environments by using Gaussian beam tracing [40]. The beam tracing structure of BELLHOP tool leads to an algorithm which has a particular simplicity. Several types of beams are implemented in BELLHOP including Gaussian and hat-shaped beams. Both geometric and physics-based spreading laws can be chosen for ray tracing. BELLHOP can produce several useful outputs including transmission loss by acoustic propagation, eigenrays, arrivals, and received timeseries. BELLHOP also allows for range-dependence in the top and bottom boundaries (altimetry and bathymetry) of watercolumn. Sound speed profile can be range-dependent as well. By using additional input files, directional sources and geoacoustic properties for the bounding media can be specified. Top and bottom boundary reflection coefficients can also be provided as an input to the BELLHOP ray tracer.

BELLHOP is utilized as a tool which uses the Gaussian beam tracing method in this thesis. BELLHOP numerically integrates the ray equations to trace rays of source signal inside the underwater channel. BELLHOP program is tested with full wave acoustic models which are computationally intensive. Results of BELLHOP ray tracer shows excellent agreement with full wave methods as stated in [2]. The Gaussian beam tracing method used in BELLHOP method does not suffer from numerical artifacts which are present in conventional ray-based approaches, although it has the same computational efficiency with other ray-based methods.

In Figure 3.6 provides a comparison between standard ray tracing and Gaussian beam tracing method accuracies. Transmission loss is calculated utilizing both ray tracing methods with a deep source. Sound speed profile specified in simulations is n^2 -linear in which square index of refraction varies linearly with depth, i.e., $n^2 = (c_0/c)^2 = a + bz$. F , SD , and RD represents source frequency, source depth, and receiver depth respectively [29]. Solid curve shows the exact solution using exact spectral integral representation. Dashed curve in Figure 3.6 (a) which is obtained by standard ray tracing approach shows shadow zones and caustic. On the other hand, dashed curve in Figure 3.6 (b) which is obtained by Gaussian beam tracing does not show the caustic spike occurred with standard ray tracing and fall off into shadow

zone is more gradual. There is a close agreement between Gaussian beam tracing solution and the exact solution.

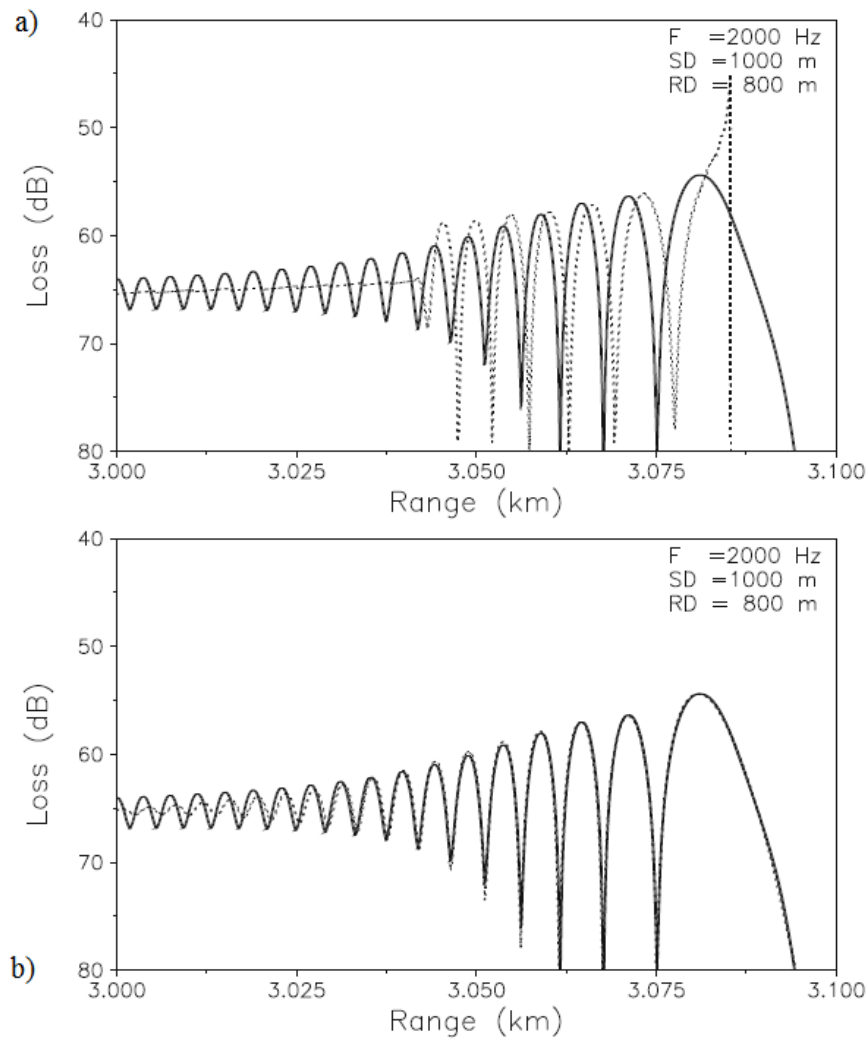


Figure 3.6: Transmission Loss (a) Standard Ray Tracing versus Exact Solution, (b) Gaussian Beam Tracing Solution vs. Exact Solution, Solid Curve: Exact Solution [29]

3.3.1 BELLHOP Input Files

In order to run BELLHOP program, various files must be provided. These files are used to describe the computational environment and the geometry of sources and receivers. There is only one such file which is referred to as an environmental file in the simplest and the most typical case [40]. This input file includes environmental parameters such as water depth, source and receiver locations, sound speed profile (SSP), and top and bottom boundary conditions. Moreover, if sea bottom has a

range-dependent shape, then a bathymetry file is added to define depth of watercolumn by using range-depth pairs. In a similar manner, if the sound speed profile in watercolumn is range-dependent, then SSP file is added to specify the sound speed by using tabulated values on a regular grid. In addition to these, an arbitrary bottom reflection coefficient is also be specified in order to characterize the bottom by using angle-reflection coefficient pairs. In order to implement similar capabilities for the surface of watercolumn the option of providing a top reflection coefficient and a top shape (called as altimetry file) can be used as well. In this study, sea surface is defined as a piecewise linear boundary. An altimetry file is needed for importing shape of the sea surface into BELLHOP program. Angle of incident ray (t_{ray}^I) is equal to angle of reflection ray (t_{ray}^R) in the piecewise linear approach to the sea surface. In Figure 3.7 reflection from piecewise linear boundary is depicted. Tangent and normal to boundary are also denoted as t_{bdry} and n_{bdry} . Interface between sea water and air is accepted as quasi-perfect reflector, because of high impedance contrast between the two environments. This means only phase of the acoustic ray shifts π radians after reflection and there is no change in absolute amplitude.

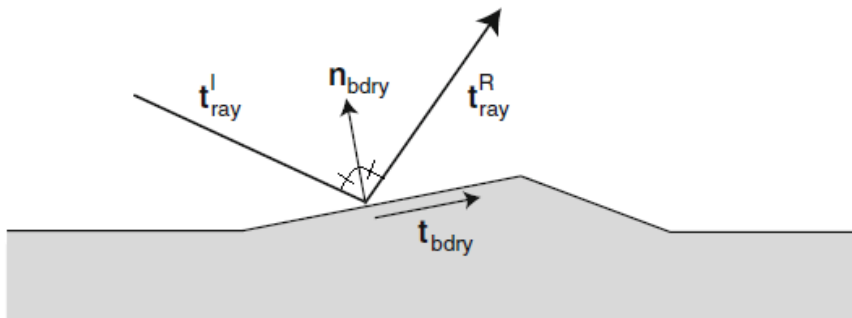


Figure 3.7: Ray Reflected from a Piecewise Linear Boundary [29]

It is usually assumed that the acoustic source is omni-directional. However, if beampattern of the source is known, it is possible to define this known beampattern by using a file with angle-amplitude pairs. These files are read into BELLHOP according to options selected within the main environmental file.

Properties of beams such as number of beams to be used, their launching angles and type of beams also should be specified in the environmental file (input file) as well.

In an underwater acoustic channel, the energy of the transmitted signal is partly transferred to heat energy. Loss of acoustic energy defined as attenuation. Attenuation is caused basically by two mechanisms which are spreading loss and absorption loss [41]. There are two types spreading loss. First one is spherical loss which causes attenuation of the signal which is proportional to inverse of square of the distance from the source point. Cylindrical loss is other type of spreading loss mechanism which causes attenuation of the signal which is proportional to inverse of the distance from the source point. Attenuation is strongly frequency dependent in underwater acoustic channel. If frequency increases, attenuation increases due to absorption loss. In this thesis, BELLHOP program uses the Thorp attenuation formula which describes coefficient of absorption loss ($\alpha(f)$). A simplified expression of frequency dependence of the attenuation given by [41]

$$\alpha(f) = 0.11 \frac{f^2}{1 + f^2} + 44 \frac{f^2}{4100 + f^2} + 2.75(10^{-4} f^2) + 0.003 \quad (3.40)$$

The absorption coefficient is in dB/km and f is in kHz in this expression.

Energy can be lost due to scatterings from the sea surface and sea bottom as well. In this thesis bottom reflections of sound energy are prevented by using options chosen in the environmental file. Sea surface is taken as a perfectly reflecting “pressure release” boundary in this study. Pressure release boundary means pressure is zero ($p = 0$) at the sea surface. Incident wave directed to the sea surface does not subject to energy loss after reflection. Only phase of incident wave shifts π radians as stated former.

3.3.2 BELLHOP Output Files

BELLHOP can produce several different output files according to options selected within the main input file. For example, if ray tracing option is chosen, BELLHOP program produces a file containing path coordinates of a fan of rays emanating from the source. If the eigenray option is selected, then the beam fan is winnowed to

include only the rays which reach to the receiver location. Eigenrays are the rays that are generated at the source and reach the receiver as a definition. The file format for eigenray option is identical to that used in the standard ray-tracing option. General purpose of usage of ray is getting a sense of how energy is propagating in the underwater channel. Figure 3.8 depicts eigenrays reach to the receiver which are emanating from source location depending on Munk sound speed profile. Different colors in Figure 3.8 represent different bounce paths of eigenrays, for example, red color represents direct path.

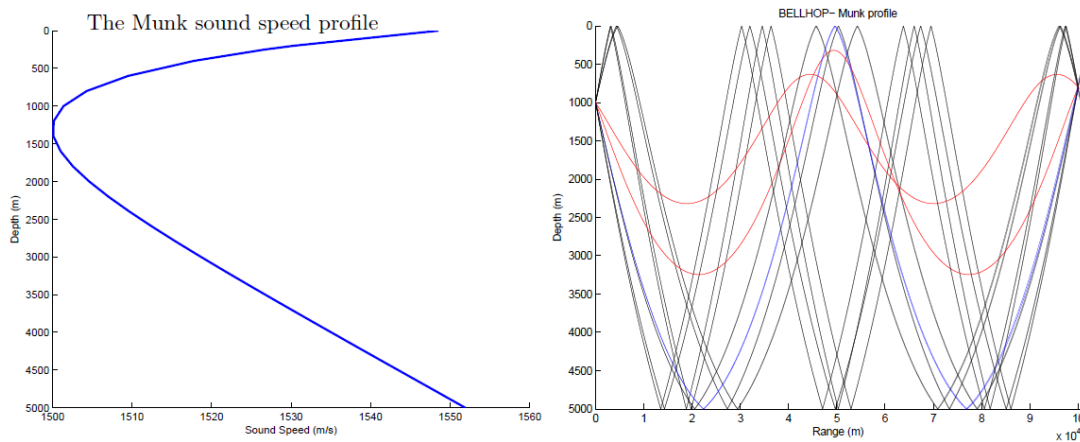


Figure 3.8: Eigenrays for the Munk Sound Speed Profile with the Source at 1000 m and the Receiver at 800 m [40]

The complex pressure field at the receiver point is obtained by contributions of each eigenray based on its intensity and phase [29]. In order to calculate the intensity at the receiver point the contribution of the each eigenray is simply summing up such that

$$p^c(r, z) = \sum_{j=1}^{N(r, z)} p_j(r, z) \quad (3.41)$$

where $N(r, z)$ denotes the number of eigenrays contributing to the complex field at a particular receiver position and $p_j(r, z)$ stands for pressure due to that eigenray. In

this thesis, only surface-interacted eigenrays are considered. Direct paths and bottom- interacted paths which reach to the receiver are out of scope of this thesis.

According to BELLHOP Manual [40] there are several points of attention for true eigenray calculation. First of all, default beam type which has a beamwidth defined by ray tube formed by adjacent rays should be used. It is called as geometric beam in [40]. Other types of beam cause get lots of additional rays that pass at greater distances from the receiver, since they have much broader beams than beams of the geometric ray. Secondly, a finer beam fan is needed to reach to the receiver point in a narrower range. Finally, eigenray calculation should be done with a single source and a receiver. All these points of attention are applied for ray files as well as arrival files in this thesis.

Another output option which is not used in this study is selected for calculating the transmission loss for a tonal source (or for a single tone of interest in a broadband waveform). The transmission loss is defined as the sound intensity due to a source of unit strength essentially. Distribution of acoustic sound energy depends on Munk sound speed profile in a flat waveguide where source depth is $1000m$ is presented in Figure 3.9. Transmission loss is calculated from acoustic sound pressure field ($p(s)$) and defined as [29]

$$TL(r, z) = TL(s) = -20 \log \left| \frac{p(s)}{p^0(s = 1)} \right| \quad (3.42)$$

where $p^0(s = 1)$ is pressure for point source in free space to be evaluated at a distance $1m$ from the source given by

$$p^0(s = 1) = \frac{1}{4\pi} \quad (3.43)$$

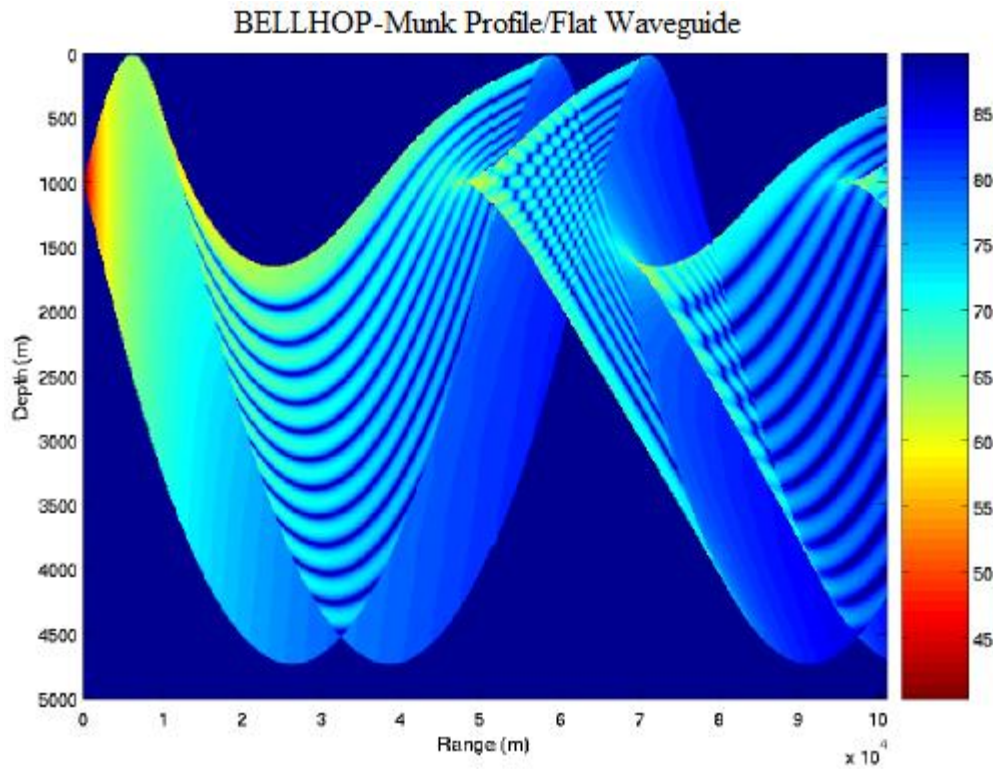


Figure 3.9: Coherent Transmission Loss Calculated by BELLHOP [44]

If not only the intensity due to a tonal source but also the entire timeseries is needed, then the arrivals calculation option is selected. This option produces a file which contains the number of echoes or arrivals for each source depth, receiver depth, and receiver range. Amplitude-delay pairs are contained in the resulting arrivals file in order to define amplitude and time delay of each arrival in the watercolumn. In addition to information about the amplitude, phase, and travel time (delay) for each arrival, the ray take-off angle at the source and arrival angle at the receiver, and the number of top and bottom bounces are also provided. The arrivals information gives the impulse response of the underwater acoustic channel. Subplots (a), (b), and (c) of Figure 3.10 shows an example channel impulse response as a function of range, depth, and time respectively. Channel impulse response can be passed to a convolver which sums up the echoes of a particular source timeseries in order to compute a received timeseries.

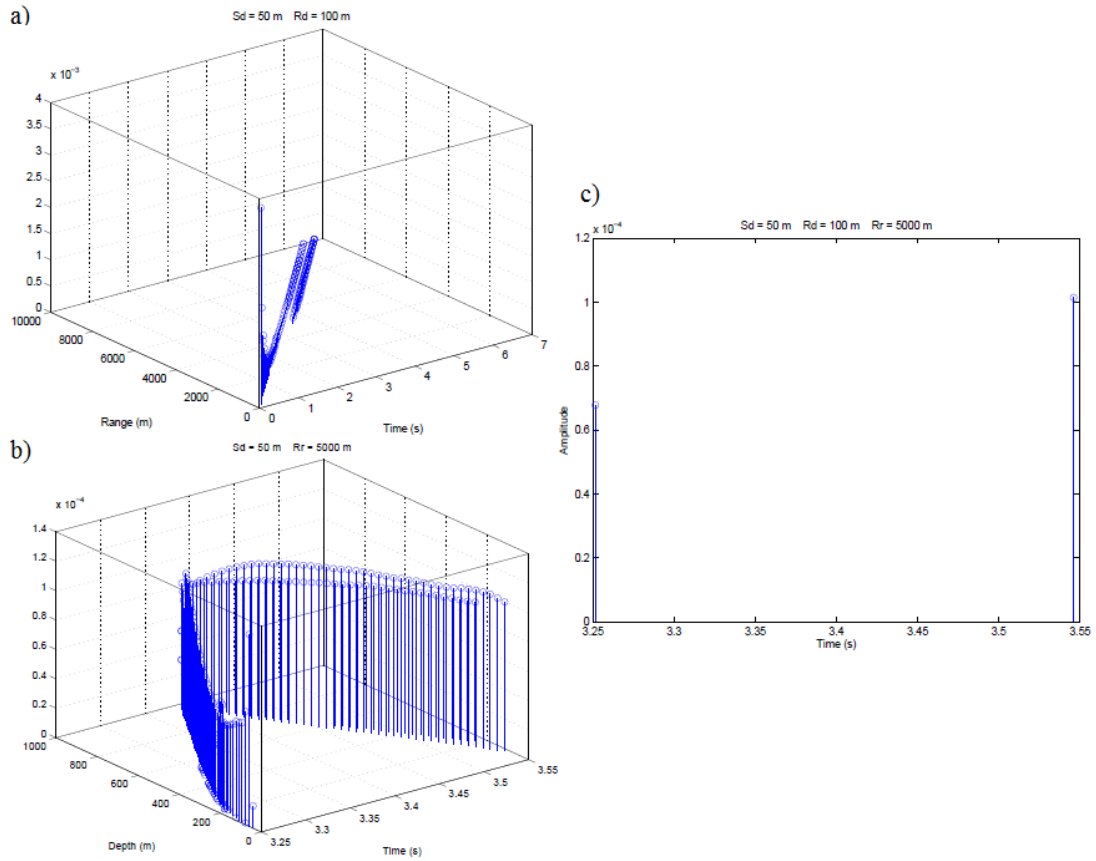


Figure 3.10: An Example Channel Impulse Response, reproduced from [40]

Following Bayındır [1], all calculations in this thesis are based on eigenray files generated by BELLHOP which are reflected from surface only and do not experience any other interaction with sea bottom or sea surface boundaries. More than once sea surface boundary interactions are allowed. An arrivals output file which contains information about arrival time, arrival angle, launching angle, and pressure amplitude at the arrival is also needed to make calculations. These outputs are combined with sea surface wave model to get the fluctuation results of the arrivals. Therefore, at each time-step of iterations of the time-evolving sea surface wave model BELLHOP program is run two times. In the first run, the arrival file option is selected in order to get arrival times of rays (delays and amplitudes). In the second run, the eigenray option is selected in order to compute geometry of eigenrays and to find interaction points with top and bottom of the watercolumn.

3.4 Doppler Shift Calculations

It is well known that when a sound wave is scattered from a moving object the frequency of the sound wave changes. This phenomenon is called Doppler shift. Doppler shifts experienced by acoustic eigenrays interacted with the moving sea surface are calculated in this thesis in order to use in coupled model in Chapter 5. It is needed to know the geometry of the eigenrays at each time step of time-varying sea surface wave model [1] for this purpose.

Doppler Effect is observed as a shift in the frequency of scattered object due to motion of source, receiver or scattering point. Sign of the Doppler shift (positive or negative) in the frequency of the source signal depends on the eigenray geometry and direction of the motion of the scattered object.

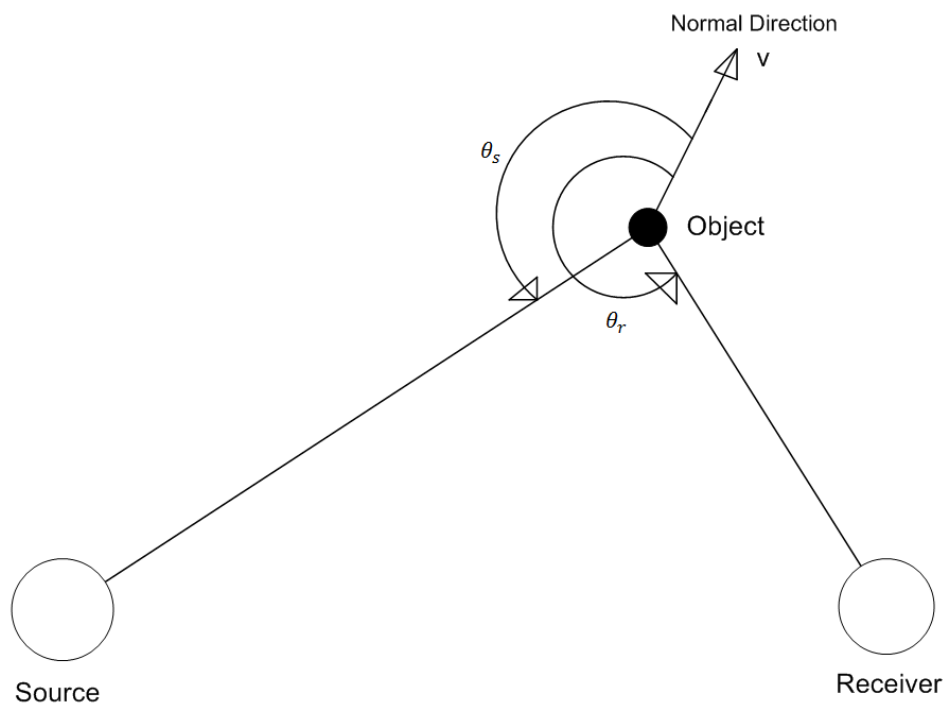


Figure 3.11: Doppler Effect of Moving Object. Source and Receiver in x-z Plane [8]

Source signals interacted with moving sea surface are shifted in frequency. Based on the eigenray geometry given in Figure 3.11, Doppler shift is calculated by expression stated as [8]

$$f_r = \frac{f_s(c + v \cos \theta_s)}{(c - v \cos \theta_r)} \quad (3.44)$$

where f is the radiating frequency of acoustic source signal, f_r is the frequency observed at the receiver and c is the sound speed in the watercolumn. v denotes the surface-normal velocity which is discussed in Section 2.6.

In the time-varying sea surface scattering problem, the top boundary of the underwater channel serves as the moving scatterer object at the interaction points of eigenrays with the sea surface. After generation of rays by BELLHOP program, these interaction points are specified and then Doppler shifts are calculated at these points by using the surface-normal velocity obtained by sea surface wave model.

When an eigenray hits the sea surface more than once, Doppler shift calculations are applied successively at each interaction point [1]. An example of multiple interactions of eigenrays with the sea surface is given in Figure 3.12. Pink triangles in Figure 3.12 show interaction points with the sea surface.

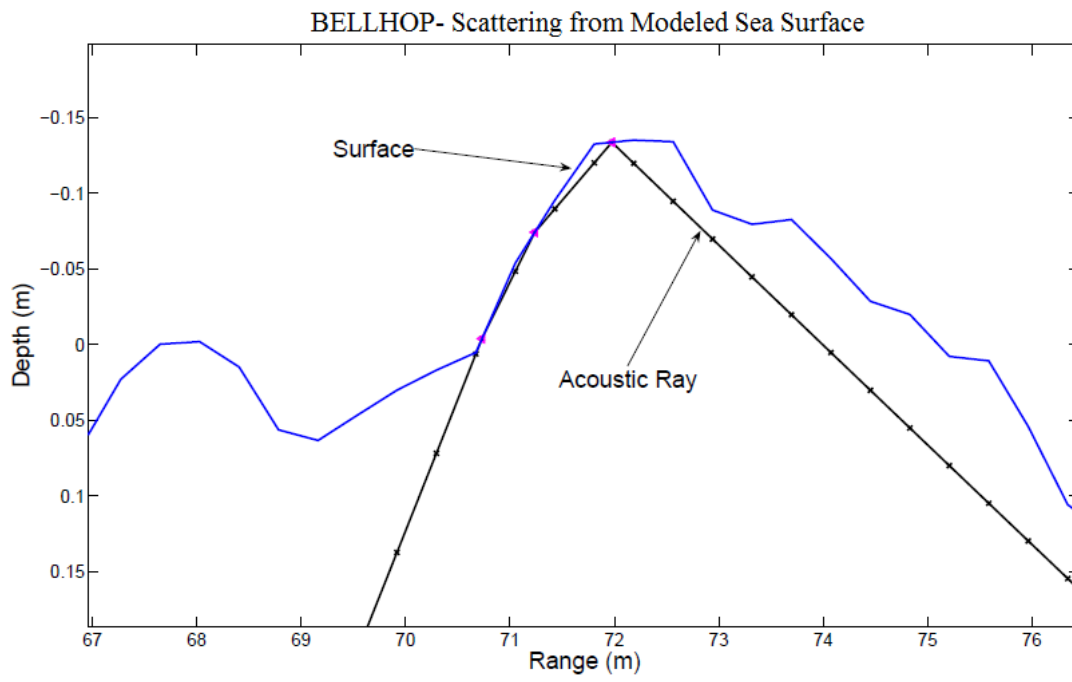


Figure 3.12: Multiple Interactions of Acoustic Eigenrays from the Sea Surface [1]

CHAPTER 4

VirTEX ALGORITHM

4.1 Introduction

In order to model the effects of the watercolumn with a rough sea surface boundary on the transmission of known timeseries the BELLHOP program is used which is based on Gaussian beam tracing method in this thesis. BELLHOP computes the impulse response or time arrival structure of the underwater acoustic channel for a given source and receiver location [14]. The received timeseries at a hypothetical receiver point can be calculated by convolving source timeseries with the impulse response of the underwater acoustic channel.

Since BELLHOP ray tracer is designed for environments where the source, receiver, and boundaries of watercolumn are stationary, utility of convolution approach is limited. In practice, most of the environments involve some form of motion; the time-evolving sea surface and motion of source and/or receiver common examples to that motion. Therefore, there is a need to develop statistical channel models which are computationally efficient for numerical simulation in order to take into account the motion induced effects on underwater acoustic signals. The Virtual Timeseries Experiment (VirTEX) code is an example model which has been developed to simulate the effect of channel variation in a manner that is computationally more efficient than repeated application of the BELLHOP program. VirTEX algorithm operates by tracing multiple interrelated beams in order to determine the cumulative effect on the signal of a given frequency [32].

VirTEX algorithm can model most forms of environmental motion as a primary advantage. In order to approximate to the time-varying environment of interest a temporal sequence of static environments that span the time interval of interest are used. Each static environment represents a “snapshot” or a “freeze frame” in time of the moving environment. For each of freeze frames a ray tracing computation is

performed. Thus, a set of eigenrays with complex amplitudes and arrival times that describe the propagation through the watercolumn is produced at the instant associated with for freeze frame of interest [14].

In environments of practical interest (e.g., sea surface) there is a time-varying motion during the time that the eigenray transits the underwater acoustic channel. The transit time of source signal can be long enough for significant motion to occur in the environment. However, the environment is assumed to be static during the entire time that the eigenrays of source signal transit the watercolumn for each “snapshot” of the environment in order to perform ray tracing computation in the *full* VirTEX algorithm. Therefore, for eigenrays that interact with the time-evolving sea surface causality of interactions is not modeled exactly [14].

The end result about VirTEX algorithm is a piecewise continuous representation of arrival function by assembly of ray tracing results for each “snapshot”. The notional depiction of the arrival function of a single eigenray is shown in Figure 4.1. Time difference between the temporal snapshots of the environment can be reduced in order to reduce the error due to piecewise continuous representation of the arrival function. Therefore, in order to increase accuracy of VirTEX algorithm performing more ray trace computations is needed by increasing the computational time.

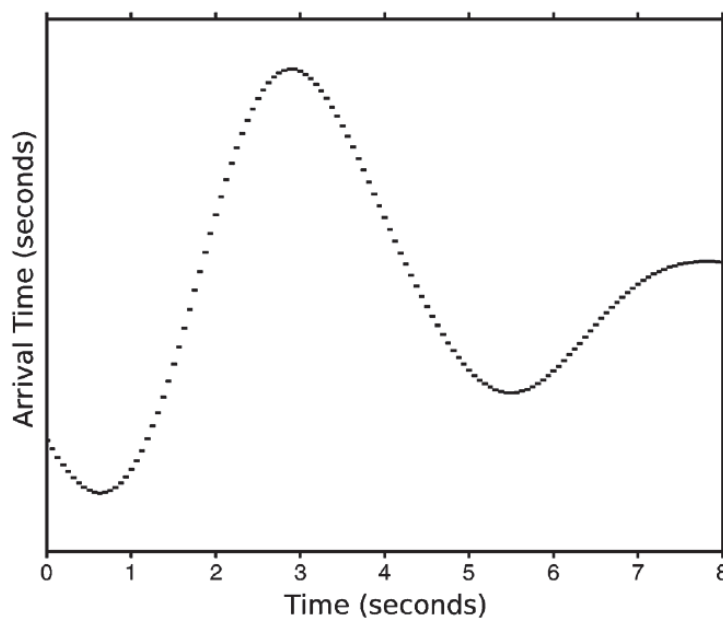


Figure 4.1: A Notional Example of Piecewise Continuous Approximation to the Arrival Function for a Single Eigenray Computed by the VirTEX Algorithm [14]

Significant Doppler spread can be introduced simply from the acoustic signal interacting with the moving sea surface. However, the effects on source signal are much greater when the source and receiver are also in motion [4]. In the VirTEX a ray-based approach is used to model moving sources/receivers as well as a time-varying sea surface. In this thesis, only interpolation method of VirTEX for time-varying sea surfaces is needed to combine with time-evolving sea surface wave field model. However, VirTEX algorithm is explained in the following sections for both moving sources/receivers case and time-varying sea surface case in order to keep in loyal to original algorithm given in [4].

4.2 Modeling Source and Receiver Motion with Rays

In this section, an implementation of two dimensional ray methods is extended to treat moving receivers and sources [4]. The complex pressure field, $P(\omega)$, can be represented as a sum of N arrival amplitudes $A_n(\omega)$ and delays $\tau_n(\omega)$ in a ray formulation given by

$$P(\omega) = S(\omega) \sum_{n=1}^N A_n e^{i\omega\tau_n} \quad (4.1)$$

where $S(\omega)$ denotes the spectrum of the source signal. An azimuthally symmetric geometry is assumed in this thesis. In order to compute amplitudes of the eigenray arrivals and arrival delays two-dimensional Gaussian beam tracing method which is implemented in BELLHOP program is used.

Since a product of two spectra is a convolution in the time domain, the corresponding time-domain representation for the received waveform, $p(t)$, can be written as

$$p(t) = \sum_{n=1}^N A_n(t) s[t - \tau_n(t)] \quad (4.2)$$

where $s(t)$ denotes the acoustic waveform of the source. Equation (4.2) shows how the acoustic signal is represented as a sum of echoes of the transmission with associated amplitudes and delays [4]. In order to allow the underwater acoustic

channel to be time-varying, a time dependency is introduced in the amplitudes and delays. Both source/receiver motion and time-evolving sea surface can cause this time variation.

The calculation of timeseries observed at the hypothetical receiver from an arrival of an eigenray is a straightforward process. For each of the transmit times (t_i) a corresponding arrival time ($\tau(t_i)$) is computed by BELLHOP ray tracing program. A “wall clock arrival time” is introduced to facilitate calculation of received timeseries [14]. The wall clock arrival time is denoted by $w(t_i) = t_i + \tau(t_i)$. After tabulation of all values of arrival function ($t_i, \tau(t_i)$) for the given eigenray received timeseries can be calculated. If a disturbance that left the source at wall clock time t_s , it arrives via the given eigenray at the hypothetical receiver point at the wall clock time $t_r = w(t_s)$. Therefore, in order to compute the amplitude of this timeseries for given eigenray at the arbitrary time t_r at the receiver, it is needed to find time t_s such that $t_r = w(t_s)$.

The desired time t_s can be found by inverse function evaluated at t_r , namely $t_s = w^{-1}(t_r)$. In order to find desired time t_s numerical interpolation of the tabulated values ($w(t_i), t_i$) is made. Unless there is no environmental motion that exceeds the local sound speed in the watercolumn, inverse function $w^{-1}(t)$ is exists and unique since it is monotone increasing. In Figure 4.2 there are graphical depictions of the wall clock time function $w(t)$ for (a) steady (source/receiver motion) and (b) unsteady (sea surface motion) motion cases. The process to evaluate t_s for a given value of t_r is shown in Figure 4.2 as well.

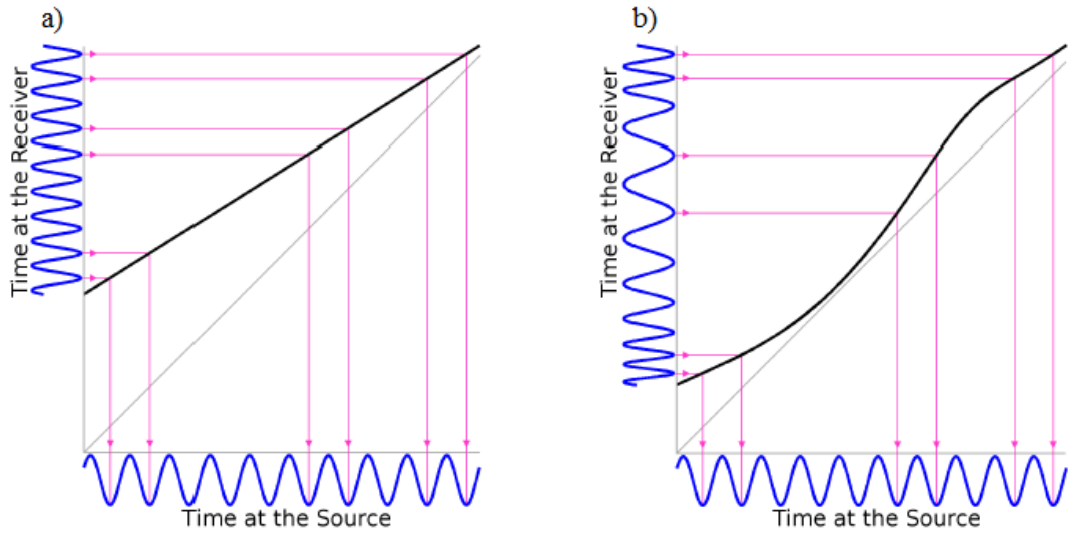


Figure 4.2: A Notional Example of the Wall Clock Time Arrival Function $w(t)$ (a) Steady Motion Case (b) Unsteady Motion Case [14]

One t_s is determined the desired amplitude of the time series observed at the receiver at time t_r is calculated from the source timeseries. All the arrival timeseries associated with eigenrays is summed up in this way.

Since the amplitudes in Equation (4.3) are actually complex numbers, the situation is a bit more complicated. The complex amplitudes are caused by the bottom reflections that introduce a phase shift (e.g., a $\pi/2$ phase shift) for example. It does not simply introduce an additional time delay, because this is a constant phase shift over frequency. Therefore, application of the convolution theorem is restated as

$$p(t) = \sum_{n=1}^N \text{Re}[A_n(t)] s[t - \tau_n(t)] - \text{Im}[A_n(t)] s^+[t - \tau_n(t)] \quad (4.3)$$

where $s^+ = \mathcal{H}(s)$ denotes the Hilbert transform of $s(t)$. The Hilbert transform is a 90° phase shift of version of $s(t)$ and accounts for the imaginary part of A_n . An interpretation of Equation (4.3) is that in order to provide an arbitrary phase change a weighted sum of the original waveform and its 90° phase-shifted version can be used [4]. The weighting provides the control of the effective phase shift.

VirTEX code aims to simulate the received field in cases where the receiver and/or sea surface is in motion as one of its main goals [4]. The arrival amplitudes and delays in Equation (4.3) change continuously in time when there is a steady or unsteady motion in the environment. Therefore, at each time step of the acoustic signal transmission new values for A_n and τ_n are required. As a theoretical approach a new ray trace can be performed at each step of the transmission in order to compute a new set of arrival amplitudes and delays of the rays. However, it requires intolerably long computation time. It can be unnecessary as well since changes in arrival amplitudes and delays are likely to be very small between time steps of transmission. As an alternative way, amplitudes and delays of rays are computed on a relatively sparse grid of points in range and depth. In order to compute the information of rays at any given location and time in the watercolumn an interpolation scheme is applied. Interpolation scheme is critical to obtain accurate received time series.

There are some subtleties in the interpolation scheme of amplitudes and delays of the rays. Figure 4.3 shows four neighboring grid points which receiver is located at inside a particular time step of transmission. If the pressure field of the interior receiver point is calculated by using straightforward interpolation of the arrival amplitude and delay from the four grid points to the receiver location, it can lead a problem since arrival patterns on one grid point possibly do not correspond to those at other grid points. At each grid point there can be different number of arrivals and arrival types due to reflections and refractions (when sound speed is not constant) in the sound channel. For example, a direct arrival which reaches to a grid point can reach to another grid point after bouncing from the sea bottom due to refraction and interpolation of these grid points can produce incorrect results. In addition, in order to do a proper interpolation, an excessive storage capacity can be required since all arrivals with their types are required to be tracked.

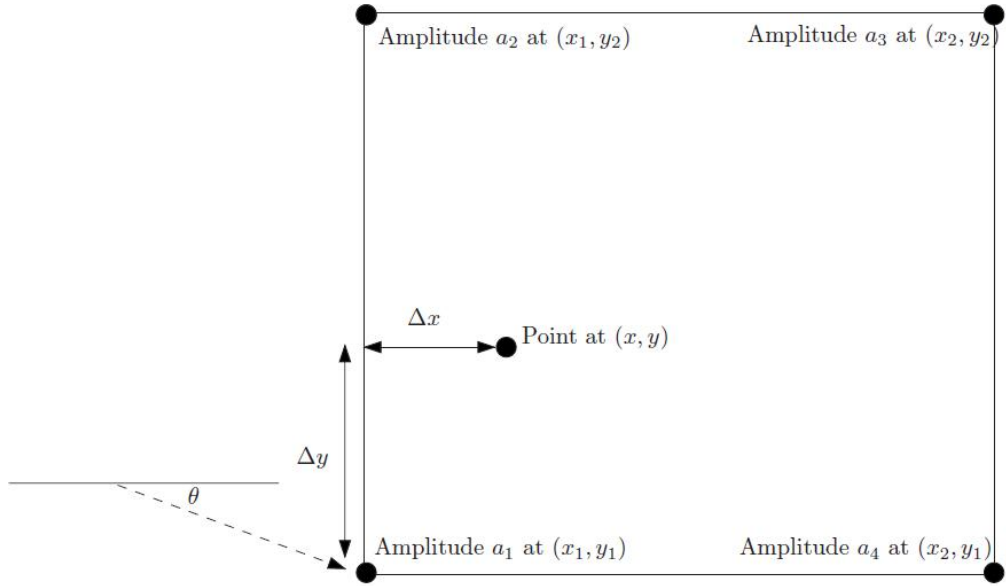


Figure 4.3: Four Points of the Computational Grid for a Ray Trace. The Actual Arrivals are Computed at the Four Corners and any Point in the Interior Computed through Interpolation of the Amplitudes and Extrapolation of the Delays. A Sample Arrival is Shown Travel [4]

A different interpolation approach is suggested in Siderius and Porter [4]. In this approach, the amplitudes of the rays at the four grid points are maintained as separate quantities. Arrival delays which correspond to arrival amplitudes are corrected by the ray path travel time differences between the points of the computational grid and the receiver point (x, y) . In the geometry of Figure 4.3 it is shown that an arrival indicated as a dashed line reaches to the lower left grid point at angle θ . The arrival delay time for that ray is adjusted from position (x_1, y_1) to position (x, y) by the distance divided by sound speed given as

$$\Delta_{delay} = (\Delta x \cos \theta + \Delta y \sin \theta) / c \quad (4.4)$$

where, for example, $\Delta x = x - x_1$, is positive (increased delay) with respect to position 1.

The arrival amplitudes from each of the grid points are weighted in order to contribute the pressure field at the receiver point given by

$$\begin{aligned}
& (1 - w_1) \times (1 - w_2) \times a_1 \\
& (1 - w_1) \times w_2 \times a_2 \\
& w_1 \times w_2 \times a_3 \\
& w_1 \times (1 - w_2) \times a_4
\end{aligned} \tag{4.5}$$

where, a_1 , a_2 , a_3 , and a_4 denote the arrival amplitudes at each point at the computational grid and weights are given by

$$\begin{aligned}
w_1 &= (x - x_1)/(x_2 - x_1) \\
w_2 &= (y - y_1)/(y_2 - y_1)
\end{aligned} \tag{4.6}$$

In the interpolation scheme, w_1 and w_2 represent a proportional distance in the x and y direction respectively. In summary, the pressure field at the receiver point is obtained by using Equation (4.3) summation of weighted amplitudes computed at four corners computational grid.

4.3 Modeling Time Varying Sea Surfaces

In Section 4.2 only the motion of the receiver is considered and it can be admitted as an approximate solution for the case when both source and receiver are moving horizontally when the sound speed profile is range independent. A time-evolving sea surface can also be added to the model (with receiver motion only) with slight modifications [4].

In order to modify the described algorithm described in Section 4.2, it is required to perform additional ray traces in order to sample the time-evolving sea surface. Figure 4.4 presents a diagram which shows required interpolation scheme to include sea surface motion. It is depicted that at an initial time, $t = t_a$, the rough sea surface has an arbitrary shape and sea surface waves evolve in time to produce a sea surface shape defined at time $t = t_b$.

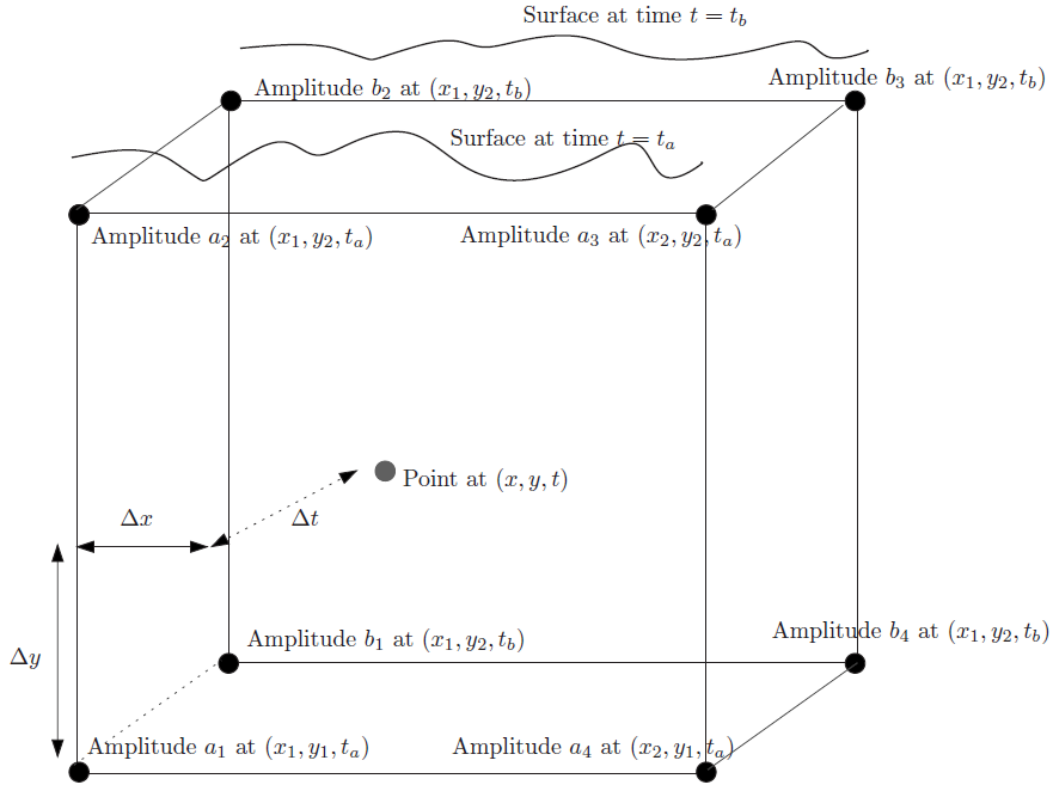


Figure 4.4: Same as Figure 4.3 Except with the Added Dimension to Allow for Time Changing Surface [4]

The time interval to sample the surface adequately is typically much greater than the sampling interval for the acoustic transmission. Therefore, in order to compute pressure field at the receiver point for all time steps ray arrival amplitudes and delays are computed for surfaces at $t = t_a$ and $t = t_b$ and trilinear interpolation is used similar to bilinear interpolation described at previous section. However, arrival delays are not extrapolated to the third dimension as a difference. In the interpolation scheme with sea surface motion again the arrivals are kept as separate quantities on each of the eight corners of the cube depicted in Figure 4.4. In order to determine the proper arrival amplitudes and delays the weights applied to the eight corners of the computation grid are used. The arrival delays at each corner of the cube are adjusted (advanced or retarded) according to distance as well. The weights given to each corner is determined by

$$(1 - w_1) \times (1 - w_2) \times (1 - w_3) \times a_1 \quad (4.7)$$

$$(1 - w_1) \times w_2 \times (1 - w_3) \times a_2$$

$$w_1 \times w_2 \times (1 - w_3) \times a_3$$

$$w_1 \times (1 - w_2) \times (1 - w_3) \times a_4$$

$$(1 - w_1) \times (1 - w_2) \times w_3 \times b_1$$

$$(1 - w_1) \times w_2 \times w_3 \times b_2$$

$$w_1 \times w_2 \times w_3 \times b_3$$

$$w_1 \times (1 - w_2) \times w_3 \times b_4$$

where a_1 , a_2 , a_3 , and a_4 denote the arrival amplitudes at $t = t_a$ at each corner and b_1 , b_2 , b_3 , and b_4 denote the arrival amplitudes at $t = t_b$ at each corner of computational grid. The weights are given by

$$\begin{aligned} w_1 &= (x - x_1)/(x_2 - x_1) \\ w_2 &= (y - y_1)/(y_2 - y_1) \\ w_3 &= (t - t_a)/(t_b - t_a) \end{aligned} \tag{4.8}$$

Since time interval between t_a and t_b is typically much greater than the acoustic sampling time interval, many of the time steps of acoustic signal transmission depend on interpolated arrival function in VirTEX code.

In Siderius and Porter [4], a comparison is made between the result of developed VirTEX algorithm and the exact solution for a given case. The exact solution is obtained based on method of images technique [8] for an isovelocity underwater acoustic channel with flat sea surface which can vary in height over time. The impulse responses of the channel computed with by the exact solution and using ray-based interpolation method (VirTEX algorithm) are almost in perfect agreement.

In this thesis, BELLHOP program is used as a ray tracer. For Equation (4.2), the channel impulse responses (arrival amplitude-delay pairs) calculated via BELLHOP

tool varies for different time instances t_a and t_b dramatically, if $|t_a - t_b| > T_c$, where T_c is channel coherence time. When maximum absolute frequency shift is f_d from frequency of source signal, T_c is defined as $1/f_d$. In this thesis, frequency of acoustic signal is 1 kHz and expected (extreme) maximum Doppler shift (f_d) is 10 Hz . Therefore, sea surface wave realizations by using wave model and results of BELLHOP program are generated with a time step equals to 0.1 second (T_c) without degrading the accuracy excessively.

In this study VirTEX code is used for environments which include only time-evolving sea surface motion. Receiver and/or source motion is not in scope of this thesis. By using interpolation scheme expressed in this chapter and Equation (4.2) or Equation (4.3) the received timeseries can be obtained from source timeseries in order to observe amplitude fluctuations of the received acoustic signal.

CHAPTER 5

COUPLED MODEL & DISCUSSION OF SIMULATIONS

5.1 BELLHOP and Time-evolving Sea Surface Wave Model

Integration

Impacts of time-evolving sea wave motion on acoustic signal are important for performance of underwater communication and sonar systems. In order to take into account the effect of sea surface, empirical data obtained from measurements in the ocean (e.g., [7] and [27]) are used combined with acoustic propagation model. VirTEX code, [4], makes simulation of time-varying environment possible in a manner repeated applications of BELLHOP ray tracer which gives impulse response of the underwater acoustic channel for every realization. Time series at hypothetical receiver location is generated by convolving source time series and time-varying impulse response of the channel provided by proper interpolation scheme of impulse responses of static environment at time different time instances. In this thesis, time-varying sea surface model and BELLHOP Gaussian beam tracing tool are coupled in a similar way to [1] and [13]. Coupled model in this study does not include the out-of-plane scattering. For modeling effects of out-of-plane scattering it is needed a 3D beam tracer combined with 2D realizations of the ocean surface. Order of out-of-plane scattering is not so critical in the simulations of this work, because grazing angle of acoustic signal is small leading to negligible out-of-plane scattering from sea surface as stated in [13].

Since purpose of this thesis is to investigate relationship between underwater channel characteristics and environmental parameters such as wind speed and fetch which affect the shape of the rough sea surface, only the surface reflected eigenrays are considered among this study. Modeling approach given in this study is similar to [1] and [13], but amplitude fluctuations of acoustic signals can be also seen via coupled model in this thesis by applying the VirTEX algorithm which computes received

timeseries for any given source timeseries. Thus, a complete model with time-evolving sea surface waves in order to observe the effects on acoustic signal is obtained. Coupled model provides the information of fluctuation of arrival times, arrival angles, and Doppler shift of eigenrays along the transmission of source signal in a moving top boundary of watercolumn. Time-varying impulse response of the channel is also calculated with arrival amplitude-delay files obtained for snapshots of time-evolving sea surface wave field and then VirTEX code is executed to generate received timeseries.

Modeling the underwater acoustic channel with environmental motion starts with realizations of rough ocean surface in order to import into ray-based model, BELLHOP which has a high computational speed. First component of the combination is 3D time-varying sea surface generation by using JONSWAP wave number spectrum and Hasselmann frequency dependent spreading function to obtain directional wave spectrum. Initial sea surface wave field is constructed according to that directional wave spectrum and a 2D cross-section of rough surface is taken in the downwind to supply an upper boundary to BELLHOP program as an input altimetry file. The altimetry file is formed by range and corresponding height data of the ocean surface. Computational range is partitioned into small components with width of Δr . In application of BELLHOP ray tracer, source signal interacts with constructed ocean surface is reflected in a geometric manner dependent to grazing angle of acoustic wave and slope of the rough surface at the reflection point. In Figure 5.1 there is an illustration of snapshot of time-varying 3D sea surface and its corresponding 2D cross-section at downwind direction. It can be seen that waveheight of the ocean waves obtained by the sea surface wave model is almost equal to the value which is given by Beaufort wind force scale table (2-3m for 8.0-10.7 m/s wind speed). Construction of 3D initial sea surface wave fields are followed by solution of linear evolution equations numerically by fourth order Runge-Kutta (RK4) method. Thus time-evolving rough sea surface realizations are generated from 3D time varying sea surface again by taking 2D cross-sections at downwind along transmission time of the source signal.

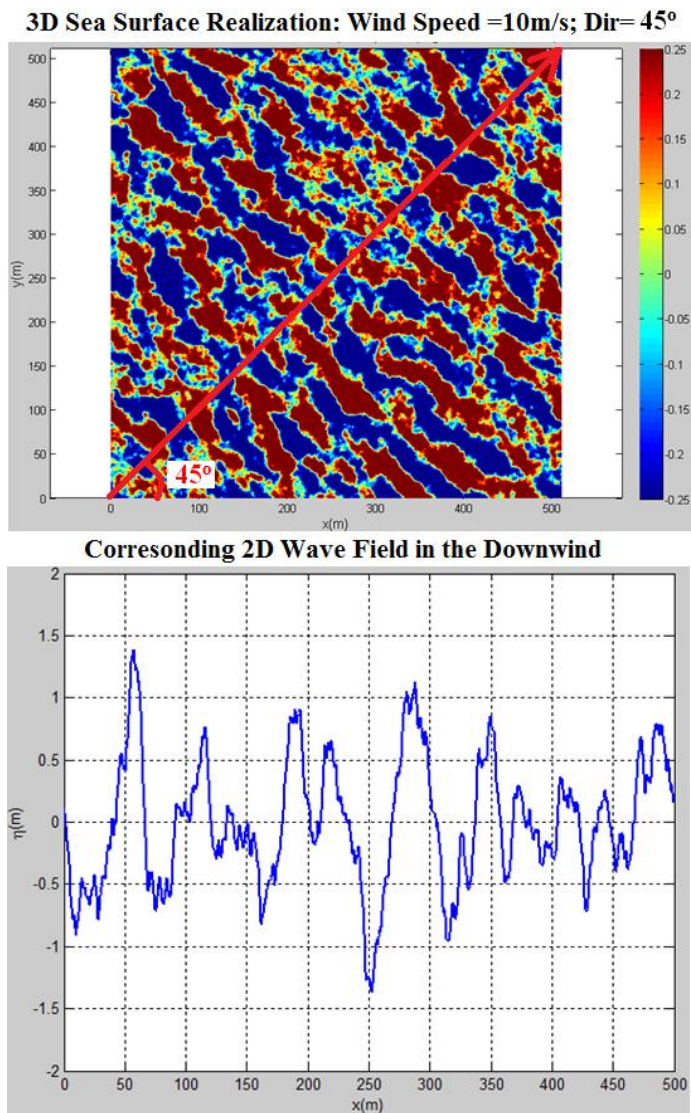


Figure 5.1: Time-varying Sea Surface Model. (top) Snapshot of 3D Time-varying Sea Surface Wave Field with Wind Speed 10m/s and at Wind Direction 45°. (bottom) Corresponding 2D Cross-section of 3D Sea Surface Snapshot

For any realization of rough sea surface BELLHOP program operates two times with output options of arrival amplitude-delay file and eigenray file in the combined model of BELLHOP tool and realistic time-evolving sea surface waves especially for coastal areas. Several considerations are taken into account after output files are generated in order to track real arrivals. Firstly, arrival-amplitude files are observed and arrivals with low amplitude with respect to arrival with strongest amplitude are eliminated. In this thesis, arrivals with their amplitudes are smaller than the one a hundredth of the strongest arrival are neglected. Corresponding paths of the

eliminated arrivals are also deleted from the eigenray file. Then, eigenrays which are far from the hypothetical receiver point bigger than an acoustic wavelength ($\lambda = 1.5 \text{ m}$ in simulations) of source signal are eliminated from eigenray file. This is because of BELLHOP does not give exact eigenrays when rough surfaces are used as a boundary of the watercolumn. The corresponding arrivals of eliminated eigenrays are deleted from arrival-amplitude file as well. In Figure 5.2 eigenrays for a BELLHOP realization with rough top boundary is presented. Eliminated eigenrays because of being far from receiver are showed with red lines and eliminated eigenray due to low amplitude is showed with dashed line in that plot. Purple diamond represents specular reflection point for a given source and receiver geometry as well.

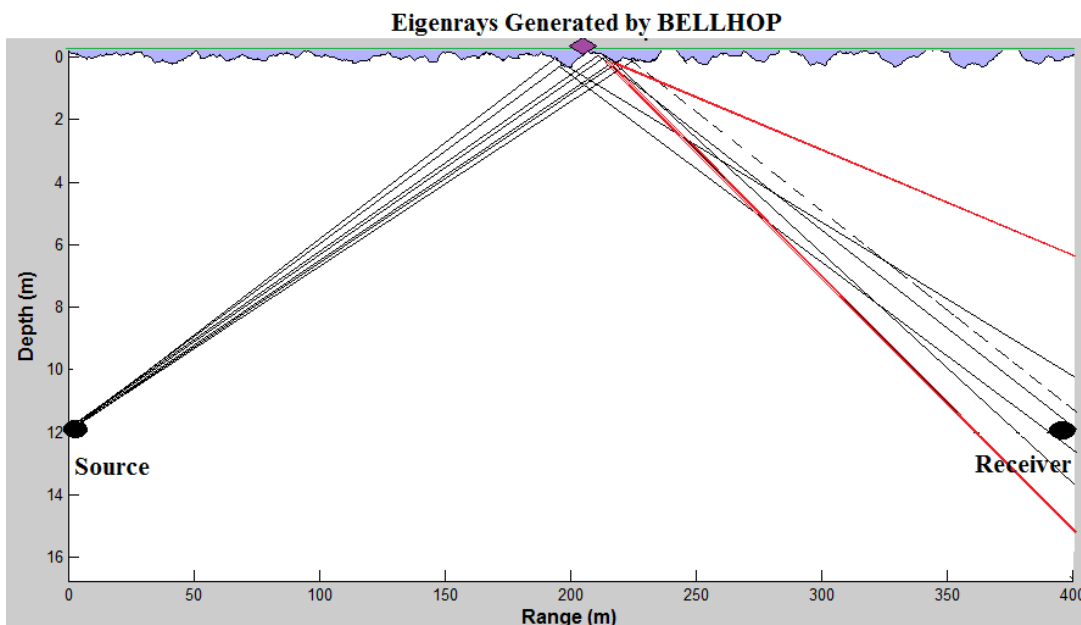


Figure 5.2: Plot of Eigenrays. Eliminated eigenrays are also showed. Red Lines are far from the Receiver and Dashed Line has a Low Amplitude

In this thesis, the effects of time-varying rough sea surface to acoustic sound which is reflected and scattered from sea surface are considered specifically. Therefore, a beam fan which is directed to the surface only is required to receive single sea surface reflected acoustic signals but multiple interactions with the sea surface are allowed. Similar to [1] and [13], a small portion of the sea surface (about several

surface wavelengths) is insonified to increase resolution and accuracy by using the same number of beams. Figure 5.3 is an illustration of geometry of acoustic sound wave scattering from ocean surface. Range of beam fan, $\Delta\theta$, is small and therefore insonified portion of sea surface, ΔR , is small as well. Red star in the Figure 5.3 represents specular point with respect to flat sea surface. For simulations in this chapter, grazing angle, θ_g , for the specular point is approximately 3.43° . Since acoustic wave energy scattered coherently in the specular direction and incoherently in all directions, a smaller of beam fan insonifies a portion on the sea surface in the vicinity of the specular point. Computational efficiency is supplied due to usage of the same number of beams with larger range of beam fan which insonifies the portion of sea surface of the same length. In the simulations bottom reflected eigenrays are not allowed. Prevention of bottom interaction of ray paths is provided by restricting computational domain of ray tracing in environmental file (*.env) of BELLHOP program.

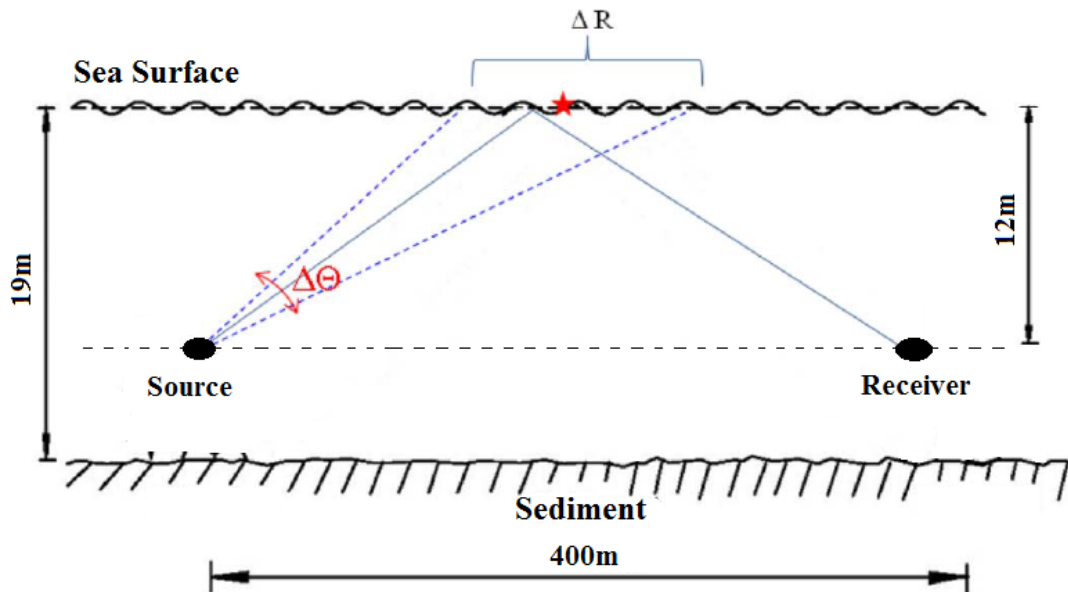


Figure 5.3: Geometry of Small Beam Fan to Increase Resolution with the Same Computational Speed, redesigned by [13]

In [1] and [13] the effects of sea surface resolution are also studied. Length of sea domain which acoustic waves propagate is partitioned to small surface widths, Δr to

generate ocean surface realizations. This partition needs to pay attention to representing sea surface wave fields without increasing computational speed dramatically. According to [13] number of eigenrays increases with decreasing width of surface partition, Δr . If number of surface partition, N_p , decreases, sea surface is not represented in a realistic manner after some point. N_p affects standard deviation of arrival times with respect to wind speed as well. Standard deviation of arrival times increases with increasing N_p , but there a convergence after some value. Hence, there is an optimum choice of N_p and $N_p = 1024$ is seemed enough for representing the sea surface realizations accurately in this study. Corresponding Δr is 0.43 m for that N_p value.

Taking into account these considerations, BELLHOP tool and linear time-evolving sea surface are combined for constructing a channel model to observe the effects of sea surface motion on high frequency acoustic signals. After preparation of environmental input file and altimetry file which defines sea surface boundary, BELLHOP program operates two times at each static environment and the channel impulse response and eigenray paths are given as output. Since BELLHOP tool traces the rays for stationary environments, channel impulse response obtained by BELLHOP expressed as

$$h(\tau) = \sum_{i=1}^N a_i \delta(\tau - \tau_i) \quad (5.1)$$

where N denotes the number of arrivals, a_i and τ_i are amplitude and delay of the i -th eigenray. Tracing of eigenrays includes due to motion of sea surface and incident angles and arrival times of eigenrays change over transmission time. In Section 2.6, calculation of Doppler shifts by using sea surface velocity potential which is computed by linear sea surface wave model is expressed in detail. For all realizations of the sea surface along transmission period Doppler shifts are calculated at interaction point(s) of eigenrays with the rough ocean surface.

Then, VirTEX code is applied to interpolate channel impulse responses of BELLHOP model in order to obtain received timeseries. After that whole picture of

channel with propagating rough sea surface is revealed and it is used to compute received timeseries from upsampled source timeseries by using convolution. Upsampling is done due to increase resolution for picking up pressure values transmitted by source at known time instances. VirTEX code uses the time varying channel impulse responses obtained by running BELLHOP for snapshots of time-varying environments (sea surface motion) as follows

$$h(t, \tau) = \sum_{i=1}^N a_i \delta(\tau - \tau_i(t)) \quad (5.2)$$

Figure 5.4 present a block diagram of the coupled model used in this thesis. In this figure, eigenrays of channel and blocks/sub-blocks require these eigenrays are highlighted with green frames and arrival time-amplitude outputs of the channel and blocks/sub-blocks require these amplitude-delay pairs are highlighted with red frames. Since Doppler shift calculations are made by finding interaction points of the eigenrays with the sea surface, the eigenray file output of BELLHOP program and Doppler shift calculation sub-block are shown in a green rectangular box. In addition, interpolation of channel impulse responses done in the VirTEX block which uses the results of arrival time-amplitude file corresponding to real eigenrays, hence this block is in rectangular boxes with both green and red colors. Simulations of this chapter are done using the model expressed in Figure 5.4 as well.

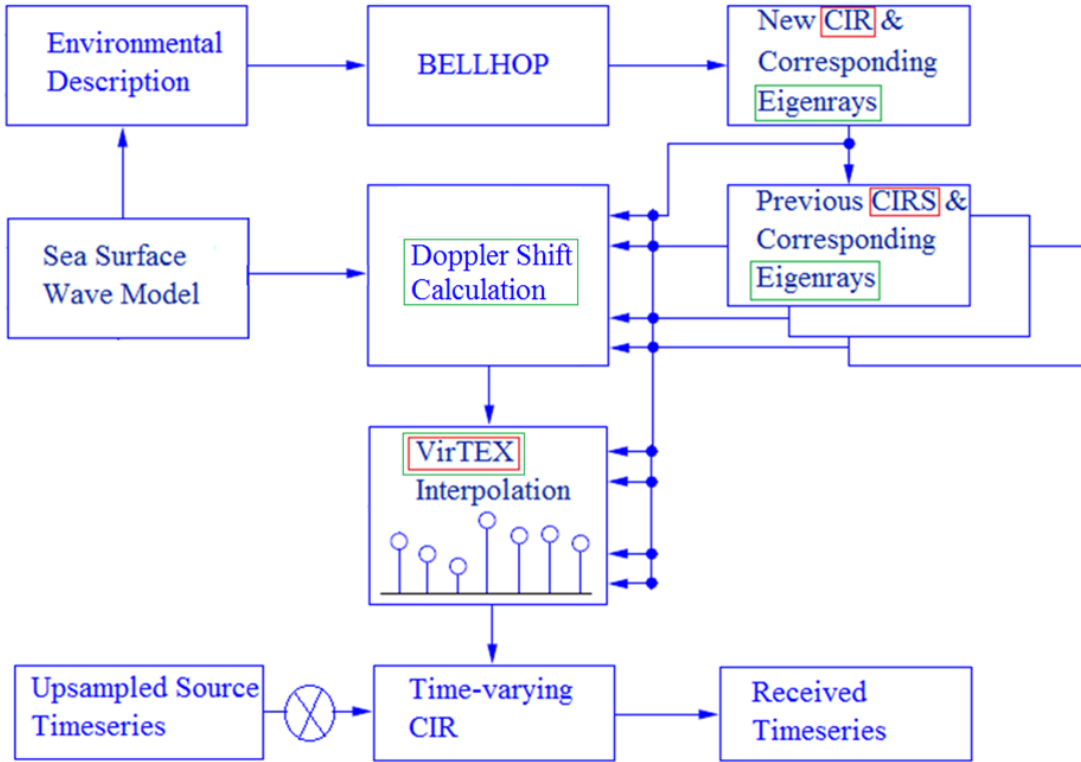


Figure 5.4: Block Diagram of the Coupled Model

5.2 Simulations and Discussions

Several parameters which are inputs to the BELLHOP program (environmental file, *.env) are constant for all simulations of the coupled model. These parameters are given in Table 5.1.

Table 5.1: Table of constant simulation parameters

Source Frequency	Source Depth	Receiver Range	Receiver Depth	Beam Fan Interval	Number of Beams	Sound Speed
1 kHz	12 m	400 m	12 m	2.8°-4.3°	1000	1500 m/s

Since one of the main purposes of this thesis is to obtain fluctuations of arrival times, arrival angles, and Doppler shifts of the eigenrays due to time-evolving motion of ocean boundary, the coupled model is operated for several environmental scenarios. For JONSWAP spectrum of sea surface waves used in this study, there are two

principal parameters to construct the wave field: wind speed (U) and fetch (X). In coastal areas fetch length (X) is generally a restricted value which is taken as 25 km in this study. Therefore, wind speed (U) is principal actor which affects sea surface wave field construction in the simulations. It is looked for a relationship between wind speed in a coastal area and temporal fluctuations of the eigenray arrivals.

Firstly, three simulations are set up for wind speeds (U) 1 m/s , 5 m/s , and 14 m/s respectively. An acoustic source signal with 15 s time duration is transmitted in these simulations through time-varying environment. For each wind speed (U) value arrival time, arrival angle, and Doppler shift fluctuations of the strongest eigenrays are plotted. In Figure 5.5-Figure 5.7 arrival time fluctuations are presented along the transmission time of the source signal.

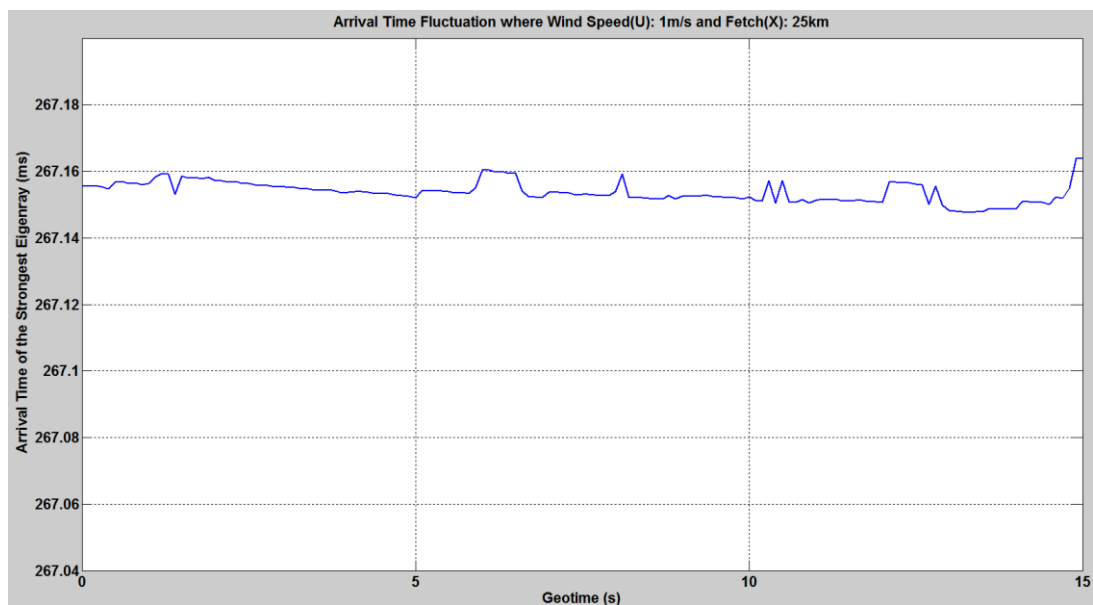


Figure 5.5: Arrival Time Fluctuation of the Strongest Eigenray: $U=1\text{m/s}$, $X=25\text{km}$

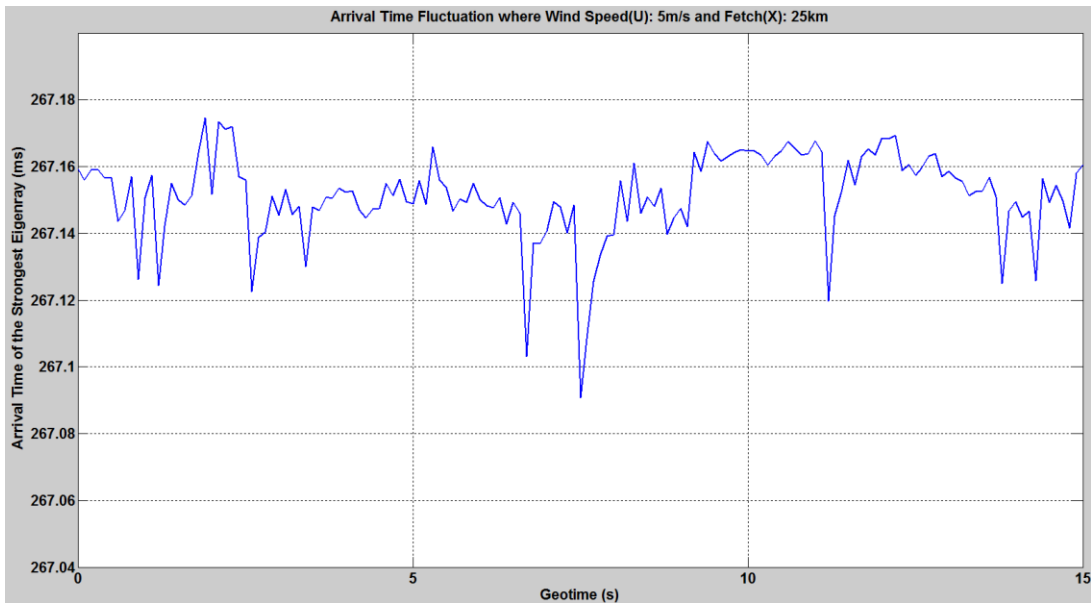


Figure 5.6: Arrival Time Fluctuation of the Strongest Eigenray: $U=5\text{m/s}$, $X=25\text{km}$

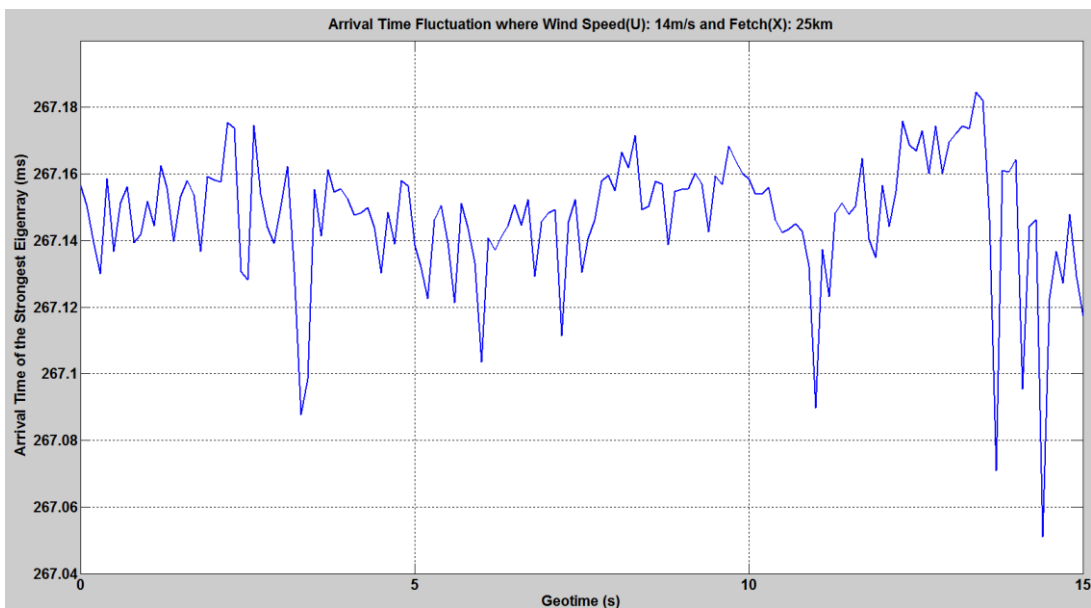


Figure 5.7: Arrival Time Fluctuation of the Strongest Eigenray: $U=14\text{m/s}$, $X=25\text{km}$

A comparison between arrival time fluctuations for these three different wind speeds can be made by Figure 5.8. It is obviously seen that variation of travel time of eigenrays increases with higher wind velocities. The eigenrays interact with crests and eigenrays interact with troughs have different arrival times. Since height of sea

surface waves rises by increasing wind speed, difference of arrival times of paths bounced from sea surface wave crests and troughs becomes greater.

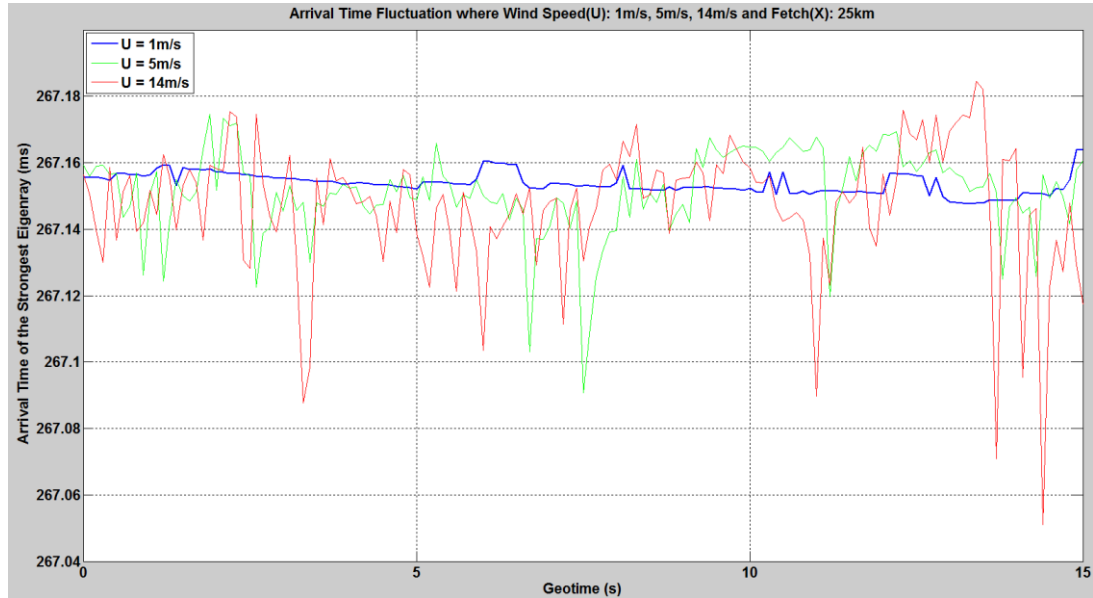


Figure 5.8: A Comparison of Arrival Time Fluctuations. Blue Line: $U=1\text{m/s}$, Green Line: $U=5\text{m/s}$, and Red Line: $U=14\text{m/s}$.

In Figure 5.9-Figure 5.11 arrival angle fluctuations of the eigenrays are illustrated for the given geometry of simulation set up showed in Figure 5.3.

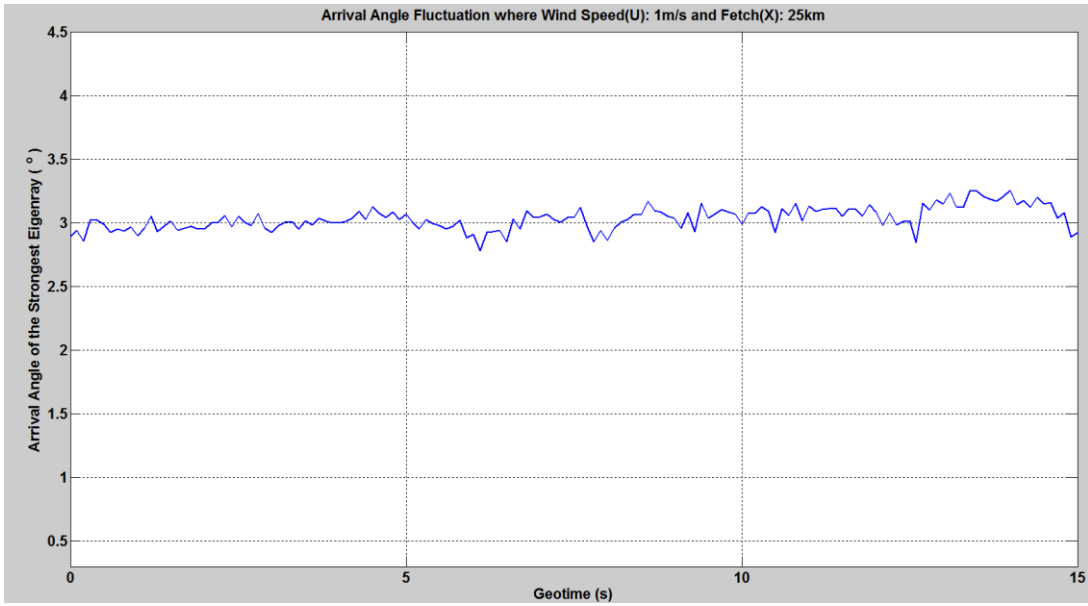


Figure 5.9: Arrival Angle Fluctuation of the Strongest Eigenray: $U=1\text{m/s}$, $X=25\text{km}$

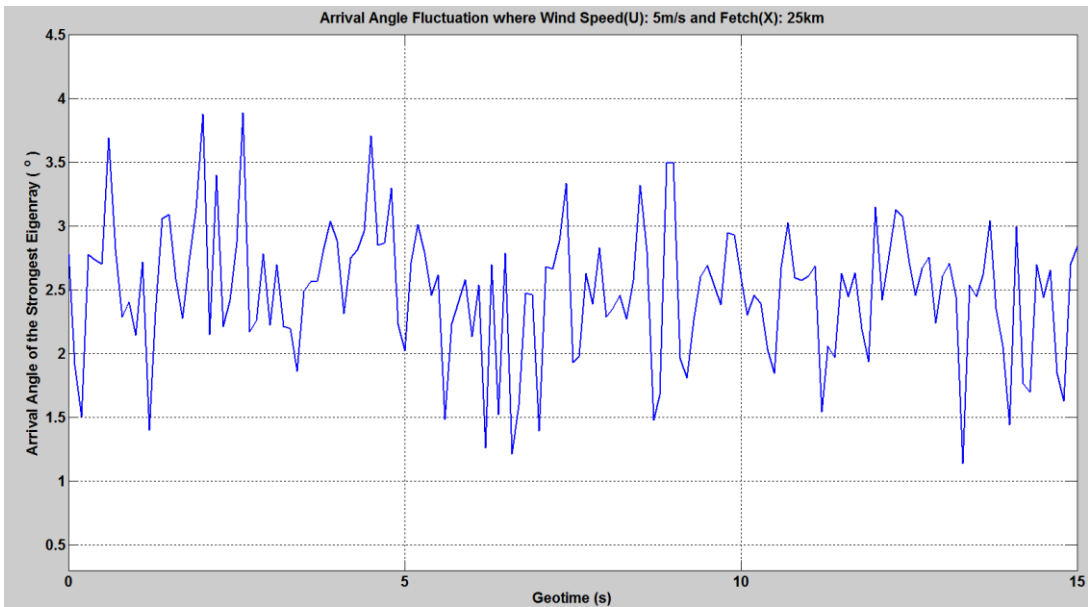


Figure 5.10: Arrival Angle Fluctuation of the Strongest Eigenray: $U=1\text{m/s}$, $X=25\text{km}$

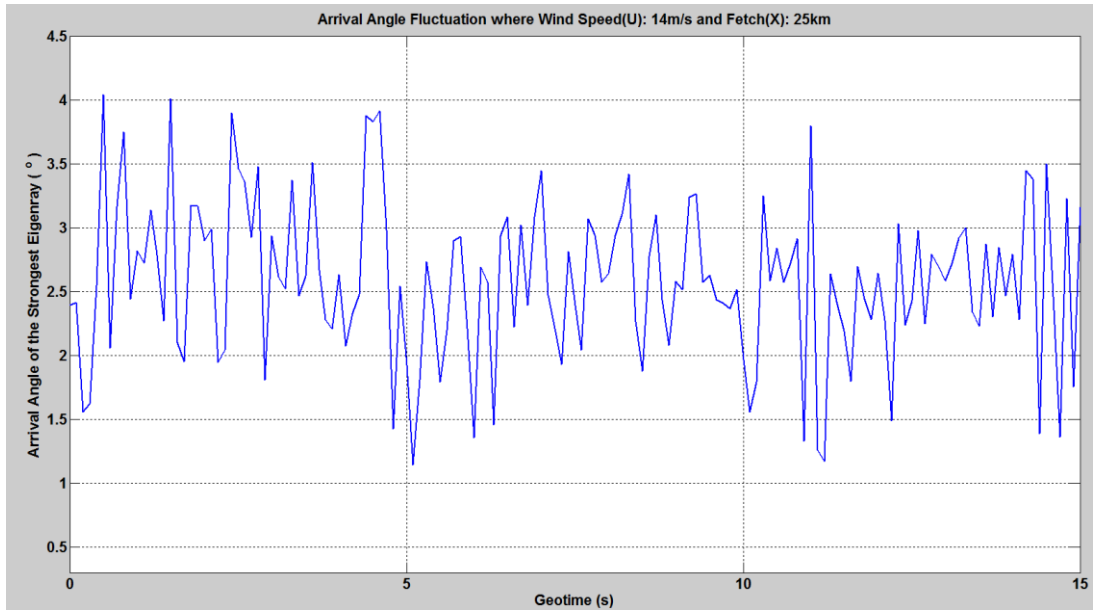


Figure 5.11: Arrival Angle Fluctuation of the Strongest Eigenray: $U=14\text{m/s}$, $X=25\text{km}$

Figure 5.12 presents again a comparison of arrival angle fluctuations with respect to different wind velocities. For wind speed, $U = 1\text{m/s}$, sea surface converges to a perfect reflector and arrival angle fluctuations are decreased. Acoustic signal is scattered to all directions when sea surface roughness gets bigger because bigger wind speed gets bigger.

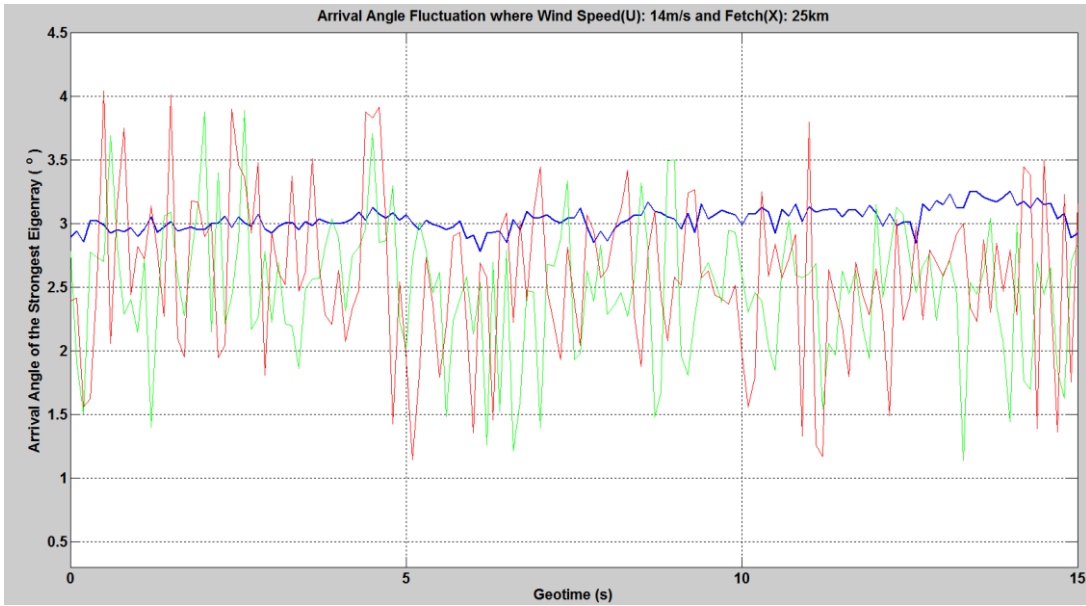


Figure 5.12: A Comparison of Arrival Angle Fluctuations. Blue Line: $U=1\text{m/s}$, Green Line: $U=5\text{m/s}$, and Red Line: $U=14\text{m/s}$.

Absolute Doppler shift fluctuations of the strongest eigenrays can be seen from Figure 5.13-Figure 5.15 as well.

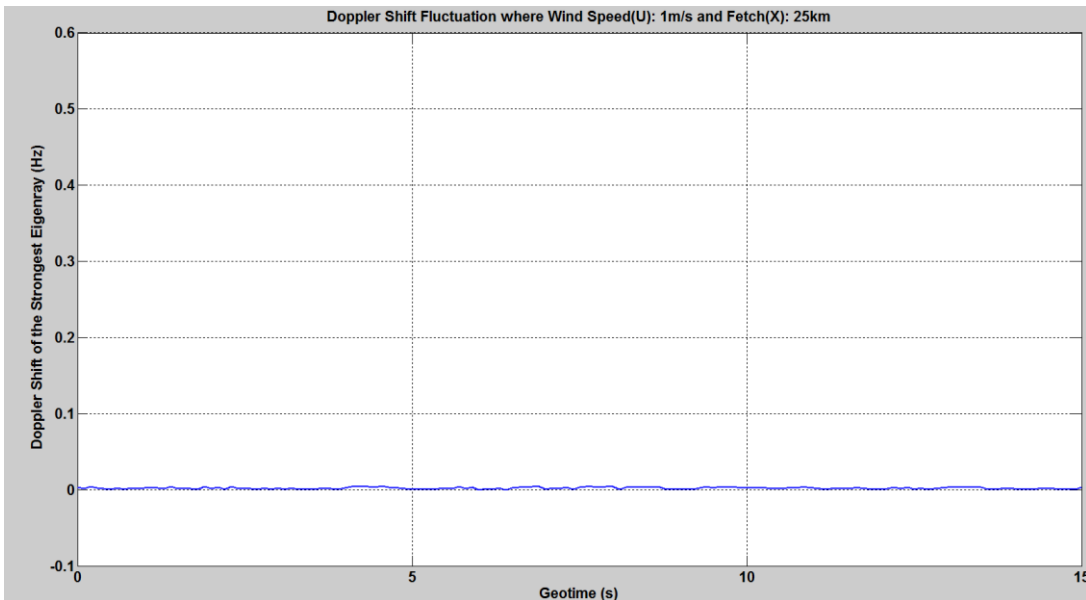


Figure 5.13: Doppler Shift Fluctuation of the Strongest Eigenray: $U=1\text{m/s}$, $X=25\text{km}$

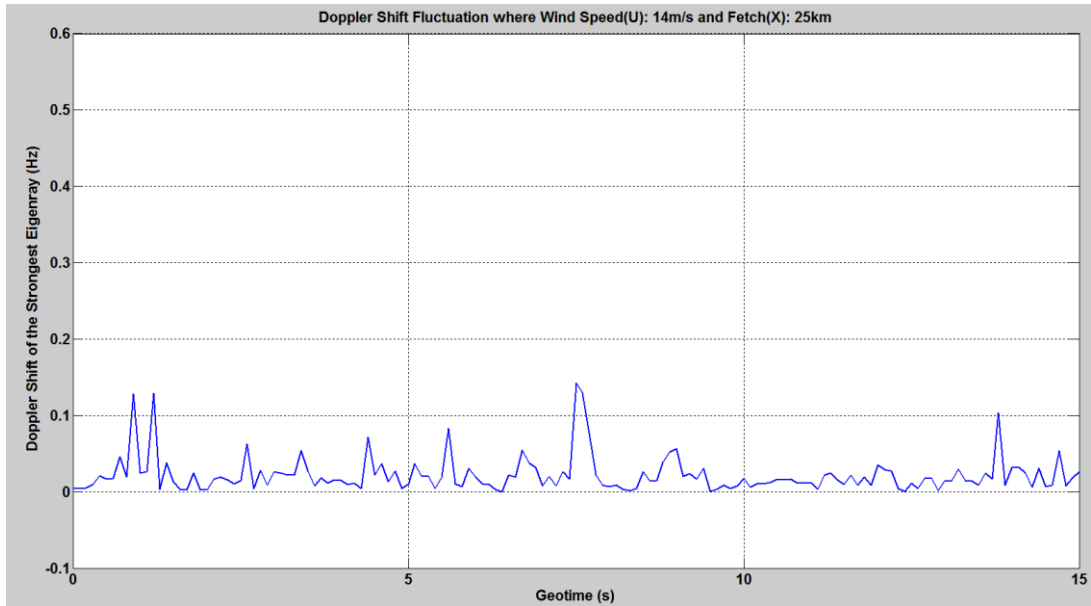


Figure 5.14: Doppler Shift Fluctuation of the Strongest Eigenray: $U=5\text{m/s}$, $X=25\text{km}$

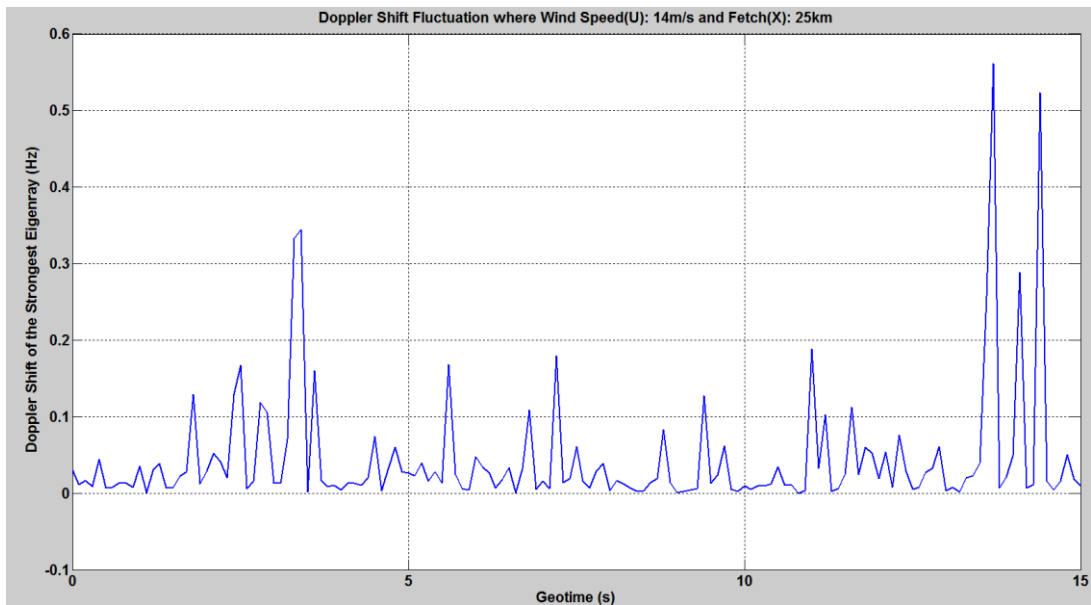


Figure 5.15: Doppler Shift Fluctuation of the Strongest Eigenray: $U=14\text{m/s}$, $X=25\text{km}$

Figure 5.16 also shows the relationship between Doppler shift and wind speed which is directly related to elevation and velocity potential of the sea surface. Normal velocity of reflection points on the ocean surface increases at high wind speeds. Therefore, higher Doppler shifts can be seen when the wind velocities are high. Variation of Doppler shifts becomes bigger for higher wind speeds as a result.

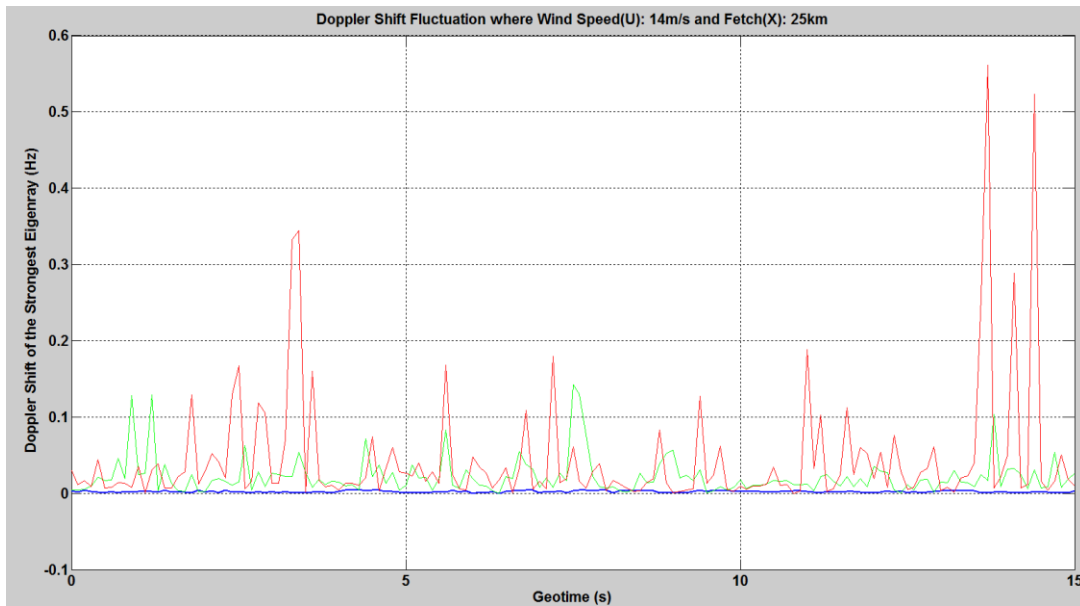


Figure 5.16: A Comparison of Absolute Doppler Shift Fluctuations. Blue Line: $U=1\text{m/s}$, Green Line: $U=5\text{m/s}$, and Red Line: $U=14\text{m/s}$.

The coupled model gives results of received timeseries for different wind speeds as well. In Figure 5.17 source signal timeseries (a) and received timeseries for wind velocities, $U = 1\text{m/s}$ (b), $U = 5\text{m/s}$ (c), and $U = 14\text{m/s}$ (d) as fetch length (X) is 25 km . Since roughness of the ocean boundary gets larger with greater wind speed, acoustic wave energy is scattered more and amplitude of received signal decreases at large wind speeds because of fading. Amplitude fluctuations of the received signals can also be observed from Figure 5.17.

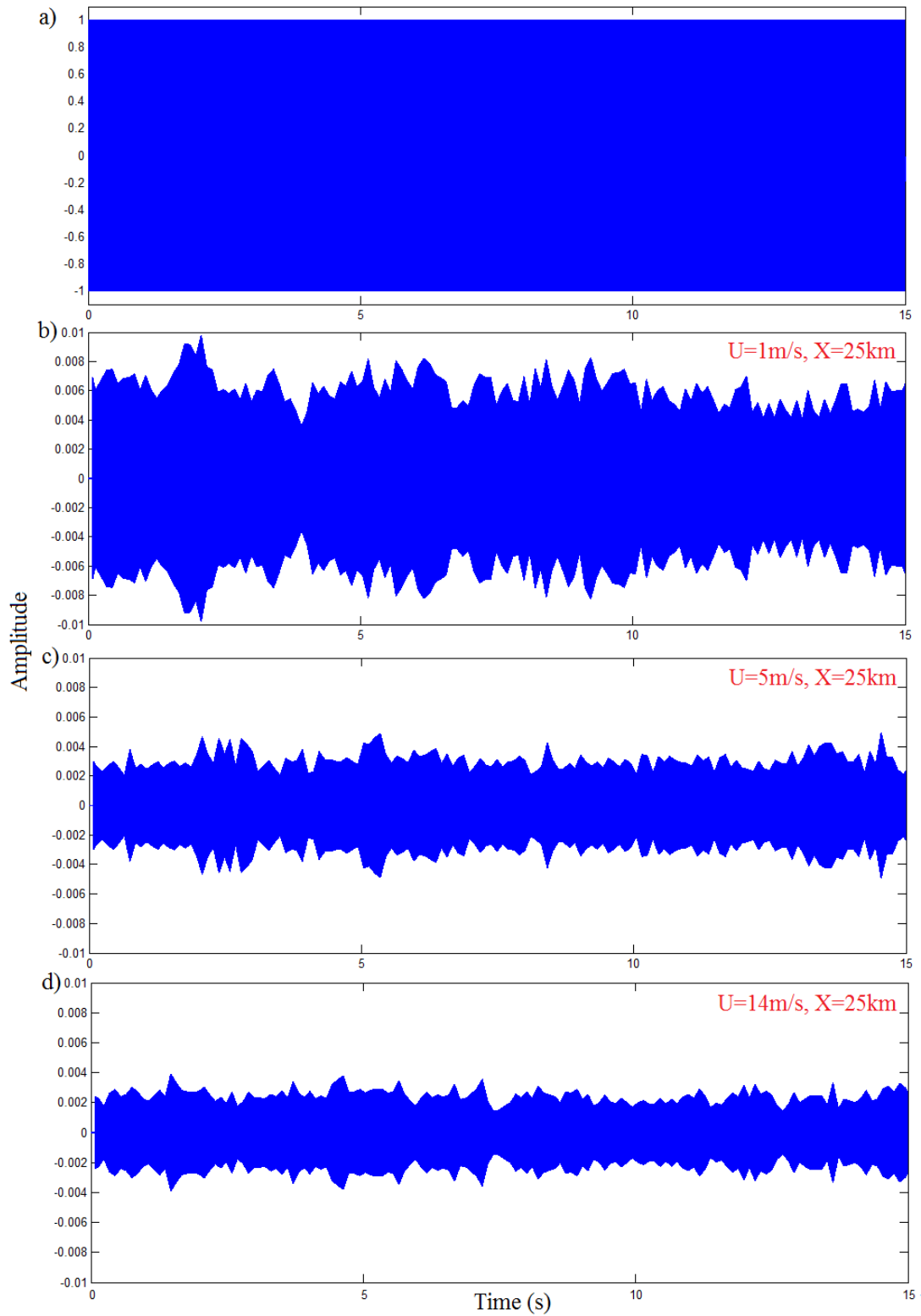


Figure 5.17: Time Series of Acoustic Signal. (a) Source Time Series (b), (c), and (d) Received Time Series for $U=1\text{m/s}$, $U=5\text{m/s}$, and $U=14\text{m/s}$ respectively.

The spectrogram for received time series for wind speed, $U = 14\text{m/s}$ and fetch length, $X = 25\text{km}$ is given in Figure 5.18 to illustrate frequency content of the source signal.

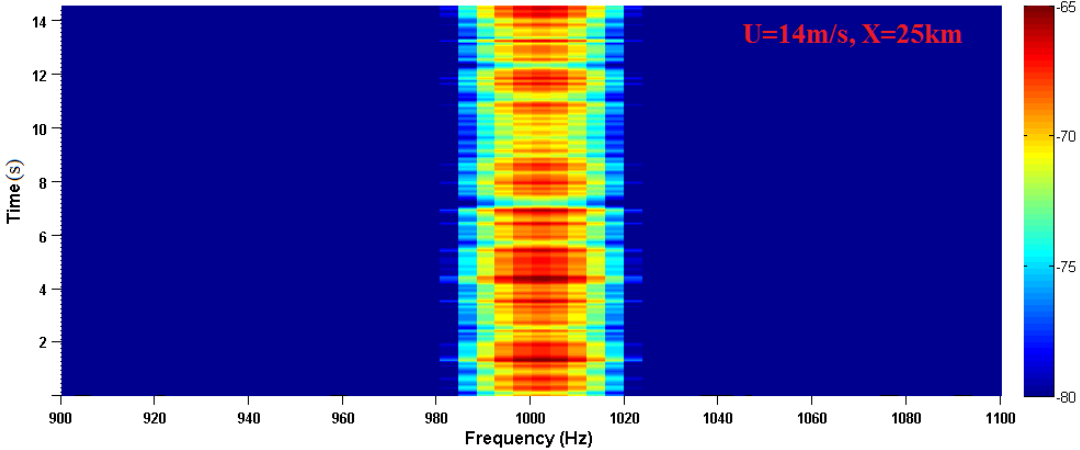


Figure 5.18: Spectrogram for Received Time Series for $U = 14\text{m/s}$, $X = 25\text{km}$.

Fetch length (X) is another important parameter for construction of initial sea surface wave field. If wind blows through a bigger area of ocean (fetch), sea surface waveheights becomes bigger as well. Therefore, an increasing effect of fluctuations of the acoustic signal is expected. Figure 5.19-Figure 5.21 ($X = 100\text{km}$) proves that expectation because range of fluctuations increase with respect to Figure 5.6, Figure 5.10, and Figure 5.14 (*where* $X = 25\text{km}$). The only difference between two group of figures is fetch (X) and wind speed is constant as ($U = 5\text{m/s}$).

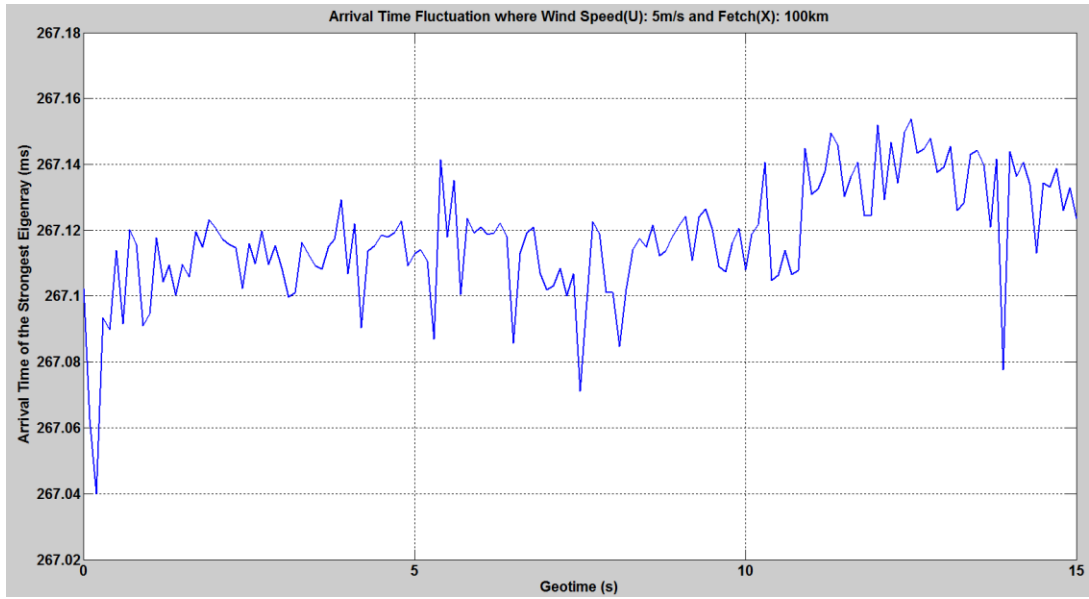


Figure 5.19: Arrival Time Fluctuation of the Strongest Eigenray: $U=5\text{m/s}$, $X=100\text{km}$.

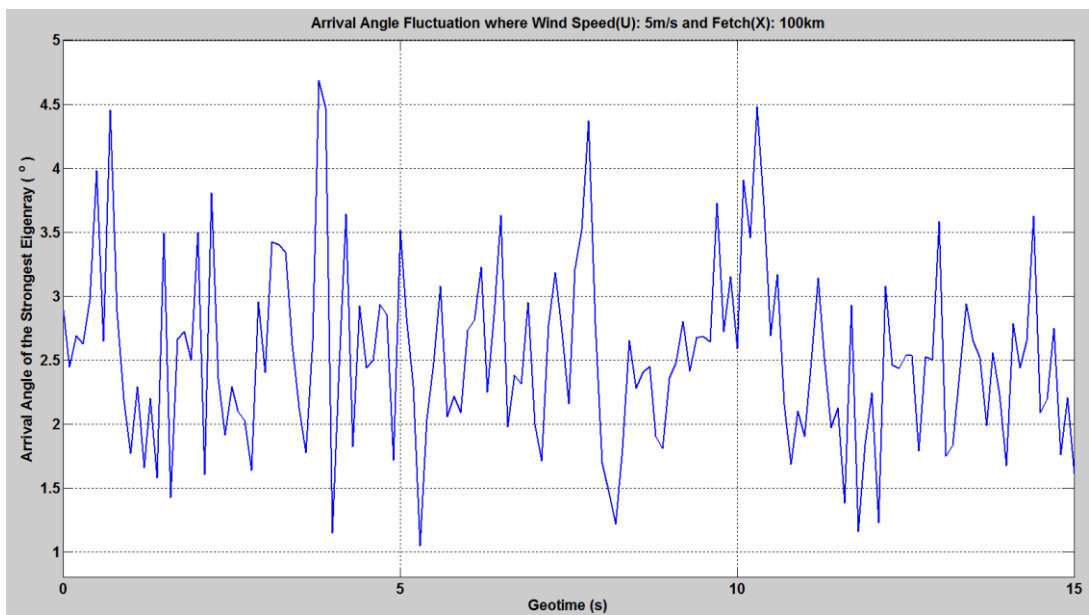


Figure 5.20: Arrival Angle Fluctuation of the Strongest Eigenray: $U=5\text{m/s}$, $X=100\text{km}$

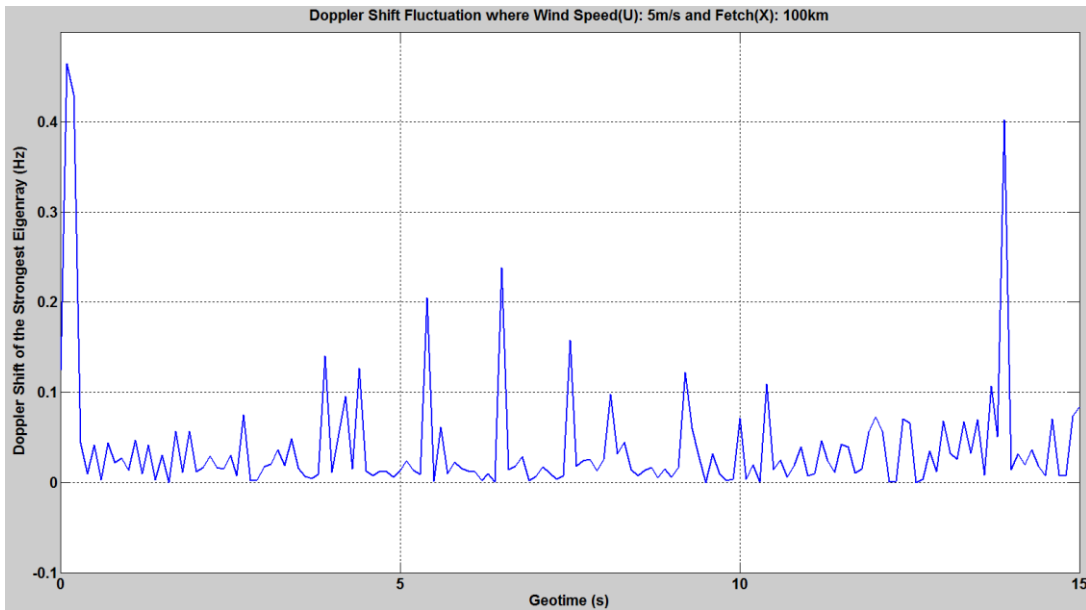


Figure 5.21: Doppler Shift Fluctuation of the Strongest Eigenray: $U=5\text{m/s}$, $X=100\text{km}$

Received time series of the acoustic signal (top) which is obtained in simulations for wind speed, ($U = 5\text{m/s}$) and fetch ($X = 100\text{km}$) is presented in Figure 5.22 with spectrogram of the received signal (bottom). It is obviously seen that the amplitude of the received signal decreases because of fading which increases at greater fetches.

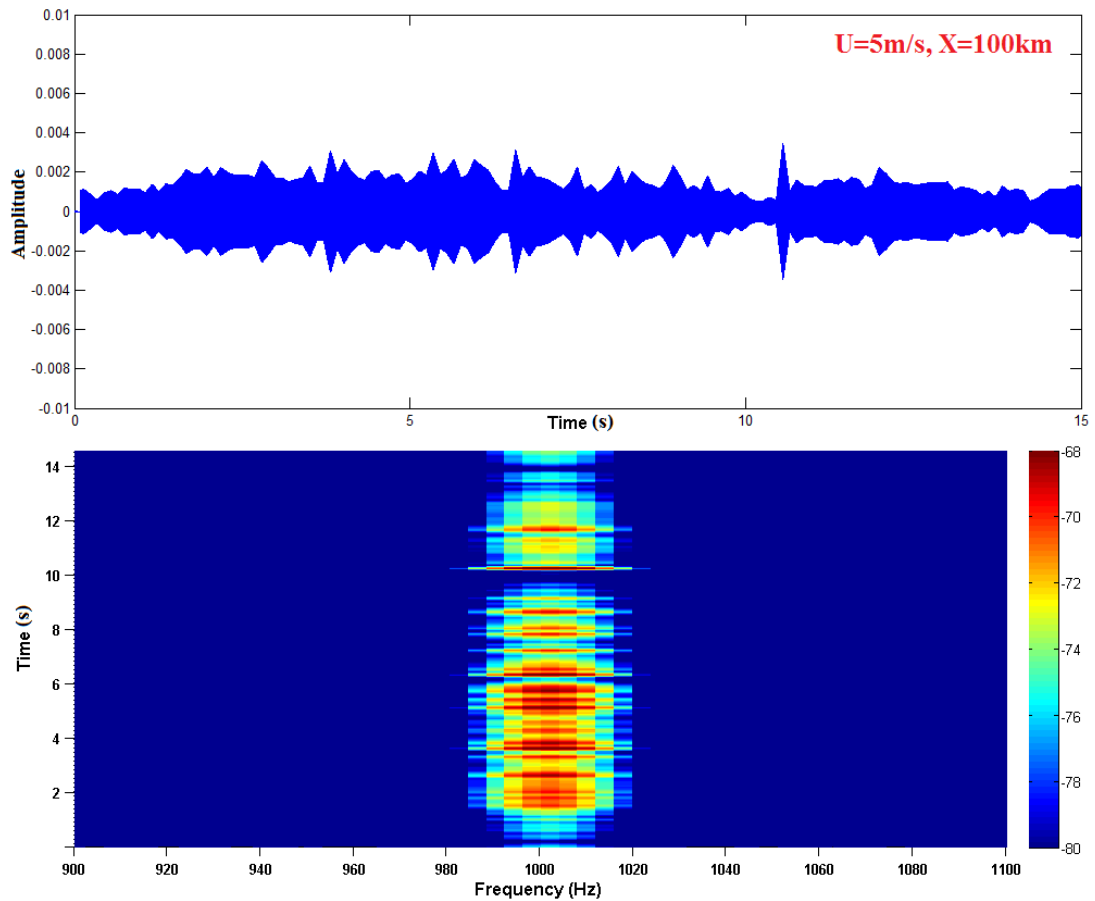


Figure 5.22: Received Signal for, $U=5\text{m/s}$, $X=100\text{km}$. (top) Received Time Series (bottom) Spectrogram of Received Time Series

The second group of simulations are made to focus on relationship between main environmental condition, wind speed (U) and statistics of acoustic signal fluctuations. Standard deviation of the signal fluctuations is chosen as the statistics parameters. The coupled model is applied to random realizations of the time-varying environment without computing the received timeseries. Monte Carlo simulations are performed 100 times at each of the wind speeds which have values in between $1 - 15\text{m/s}$ interval. For each random realization and for each wind speed arrival time, arrival angle, and Doppler shift of the strongest eigenray are calculated. After all realizations end for the given wind velocity, standard deviations of signal fluctuations are evaluated by post-processing. Figure 5.23-Figure 5.25 present standard deviations of acoustic wave fluctuations with respect to wind velocity (U).

The standard deviation of the arrivals increases almost linearly with wind speed. Path length of the eigenrays reflected from the sea surface crest is larger than eigenrays interacted with the sea surface trough. Difference between those path lengths becomes larger when wind speed gets larger. Therefore, arrival time variation of the eigenrays is high at high wind speeds as shown in Figure 5.23. Dashed line represents the fitted curve to the standard deviations in this figure.

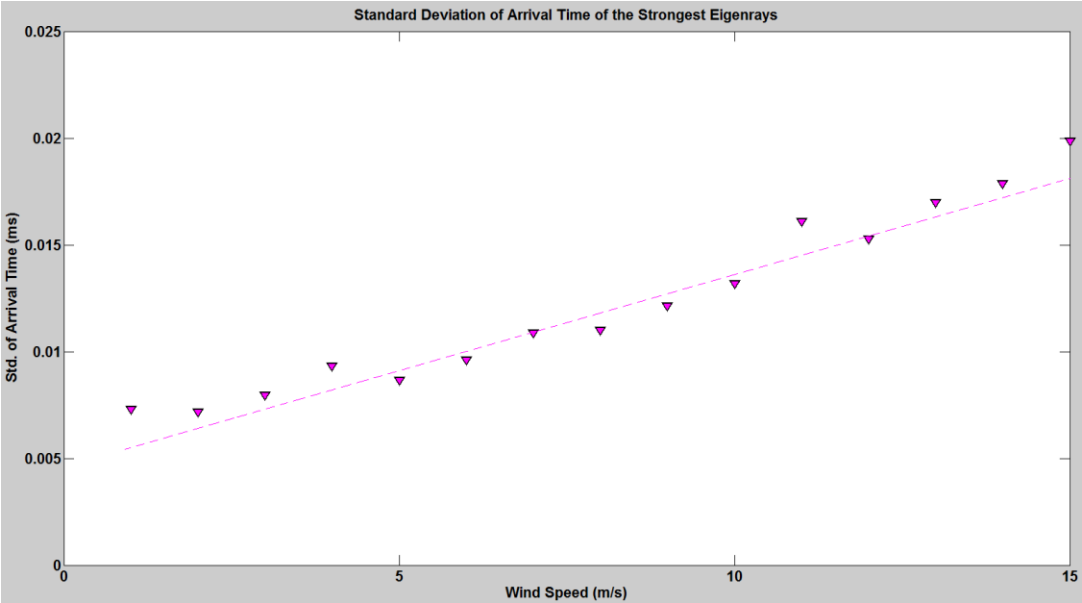


Figure 5.23: Standard Deviation of Arrival Time wrt. Wind Speed (U)

Since sea surface roughness leads to decrease of coherent energy in the specular direction and increase of incoherent energy in all directions, standard deviation of the arrival angle is directly related to increase in speed of the wind as shown in Figure 5.24.

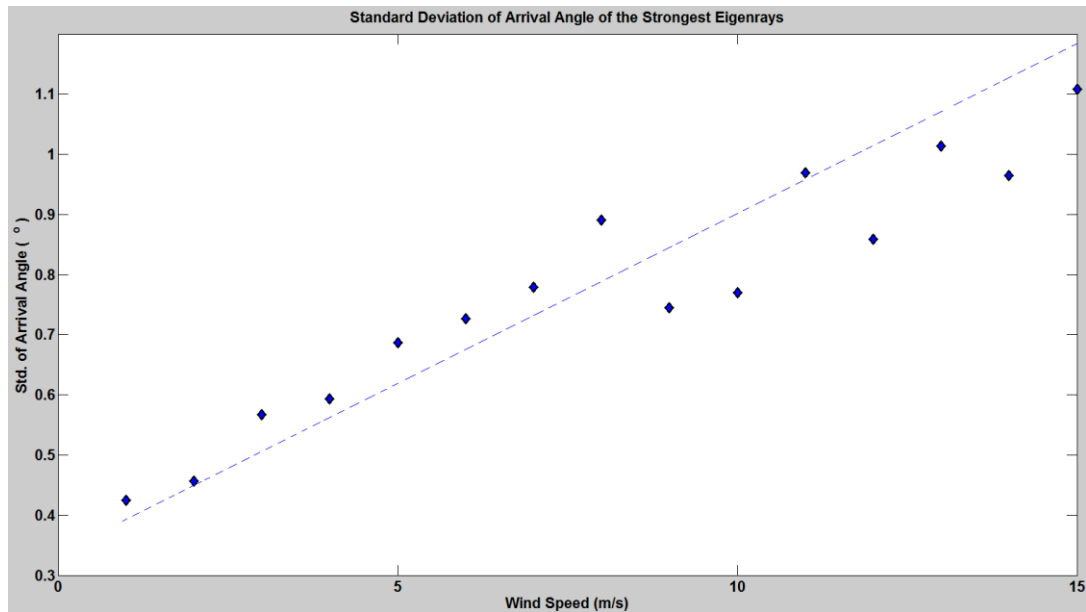


Figure 5.24: Standard Deviation of Arrival Angle wrt. Wind Speed (U)

Surface-normal velocities of the eigenray interaction points with the rough sea surface are also wind speed dependent values in a linear manner. It can be shown in Figure 5.25 that the slope of standard deviation of Doppler shift curve decreases after wind velocity is equal to 5 m/s . The reason of that can be saturation of computed surface-normal velocities used in Doppler shift calculations by post-processing.

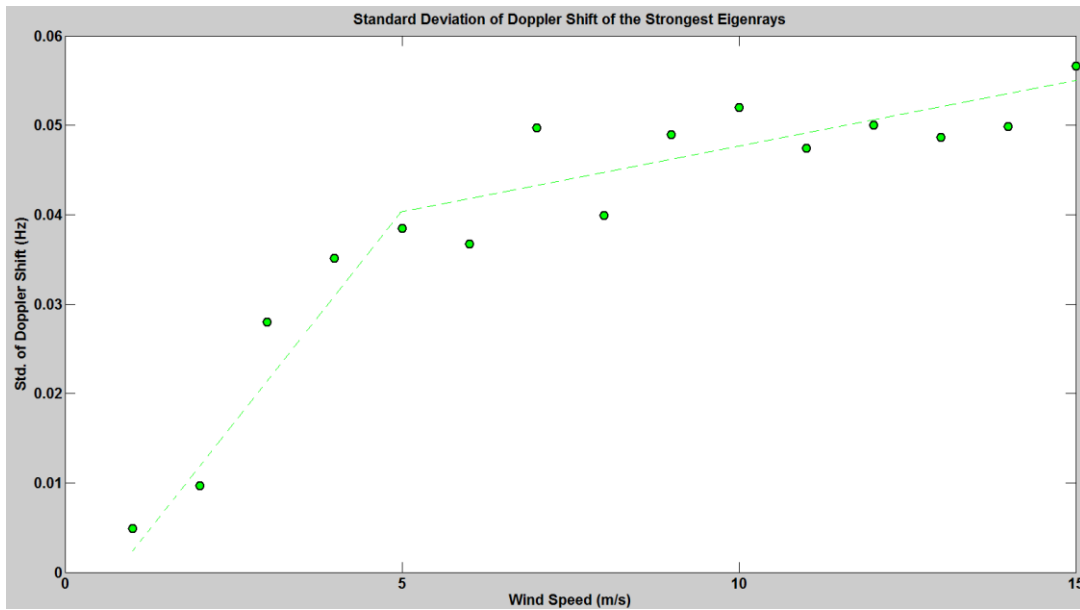


Figure 5.25: Standard Deviation of Doppler Shift wrt. Wind Speed (U)

Monte Carlo based simulations can be repeated for a larger beam fan interval. In the repeated simulations beam fan interval is chosen as 2.0° - 13.5° and other simulation parameters are not change. The results of the new simulation can be seen in Figure 5.26-Figure 5.28. As expected, standard deviations of the signal fluctuations with respect to wind speed gets larger with larger beam fan interval.

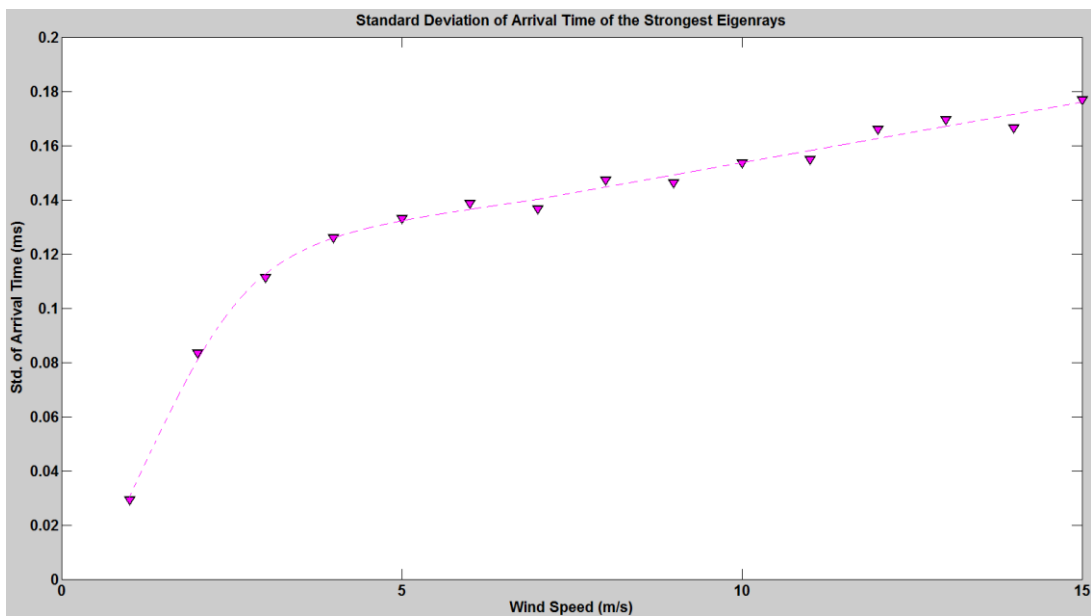


Figure 5.26: Standard Deviation of Arrival Time wrt. Wind Speed (U)

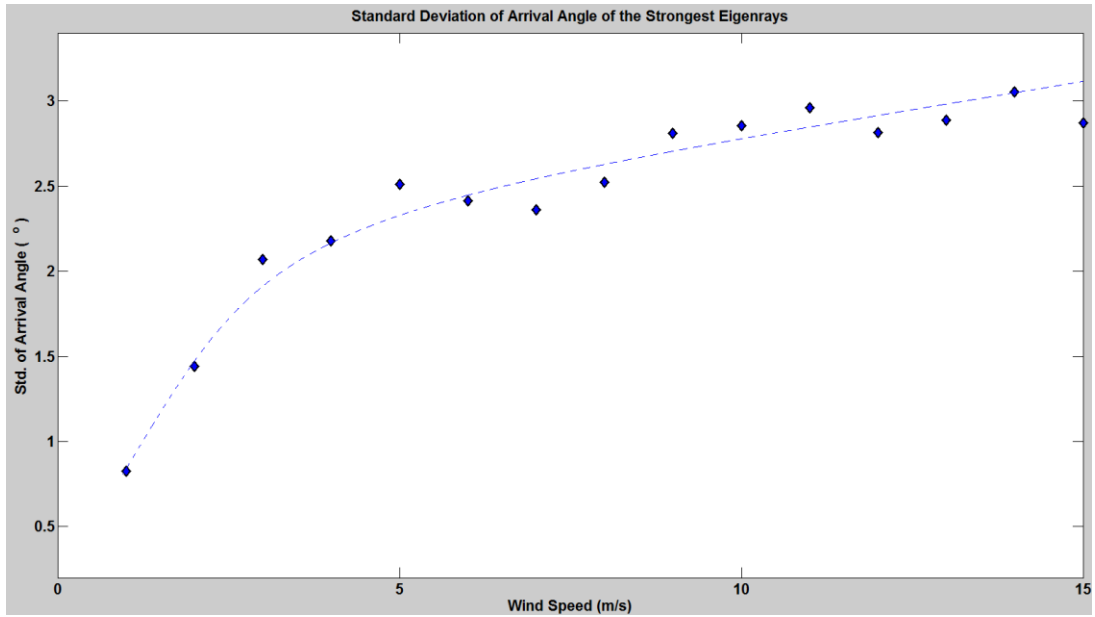


Figure 5.27: Standard Deviation of Arrival Angle wrt. Wind Speed (U)

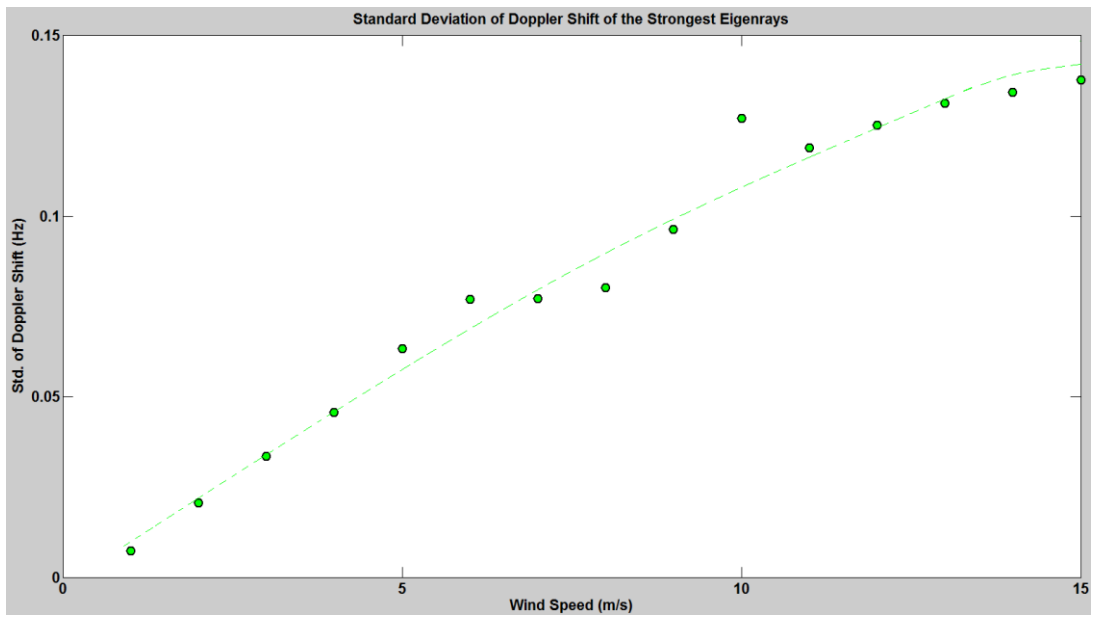


Figure 5.28: Standard Deviation of Doppler Shift wrt. Wind Speed (U)

CHAPTER 6

CONCLUSION

6.1 Concluding Remarks

Realistic linear sea surface wave model and ray-based acoustic propagation model, BELLHOP is combined in this thesis in order to simulate fluctuations in the eigenray arrivals due to wind-driven time-varying sea surface boundary. In addition to that the received timeseries are also obtained to examine amplitude fluctuations in the received signal. The arrival amplitude-delay file values are also used to construct received timeseries by convolution of the source signal with interpolated channel impulse responses. By utilizing the relationship between the main environmental parameters (wind speed and fetch) and the time-evolving sea surface wave field, sea surface motion induced acoustic signal fluctuations are modeled in this thesis. Doppler shifts calculated by the surface-normal velocity of ocean waves at reflection points of the acoustic signal. Statistics of the arrival fluctuations (time, angle, and Doppler shift) with respect to wind speed based on Monte Carlo simulations by using random sea surface realizations are given in this study as well. Since ray-based model, BELLHOP program is used in this study, the computational speed is high relatively. The coupled model also allows the change of the environmental parameters, the model geometry, and other inputs of model in a quick way. It is open to make simulations parallel in order to decrease computational time as well.

6.2 Future Work

In the further work of this thesis additional factors can be included to the coupled model. For example, moving source(s) and receiver(s) can be added to observe additional Doppler effects. Actually, VirTEX code presents an interpolation scheme for steady source/receiver motion readily. The received timeseries can be obtained by

using that scheme when source/receiver is/are in motion in addition to the time-varying sea surface.

Simulations in this thesis are made for isovelocity medium, sound speed profile can also be taken into account for acoustic propagation model. The effects of the refracting sound waves on Doppler shift calculations can be examined.

BELLHOP is a ray tracer operates in 2D computational environments (range and depth). 3D simulations can be made by using a 3D ray tracer in order to observe the effects of out-of-plane scattering as well.

Experiments can be conducted in order to validate results of coupled model with adjusted arrival delays. In these experiments, only the single surface reflected portion of the acoustic signal can be distinguished. Then sea surface wave data obtained for different wind speeds can be imported into combined/coupled model in order to compare model results with measurements obtained from experiments.

In order to improve the model and to make more realistic simulations especially in shallow water bubble clouds can be located into a hydrodynamic computational geometry as well. It requires knowledge about bubble scattering e.g., refractive and dissipative effects of the bubbles.

REFERENCES

- [1] C. Bayindir, "Implementation of a computational model for random directional seas and underwater acoustics," M.S. thesis, Dept. Civil Environ. Eng., Univ. Delaware, Newark, DE, 2009.
- [2] M. B. Porter and H. P. Buckner, "Gaussian beam tracing for computing ocean acoustic fields," *J. Acoust. Soc. Amer.*, vol. 82, pp. 1348–1359, 1987.
- [3] M. B. Porter, Acoustic Toolbox [Online]. Available: <http://oalib.hlsresearch.com/Rays/index.html>, last accessed on 5 September 2014
- [4] M. Siderius and M. B. Porter, "Modeling broadband ocean acoustic transmissions with time-varying sea surface," *J. Acoust. Soc. Amer.*, vol. 124, pp. 137–150, 2008.
- [5] E. I. Thorsos, "Acoustic scattering from a 'Pierson-Moskowitz' sea surface," *J. Acoust. Soc. Amer.*, vol. 88, pp. 335–349, 1990.
- [6] P. H. Dahl, "High-frequency forward scattering from the sea surface: The characteristic scales of time and angle spreading," *IEEE J. Ocean. Eng.*, vol. 26, no. 1, pp. 141–151, Jan. 2001.
- [7] K. Hasselmann, T. P. Barnett, E. Bouws, H. Carlson, D. E. Cartwright, K. Enke, J. A. Ewing, H. Gienapp, D. E. Haselmann, P. Kruseman, A. Meerburg, P. Muller, D. J. Olbers, K. Richter, W. Sell, and H. Walden, "Measurements of wind-wave growth and swell decay during the Joint North SeaWave Project (JONSWAP)," *Deut. Hydrogr. Inst. Hamburg*, vol. 8, pp. 6–95, 1973.
- [8] Clay, C.S. and Medwin, H. (1977). *Acoustical Oceanography: Principles and Applications*. John Wiley and Sons, New York.
- [9] Eckart, C. (1953). "The scattering of sound from the sea surface", *J. Acoust. Soc. Am.* 25, 566-570.
- [10] Rice, S.O. (1951). "Reflection of electromagnetic waves from slightly rough surfaces", *Commun. Pure Appl. Math* 4, 351-278.
- [11] M. B. Porter, "The time-matched fast-field program (FFP) for modeling acoustic pulse propagation," *J. Acoust. Soc. Am.*, vol. 87(5), pp. 2013-2023,

May 1990.

- [12] M.B. Porter, “The KRAKEN normal mode program (Draft),” Naval Research Laboratory, Washington DC, 1992.
- [13] E. A. Karjadi, M. Badiey, J. T. Kirby, and C. Bayindir, “Effects of surface gravity waves on high frequency propagation in shallow water,” *IEEE J. Ocean. Eng.* 37, 112–121 (2012).
- [14] John C. Peterson and Michael B. Porter, “Ray/beam tracing for modeling the effects of ocean and platform motion” *J.Acoust. Soc. Am.*, vol. 38(4), pp. 655-665, October 2013.
- [15] Michael B. Porter and Yong-Chun Liu “Finite-element ray tracing”, *Theoretical and Computational Acoustics*, vol. 2, pp.947-956, New Jersey Institute of Technology, Newark, 1994.
- [16] Rodriguez O.C., Silva A.J., Gomes J.P., and Jesus S.M. “Modeling arrival scattering due to surface roughness.” In *Proceedings of ECUA2010*, Istanbul, Turkey, July 2010.
- [17] B. E. Parkins,” Scattering from the Time-Varying Surface,” *J. Acoust. Soc. Amer.* 42, 1262-1267 (1967).
- [18] Louis L. Scharf and Robert L. Swarts, “Acoustic scattering from stochastic sea surface”, *J. Acoust. Soc. Am.* Vol. 55, no. 2, pp. 247-253 February 1974.
- [19] W. I. Roderick and B. F. Cron, “Frequency spectra of forward-scattered sound from the ocean surface”, U.S Navy Underwater Sound Laboratory, New London, Connecticut, January 1970.
- [20] Mitsuyasu H. and Tsuyoshi U. “A comparison of observed and calculated directiocal wave spectra in the east China sea.” *Journal of the Oceanographical Society of Japan*, 45:338–349, September 1989.
- [21] Hasselmann D.E., Dunckel M., and Ewing J. A. *Directional Wave Spectra Observed during JONSWAP 1973.* *Journal of Physical Oceanography*, 10:1264–1280, August 1980.
- [22] Coastal Engineering Technical Note, “Directional wave spectra using cosine-squared and cosine 2S spreading functions ”, U.S. Army Engineer Waterways Experimental Station, Coastal Engineering Research Center, P.O. Box 631 Vicksburg, Missisipi 39180, June 1985.
- [23] Heitsenrether R.M. and Badiey M. “Modeling Acoustic Signal Fluctuations Induced by Sea Surface Roughness.” In *Proceedings of the High Frequency Ocean Acoustics Conference*, AIP Conference Proceedings, volume 728,

pages 214–221, March 2004.

- [24] Abdalla, S. (1991), ‘Development of a Third Generation Wind Wave Model Applicable to Finite Depths’, Ph.D. Thesis, Middle East Technical University, Ankara, Turkey.
- [25] Yilmaz N. “Spectral Characteristics of Wind Waves in the Eastern Black Sea”, Ph.D. Thesis, Middle East Technical University, Ankara, Turkey, July 2007
- [26] Robert H. Stewart, “Introduction to the Physical Oceanography”, chap. 16: Ocean waves, Texas A&M University, July 2007, Available: http://oceanworld.tamu.edu/resources/ocng_textbook/chapter16/chapter16_01.htm, last accessed on 5 September 2014
- [27] W. J. Pierson Jr., and L. Moskowitz, “A proposed spectral form for fully Developed wind seas based on the similarity theory of S.A. Kitaigorodskii”, J. Geophys. Res. 69, 5181-5190 (1964).
- [28] Donelan, M.A., Hamilton, J. and Hui, W.H. (1985). “Directional spectra of wind generated waves”, Phil. Trans. R. Soc. Lond. A 315, 509-562.
- [29] F. B. Jensen, W. A. Kuperman, M. B. Porter, and H. Schmidt, “Computational Ocean Acoustics”, Second Edition, Springer
- [30] J. C. Torres, “Modeling of high-frequency acoustic propagation in shallow water”, Ensign, United States Navy, B.S. United States Naval Academy, Naval Postgraduate School, June 2007
- [31] W.I. Roderick and R. Deavenport, “Doppler characteristics of sea surface reflected and scattered acoustic signals induced by surface wave motion”, IEEE, pp. 287-292, New London, 1993
- [32] P. Qarabaqi and M. Stojanovic, “Statistical characterization and computationally efficient modeling of class of underwater acoustic channels”, IEEE Journal of Oceanic Engineering, vol.38, no.4, October 2013
- [33] M. B. Porter, “Numerical Methods of acoustic modeling”, from Proceedings of Undersea Defense Tech. Conf., London, 1983
- [34] S. T. McDaniel and D. F. McCammon, “Composite-roughness theory applied to scattering from fetch limited seas,” J. Acoust. Soc. Amer., vol. 82, pp. 1712–1719, 1987.
- [35] C.T. Tindle, G.B. Deane, Shallow water sound propagation with surface waves. J. Acoust. Soc. Am., 117, 2783–2794 (2005)

- [36] Kuryanov, B.F. (1963). “The scattering of sound at a rough surface with two types of irregularity”, *Sov. Phys. Acoust.* 8, 252-257.
- [37] C.T. Tindle, “Wavefronts and Waveforms in Deep-Water Sound Propagation” . *Acoust. Soc. Am.*, vol. 112, no. 2 pp. 464-475, 2002
- [38] Modern Beaufort Force Scale Table, Available at: http://en.wikipedia.org/wiki/Beaufort_scale, last accessed on 5 September 2014
- [39] G.A. Mastin, P.A. Watterberg, and J.F. Mareda, “Fourier Synthesis of Ocean Scenes”, Sandia National Laboratories, IEEE, 1987
- [40] M. B. Porter, The BELLHOP manual and user’s guide [online], <http://oalib.hlsresearch.com>, last accessed on 5 September 2014
- [41] R. J. Urick, “Principles of underwater sound”, 3rd Edition, Peninsula Publishing
- [42] “Runge-Kutta method”, pdf Available at: https://www.math.okstate.edu/~yqwang/teaching/math4513_fall11/Notes/rungekutta.pdf , last accessed on 5 September 2014
- [43] J.M. Howem, “Modeling and measurement methods for acoustic waves and acoustic microdevices”, chapter 23, ”Ray trace modeling of the underwater sound propagation”, Norway
- [44] O.C. Rodriguez, “General description of the BELLHOP ray tracing program”, Version 1.0, (13/06/2008), Available Online at: <http://oalib.hlsresearch.com/Rays/index.html>, last accessed on 5 September 2014